SIMULATION OF MULTIOBJECT NANOSCALE SYSTEMS

A Dissertation

Presented to

The Graduate Faculty of The University of Akron

In Partial Fulfillment

of the Requirements for the Degree

Doctor of Philosophy

Jianhua Dai

May, 2009

SIMULATION OF MULTIOBJECT NANOSCALE SYSTEMS

Jianhua Dai

Dissertation

Approved:

Advisor
Dr. Igor Tsukerman

Committee Member
Dr. Nathan Ida

Committee Member
Dr. Iqbal Husain

Committee Member
Dr. Alex Povitsky

Committee Member
Dr. Dmitry Golovaty

Accepted:

Department Chair
Dr. Alex De Abreu-Garcia

Dean of the College
Dr. George K. Haritos

Dean of the Graduate School
Dr. George R. Newkome

Date

ABSTRACT

The development of nanoscience and nanotechnology has important implications for advances of electronics, biology, medicine, photonics, and other areas. The growing knowledge in this field will lead to profound progress in the ways that materials, devices, and systems are understood and created. Numerical simulation is an indispensabe tool for understanding nanoscale systems, as our usual intuition may be misleading at the nanoscale.

This dissertation focuses on two classes of numerical methods: the finite element method (FEM) and finite difference (FD) methods with their generalization known as the flexible local approximation method (FLAME). FEM is a versatile numerical method that is widely applied in all areas of engineering analysis. This method remains powerful for many physical nanoscale models, especially problems invloving complex geometries and inhomogeneous media, provided that the required number of finite elements is not too large. However, for a large number of objects, the complexity and the computational overhead of FE meshes and the related data structures become too high.

Based on the simple Taylor expansions, FD method has significant advantage for geometrically simple problems. However, the accuracy of FD deteriorates for problems with geometrically complex boundaries and material interfaces not

conforming to the FD grid lines. The Taylor expansion breaks down at material interface boundaries because the solution is not sufficiently smooth for such problems. FLAME is a generalized FD calculus recently developed. It replaces the Taylor expansion with a physically and mathematically more accurate local approximation. By this way, this method reduces or even eliminates the "staircase" noise at slanted or curved material interfaces. FLAME is first applied in the simulations of electrostatic and magnetostatic multiparticle problems. It shows higher accuracy both in two dimensions (2D) and three dimensions (3D) compared with the finite difference (FD) method and FEM. FLAME also exhibits flexibility in the interpolation of the potential, electric field, and the calculation of the force. For the problems in which components are in close proximity to each other, analytical/numerical bases and adaptive mesh algorithms are developed based on FLAME for better accuracy without increasing the complexity of the calculation.

The FLAME method, including analytical/numerical bases and adaptive mesh algorithms, is also applied to wave scattering problems. The computational cost of FLAME in many cases is much lower than that of other methods at comparable levels of numerical accuracy.

As a novel application of FLAME, this method is used to explore electrostatic interactions for macromolecules (e.g. protein molecules) in electrolytes. In the conventional model, the whole domain is divided into two layers: the inner macromolecular core and the outer solvent. The inner layer is governed by the Poisson equation with the existance of point charge, and the outer one is governed

by the Poisson-Boltzmann equation due to the Boltzmann-like distribution of ions. Results show that this model has great accuracy for short-distance interaction. However, the accuracy for long-distance interaction is not as good as for short-distance interaction. To improve the whole accuracy, an interim layer with a low dielectric permittivity is introduced to simulate the region between macromolecular core and solvent. The simulation based on FLAME shows significant accuracy improvement compared with that of the conventional FD method. The accuracy in FLAME is high even for the area around point charge singularities.

FEM is applied to a ferrofluid model that is of interest in magneticly driven assembly of micro- and nanoparticles [1, 2]. The ferrofluid particles are characterized by their volume density with a Boltzmann-like distribution function in the magnetic field. The problem is formulated in terms of the scalar , rather than vector, magnetic potential, which significantly reduces the computational cost.

FEM is used for the problem of nano-focusing of light by a self-similar cascade of silver nanoparticles. The goal is to explore the electrodynamic effects affecting the very high local field enhancement. The results lead to appreciable corrections of field enhancement in real applications.

ACKNOWLEDGEMENTS

First and foremost, I would like to express my appreciation to my advisor, Dr. Tsukerman, for his guidance, support and encouragement. He has shown a large and consistent interest in my project during the time and provided me valuable advices and comments in various ways.

I express gratitudes to my committee members, Dr. Ida, Dr. Husain, Dr. Povitsky and Dr. Golovaty for reviewing my work and helpful recommendations.

Special thanks are given to my fellow graduate student, Frantisek, for his useful discussions and information related with the topic. The sincere friendship and support from him always gave me energy and impetus to finish this research.

My deepest gratitude goes to my girlfriend Silin Ding, my friends Mr. and Mrs. Tass, and my family who provide love and support more than I could ever expect.

TABLE OF CONTENTS

LIST OF TABLES

LIST OF FIGURES

CHAPTER I

INTRODUCTION

This chapter presents an overview of selected problems in nanotechnology, and numerical methods that may be applied to these problems. The organization of this thesis is summarized.

1.1 General Overview

Nanotechnology seeks to discover and manipulate the properties of matter at the nanoscale in order to develop new applications across many fields, such as electronics, photonics, medicines, and materials [3, 4]. These materials and systems can be designed to exhibit novel and significantly improved physical, chemical, and biological properties, phenomena, and processes as a result of the limited size of their constituent particles or molecules. For example, in the field of nanoscale electronics, one development would be further miniaturizing the electronic circuits, which leads to faster, more sophisticated, and more portable devices [5].

Nanotechnology includes the integration of nanoscale structures into larger material's components, systems, and architectures. However, within these larger-scale systems, the control and construction remains at the nanoscale. This scale

leads to dealing with a very large number of elements. Taking integrated electronic systems as an example, modern microelectronic systems contain up to 100 million devices on a single chip. Nanoelectronics might push this number up to 1 billion or more devices [6]. The primary problem is not only the large number of devices, but also the development time and the time for testing such systems.

Nanotechnology is a very broad concept that includes many research branches. It is impossible to cover all of them in this thesis. This thesis presents the research and development of computational methods for electrostatic and magnetostatic interactions of nanoparticles, wave scattering problems, electrostatic interactions of proteins, self-assembly of colloidal systems and electrodynamic effects of nanooptics.

1.2 Multiobject Systems

Analysis of systems composed of many objects can be computationally expensive, and even unfeasible if the number of objects is too large. Simplification of such systems is necessary for simulations. It may involve focusing on a few key geometric and physical parameters.

For the analysis of multiobject systems, it is very important to have a proper mathematic model. Different parts of multiobject systems can often be represented by different parameters and even by different mathematic equations. As an example, the protein model discussed in Chapter 6 includes inside and outside domains governed by different equations.

The focus of this thesis is on the calculation of electromagnetic quantities, such as potential, field, and force. All macroscopic electromagnetic phenomena are governed by Maxwell's equations, a set of four partial differential equations that relate the electric and magnetic fields to their sources, charge density, and current density [7]. With the emphasis on frequency domain calculation in this thesis, the time-harmonic form of Maxwell's equations for complex phasors of the fields (with the time dependence $e^{j\omega t}$ implied) is as follows:

$$\begin{cases} \nabla \cdot \epsilon \mathbf{E} = \rho \quad Guass's\ law \\ \nabla \cdot \mathbf{B} = 0 \quad Guass's\ law\ for\ magnetism \\ \nabla \times \mathbf{E} = -j\omega\mu\mathbf{H} \quad Faraday's\ law \\ \nabla \times \mathbf{H} = \mathbf{J} + j\omega\epsilon\mathbf{E} \quad Ampère's\ law \end{cases} \tag{1.1}$$

where $\mathbf{E}$ is the electric field, $\mathbf{B}$ and $\mathbf{H}$ are magnetic field quantities interrelated by $\mathbf{B} = \mu\mathbf{H}$, ϵ and μ are the electrical permittivity and the magnetic permeability separately, and ρ and $\mathbf{J}$ are the electric charge and the current densities.

For electrostatic problems with $\omega = 0$, (1.2) can be deduced from Faraday's law

$$\nabla \times \mathbf{E} = 0 \tag{1.2}$$

Therefore, the electric field is conservative and $\phi = \int_C Edl$ is path-independent (for a simply connected domain), where C is an arbitrary path connecting the point with zero potential to the point under consideration. The field is

$$\mathbf{E} = -\nabla\phi \tag{1.3}$$

With this relation, (1.4) can be obtained from Gauss's law.

$$-\nabla \cdot \epsilon \nabla \phi \;=\; \rho \tag{1.4}$$

If the medium contains no free charges, (1.4) reduces to

$$-\nabla \cdot \epsilon \nabla \phi \;=\; 0 \tag{1.5}$$

Assuming the electric permittivity to be constant, (1.4) and (1.5) can be simplified to the Poisson equation (1.6) and the Laplace equation (1.7).

$$\nabla^2 \phi \;=\; -\frac{\rho}{\epsilon} \tag{1.6}$$

$$\nabla^2 \phi \;=\; 0 \tag{1.7}$$

In electrodynamic analysis ($\omega \neq 0$), either of the fields ($\mathbf{E}$ or $\mathbf{H}$) can be eliminated from the system of Maxwell's equations. Then, time-harmonic wave equations assume the form

$$\nabla \times \left(\frac{1}{\mu}\nabla \times \mathbf{E}\right) - \omega^2 \epsilon \mathbf{E} \;=\; -j\omega \mathbf{J} \tag{1.8}$$

$$\nabla \times \left(\frac{1}{\epsilon}\nabla \times \mathbf{H}\right) - \omega^2 \mu \mathbf{H} \;=\; \nabla \times \left(\frac{1}{\epsilon}\mathbf{J}\right) \tag{1.9}$$

Equations (1.1) as well as (1.8) and (1.9) are general and applicable to a broad range of electromagnetic problems. In this thesis, we consider several types of problems governed by these equations. In Chapter 5, a 2D model is used for wave-scattering from cylindrical particles. In Chapter 6, the Poisson-Boltzmann equation is used to simulate the Boltzmann-like distribution of the ions for determining electrostatic interactions in macromolecules. In Chapter 8, the wave equation is used to explore the electrodynamic effects in plasmonic nanolenses.

1.3 Numerical Methods Applicable to Nanoscale Simulation

Experimental investigation of nanoscale systems is generally difficult due to the small size of components. This makes the development of efficient and reliable simulation techniques particularly important. Simulation is indispensable for the design, synthesis, monitoring, and testing of nanoscale systems. The first critical step of the analysis is to formulate a mathematical model of systems (e.g. a set of differential equations with boundary conditions). Making sure that a particular mathematical model is valid on the nanoscale is not an easy task. The main thrust of this thesis is efficient methods of solving the engineering and physical nanoscale problems for which reasonably accurate models are already established. However, in some special cases, such as the protein simulation in Chapter 6, we do discuss the validity of the physical mode and possible amendments to it.

Except for a few simple cases, exact analytical solutions of numerical models are usually not available and it is necessary to resort to numerical approximations. There exist several well-established numerical methods. One of the oldest is the finite difference (FD) method. FD started to gain prominence in the 1920s and has been applied to solve different field problems [8]. It historically was the first numerical technique for boundary value problems in general physics, and in electromagnetism in particular. But it has salient disadvantages. The notorious "staircase" effect at slanted or curved boundaries decreases the accuracy of this method [9, 10].

An important category of FD methods is the finite-difference time-domain (FDTD) techniques. FDTD can be used in nanoscale simulation, for example in application to 3D photonic structures [11, 12]. FDTD still suffers from the staircase effect along curved boundaries. To extract the frequency domain information from FDTD simulations, one typically needs to apply the Fourier transform (FT) to long runs in time domains, which can render the simulation inefficient.

Another popular and powerful computation technique is the finite element method (FEM), which has been successfully used to solve a large variety of physical problems [13]. FEM belongs to the broad class of variational methods. Many commercial software packages based on FEM, such as Ansoft HFSS and COMSOL Multiphysics, are widely used. Both FEM and FD subdivide the computation domain into small subdomains; regular grids in various coordinate systems are typical in FD, whereas geometrically complex meshes are typical in FEM. For FEM, the overhead (mesh generation, data structures) could be significant for multiobject systems.

In nanoscale simulations, the large number of objects may lead to a very large number of grid nodes or elements to achieve the desired level of accuracy for FEM and FD. This complexity will be even greater when the objects are moving. For moving particles, the fast multipole method (FMM) works well. FMM is a mathematical technique based on the multipole expansion that was developed to speed up the calculation of long-ranged forces [14]. However, the computational advantage of this method manifests itself only when the number of objects is extremely large. FMM is also ineffective for heterogeneous media (e.g. finite-size

particles with dielectric or magnetic parameters different from those of free space), especially when the problem is governed by nonlinear equations.

Flexible local approximation method (FLAME) is one of the methods that play a central role in this thesis. It is a recently developed generalized FD calculus that incorporates accurate local analytical approximations of the solution into schemes [15, 16]. These approximations take into account specific local behavior of the solution. Examples of such approximations are exponentials, spherical harmonics, plane waves, polynomials, etc.

1.4 Organization of the Dissertation

This thesis presents the development of numerical simulation techniques for nanoscale systems, with the focus on FEM and FLAME. These two numerical methods are introduced in Chapters 2 and 3. Then, this thesis discusses applications of FLAME to electrostatic and wave scattering problems. Chapter 4 concentrates on applications of FLAME to eletrostatic multiparticle models in both 2D and 3D. In these models, all calculations of the potential, the electric field, and the electromagnetic force acting on the particles are presented in detail. Chapter 5 focuses on the 2D model of wave scattering by cylindrical particles. Chapter 6 presents the application of FLAME to the elecrostatic model of macromolecules. The model includes several layers of different materials with different dielectric properties. Two other nanoscale models, magnetic assembly of ferrofluid particles and electrodynamic nanolenses, are described in Chapters 7 and 8. Both models use FEM for numer-

ical simulations. Magnetic assembly of colloidal particles relies on a combination of applied magnetic fields and fields of permanent magnets. For electrodynamic nanolenses, the significant field enhancement achieves notable attention, but its small scale makes the experiment difficult. The nanolens model based on numerical simulation is applied to discover electrodynamic effects. Finally, Chapter 9 presents the conclusion of this thesis and recommendations for future research and potential application.

CHAPTER II

THE FINITE ELEMENT METHOD

This chapter serves as an introduction to the finite element method (FEM) that is used extensively in this thesis. The first part reviews the history of FEM and its application in electromagnetics. Then, the main principle of FEM is introduced. A simple illustrative example of FEM is demonstrated. The last section is a summary of FEM.

2.1 The Origin of FEM

FEM is a versatile and powerful numerical method that is widely applied to solve problems covering almost the whole spectrum of engineering analysis. Common applications include static, dynamic, and thermal behavior of physical systems, and their components. FEM belongs to the broad class of variational methods and is used for finding approximate solutions of partial differential equations (PDE) as well as of integral equations. This section follows an introductive review of the history of FEM in [17]. The original mathematical treatment of FEM can be traced to papers by Hrennikoff (1941) and Courant (1942). Some pioneering research was conducted by Turner, Clough, Martin, and Topp (1956) and Argyris (1960)

before the name of finite element method firstly used by Clough in 1960. The early use of FEM was restricted to the application of the techniques for structural related problems. It was not applied to electromagnetic problems until 1968 [8].

In this thesis, the emphasis is put on electromagnetic problems. It is usually possible to formulate such problems in a bounded domain, with given boundary conditions. A generic form of the governing differential equation in a domain Ω is

$$\mathcal{L}\phi \;=\; f \tag{2.1}$$

where $\mathcal{L}$ represents a differential operator, f is the excitation or force function, ϕ is the unknown function to be found. For electromagnetic problems, the form of the governing differential equation ranges from the Laplace or Poisson equation to scalar and vector wave equations. The boundary conditions range from simple Dirichlet and Neumann conditions, to complicated radiation or perfectly matched laayer (PML) conditions (introduced in Chapter 8).

2.2 The Variational Principles in FEM

Boundary value problems can be cast in a variational form. Instead of directly solving the PDE, it is possible to replace the problem of integrating a PDE by the equivalent problem of seeking a function that give a minimum value of some integral. This is the basis of variational principle. Based on it, the solution is approximated with an expansion.

$$\tilde{\phi} \;=\; \sum_{j=1}^{N} c_j \psi_j \;=\; \{c\}^T\{\psi\} \;=\; \{\psi\}^T\{c\} \tag{2.2}$$

where ψ_j are the chosen expansion functions, c_j are coefficients to be determined. Depending on the variational principle, there are two popularly used approaches for FEM: Rayleigh-Ritz and Galerkin.

According to Mikhlin [18], if operator $\mathcal{L}$ in (2.1) is real, self-adjoint, and positive definite, the solution of (2.1) can be obtained by minimizing the functional

$$I(\phi) \;=\; \frac{1}{2} < \mathcal{L}\phi, \phi > \;\; - \;\; < \phi, f > \tag{2.3}$$

where the inner product, denoted by the angular bracket, is defined as

$$< \phi, \psi > \;\; = \;\; \int_{\Omega} \phi \psi^* d\Omega \tag{2.4}$$

An approximational solution can be obtained by minimizing the functional (2.3) in a finite dimensional subdomain. That is the essence of the Ratleigh-Ritz method. Substituting the approximated solution (2.2) into (2.3), the approximated variational functional is obtained.

$$I(\tilde{\phi}) \;=\; \frac{1}{2}\{c\}^T \int_{\Omega} \{\psi\}\mathcal{L}\{\psi\}^T d\Omega \{c\} - \{c\}^T \int_{\Omega} \{\psi\} f d\Omega \tag{2.5}$$

Generally speaking, substituting $\tilde{\phi}$ for ϕ results in a nonzero residual.

$$r \;=\; \mathcal{L}(\tilde{\phi} - \phi) \;=\; \mathcal{L}\tilde{\phi} - f \;\neq\; 0 \tag{2.6}$$

A suitable approximation is obtained if the residual is required to be zero in some weighted-average sense.

$$R_i \;=\; \int_{\Omega_i} w_i r d\Omega \;=\; 0 \tag{2.7}$$

where w_i is a judiciously chosen weighted function. Substituting (2.2),

$$R_i \;=\; \int_{\Omega_i} (w_i \mathcal{L}\{\psi\}^T\{c\} - w_i f) d\Omega \;=\; 0 \tag{2.8}$$

The Galerkin method selects the weighting functions w_i to be the same as the basis functions. When the operator is a positive definite linear differential operator of an even order, the Galerkin method is equivalent to the Rayleigh-Ritz method. Other choices of weighted functions lead to other methods, such as the point collocation method, the subdomain collocation method and the least squares method.

FEM provides a discretization procedure for the variational form by subdividing the computational domain into elements. Finite elements of various geometric shapes are commonly used in FE analysis. In 2D, the common shapes are triangle and quadrangle. In 3D, the common shapes are tetrahedron and hexahedron. The choice of the element types depends on the physical problem, the required accuracy and geometric convenience of discretization. Several types of elements could be mixed in a single mesh. Curved elements are commonly used as well, to approximate non-planar boundaries with high accuracy.

Making the mesh finer over parts or all of the domain is known as h-refinement. Increasing the order of elements is termed p-refinement. Both refinement techniques can improve the calculation accuracy. Naturally, higher accuracy typically entails higher computational cost.

2.3 An Illustrative Example for FEM

For illustrative purpose, an example of a 2D boundary value problem is demonstrated in this section. The Rayleigh-Ritz method is applied to the Helmholtz equation

$$\nabla^2\phi + \kappa^2\phi \;=\; f \tag{2.9}$$

Assuming linear triangular elements are selected, numerical solution $\tilde{\phi}$ within an element e is of the form

$$\tilde{\phi_e}(x,y) \;=\; a_{e1} + a_{e2}x + a_{e3}y \tag{2.10}$$

It is convenient to switch to the nodal basis functions.

$$\tilde{\phi_e}(x,y) \;=\; \sum_{i=1}^{3} \psi_{ei}(x,y)c_{ei} \tag{2.11}$$

Here i represents the node's number of triangular element e. Each of these basis functions is equal to 1 at one of the nodes of the mesh and zeros at all other nodes, as shown in Figure 2.1. The basis functions can be calculated to be described by the following expression.

$$\begin{aligned}
\psi_{e1} &= \frac{1}{2A_e}[(x_{e2}y_{e3} - x_{e3}y_{e2}) + (y_{e2} - y_{e3})x + (x_{e3} - x_{e2})y] \\
\psi_{e2} &= \frac{1}{2A_e}[(x_{e3}y_{e1} - x_{e1}y_{e3}) + (y_{e3} - y_{e1})x + (x_{e1} - x_{e3})y] \\
\psi_{e3} &= \frac{1}{2A_e}[(x_{e1}y_{e2} - x_{e2}y_{e1}) + (y_{e1} - y_{e2})x + (x_{e2} - x_{e1})y]
\end{aligned} \tag{2.12}$$

where A_e is the area of element e.

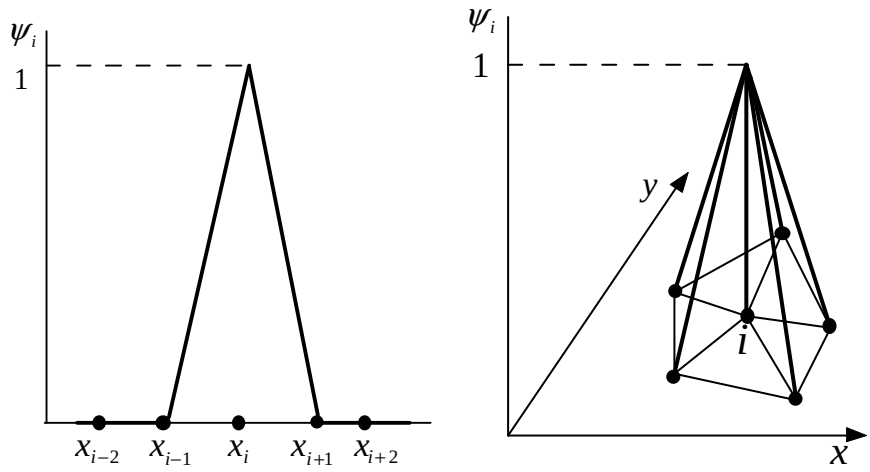

(a) First order 1D elements (b) First order 2D elements

Figure 2.1: Linear basis function for 1D and 2D of first order elements.

For the PDE (2.9), the variation functional for element e is

$$I(\tilde{\phi}_e) \;=\; \frac{1}{2}\int_{\Omega_e}\left[|\nabla\tilde{\phi}_e|^2 - \kappa^2\tilde{\phi}_e{}^2 + 2f\tilde{\phi}_e\right]d\Omega \tag{2.13}$$

Here Ω_e represents the domain of the element e. To minimize the $I(\tilde{\phi}_e)$, its differential operation with c_{ei} together with (2.11) yields

$$\frac{\partial I(\tilde{\phi}_e)}{\partial c_{ei}} \;=\; \sum_{j=1}^{3} c_{ej}\int_{\Omega_e}\left(\frac{\partial\psi_{ei}}{\partial x}\frac{\partial\psi_{ej}}{\partial x} + \frac{\partial\psi_{ei}}{\partial y}\frac{\partial\psi_{ej}}{\partial y} - \kappa^2\psi_{ei}\psi_{ej} + f\psi_{ei}\right)dxdy \quad i=1,2,3 \tag{2.14}$$

This equation can be simplified to

$$\left\{\frac{\partial I(\tilde{\phi}_e)}{\partial c_e}\right\} \;=\; [K_e]\{c_e\} - \{b_e\} \tag{2.15}$$

Here $\left\{\frac{\partial I(\tilde{\phi}_e)}{\partial c_e}\right\} \;=\; [\frac{\partial I(\tilde{\phi}_e)}{\partial c_{e1}}, \frac{\partial I(\tilde{\phi}_e)}{\partial c_{e2}}, \frac{\partial I(\tilde{\phi}_e)}{\partial c_{e3}}]^T$, and $\{c_e\} \;=\; [c_{e1},\; c_{e2},\; c_{e3}]^T$. The entire of matrix $[K_e]$ are calculated as

$$K_{eij} \;=\; \int_{\Omega_e}\left(\frac{\partial\psi_{ei}}{\partial x}\frac{\partial\psi_{ej}}{\partial x} + \frac{\partial\psi_{ei}}{\partial y}\frac{\partial\psi_{ej}}{\partial y} - \kappa^2\psi_{ei}\psi_{ej}\right)dxdy \quad i,j=1,2,3 \tag{2.16}$$

The elements of vector $\{b_e\}$ are calculated as

$$b_{ei} \;=\; \int_{\Omega_e} f\psi_{ei} dxdy \quad i = 1, 2, 3 \tag{2.17}$$

By including all N elements, we can get

$$\left\{\frac{\partial I(\tilde{\phi})}{\partial c}\right\} \;=\; \sum_{e=1}^{N} \left\{\frac{\partial I(\tilde{\phi_e})}{\partial c_e}\right\} \;=\; \sum_{e=1}^{N} ([K_e]\{c_e\} - \{b_e\}) \;=\; [K]\{c\} - \{b\} \;=\; 0 \tag{2.18}$$

Proper amendments to (2.18) must be made to take into account the boundary conditions; the relevant procedures are well known and described in the FE literatures [19–21].

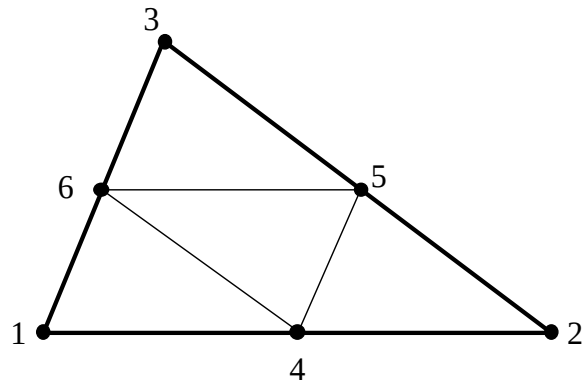

Figure 2.2: Quadratic triangular element.

The brief description above is for first order elements. As mentioned, the accuracy of FEM can be improved not only by h-refinement (mesh refinement), but also by p-refinement (increasing the order). Here let us consider quadratic triangular elements for illustration.

As shown in Figure 2.2, the quadratic triangular element has six nodes. In this element, the form of approximation for $\tilde{\phi}$ is

$$\tilde{\phi_e}(x,y) \;=\; a_{e1} + a_{e2}x + a_{e3}y + a_{e4}x^2 + a_{e5}xy + a_{e6}y^2 \tag{2.19}$$

The corresponding element basis functions are calculated as

$$\begin{aligned} \Psi_{ei} \;&=\; (2\psi_{ei} - 1)\psi_{ei}, \quad i = 1,2,3 \\ \Psi_{e4} \;&=\; 4\psi_{e1}\psi_{e2}, \qquad \Psi_{e5} \;=\; 4\psi_{e2}\psi_{e3} \\ \Psi_{e6} \;&=\; 4\psi_{e3}\psi_{e1} \end{aligned} \tag{2.20}$$

Here $\psi_e^i,\ i = 1,2,3$ is as (2.12).

Matrix assembly is performed in a similar manner as for first order elements. Higher accuracy of the numerical result can usually be expected with higher order, but at a higher computational cost.

2.4 Conclusion

FEM is a numerical method based on variational principles and special basis functions defined over the finite elements in the computation domain. These functions approximates the field in a piece-wise way. The solid variational foundation of FEM makes the method remarkably robust. The numerical approximation depends not only on the mesh refinement, but also on the order of the elements. Hp-refinement (especially incorporating adaptive algorithms discussed in Chapter 8) aims at the most effective use of the computational resources. Overall, FEM is a popular numerical method that has wide applications in a variety of areas.

CHAPTER III

THE FLEXIBLE LOCAL APPROXIMATION METHOD (FLAME)

FLAME is a new numerical method that has already demonstrated its strengths in several applications [15, 16, 22, 23]. The main ideas of the method and the construction of FLAME schemes are presented below. Several examples are given, ranging from the 1D Laplace equation to the 3D linerized Poisson-Boltzmann equation.

3.1 Development of FLAME

The flexible local approximation method (FLAME) has been developed since 2004 [15, 16, 22]and has already been applied to a wide variety of problems: colloidal systems, photonic crystal waveguides, electrostatic interactions in solute-solvent systems, and more [21, 23, 24]. This method is a substantial generalization of classical FD method.

The FD method typically uses local Taylor expansions in the vicinity of a grid stencil to generate a scheme on grids that are usually simple and regular with respect to one of the standard coordinate systems. The relative simplicity makes FD easy to use and may be a significant advantage for geometrically simple problems. But the accuracy of FD deteriorates for problems with geometrically complex

boundaries and material interfaces not conforming to the FD grid lines. As an obvious example, Figure 3.1(a) shows that the curved boundary of a circular particle is represented inaccurately as a "staircase" on a regular FD grid. In FD (flux balance) schemes (see Chapter 4), the circular particle is approximated by the dashed-line pattern. This introduces the "staircase" noise, especially when the mesh is relatively coarse. Although the geometric interpretation of this effect is obvious, the algebraic origin of the noise lies in the Taylor expansion, which breaks down at material interface boundaries because the solution is not sufficiently smooth. The easiest way to reduce the error is to refine the mesh, but it will increase the computational cost.

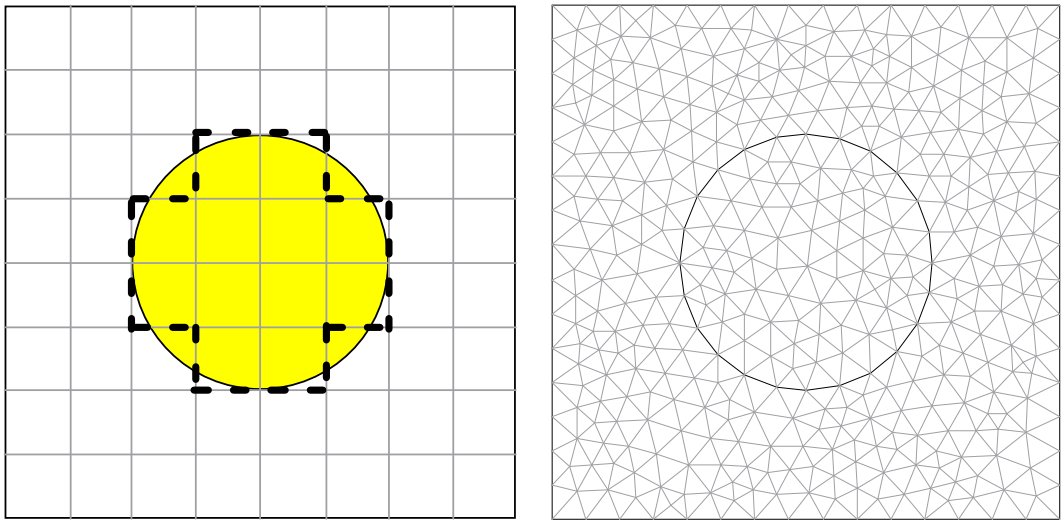

(a) FD mesh (b) FEM mesh

Figure 3.1: Sample mesh for FD and FEM.

For comparison, the Finite Element Method (FEM, Chapter 2) employs geometrically conforming meshes, as illustrated in Figure 3.1(b). This is one of the

reasons why FEM is so powerful in a variety of problems, especially where the geometry is complex. The flexible choice of various geometric shapes for finite elements and hp-refinement make FEM even more powerful. However, the computational overhead of mesh generation and matrix assembly in FEM cannot be brushed aside. As an example, for the problems with a large number of moving particles, the generation of geometrically conforming FE meshes is quite complicated or even impractical.

It is desirable to look for a method that could operate on a simple grid and yet would reduce or even eliminate the "staircase" noise at slanted or curved interfaces. Then the accuracy could be significantly improved, while keeping the grid and the numerical algorithm relatively simple. Since, as mentioned above, the algebraic nature of the numerical noise is in the breakdown of the Taylor expansion at curved interfaces, it is only natural to replace the Taylor expansion with a physically and mathematically more accurate local approximation. In the "Trefftz" version of FLAME, the approximating functions are chosen to satisfy the governing equation of the problem (along with the interface boundary conditions).

It should be emphasized that the approximating functions are defined locally, within small subdomains around each grid node. Unlike accurate global solutions, local ones are usually relatively easy to derive, as many examples in this thesis and in the papers cited above demonstrate. More specifically, fields around spherical particles can be approximated by several spherical harmonics; fields scattered from cylinders are by Bessel functions, and so on. Such analytical approximations

are incorporated directly into the difference scheme. Furthermore, if an analytical or quasi-analytical local approximation of the solution cannot be found, the approximation by other numerical method will be used.

3.2 Introduction to the FD Method

A general approach for constructing FD schemes is by Taylor's series. According to the well-known expansion,

$$f(x_0 + \Delta x) \;=\; f(x_0) + \Delta x f'(x_0) + \frac{1}{2!}(\Delta x)^2 f''(x_0) + \frac{1}{3!}(\Delta x)^3 f'''(x_0) + \cdots \quad (3.1)$$

and

$$f(x_0 - \Delta x) \;=\; f(x_0) - \Delta x f'(x_0) + \frac{1}{2!}(\Delta x)^2 f''(x_0) - \frac{1}{3!}(\Delta x)^3 f'''(x_0) + \cdots \quad (3.2)$$

By subtracting (3.2) from (3.1)

$$f(x_0 + \Delta x) - f(x_0 - \Delta x) \;=\; 2\Delta x f'(x_0) + O(\Delta x)^3 \quad (3.3)$$

Here $O(\Delta x)^3$ is the error of truncating the series. Usually it is called the error of the order $(\Delta x)^3$, and even simply the 3rd order. To get the approximation, the $O(\Delta x)^3$ will be neglected to get

$$f'(x_0) \;=\; \frac{f(x_0 + \Delta x) - f(x_0 - \Delta x)}{2\Delta x} \quad (3.4)$$

Adding (3.1) and (3.2), and neglecting the term $O(\Delta x)^4$, it yields

$$f''(x_0) \;=\; \frac{f(x_0 + \Delta x) - 2f(x_0) + f(x_0 - \Delta x)}{(\Delta x)^2} \quad (3.5)$$

By taking more terms in Taylor expansions, higher-order approximations, and correspondingly better accuracy, are obtained.

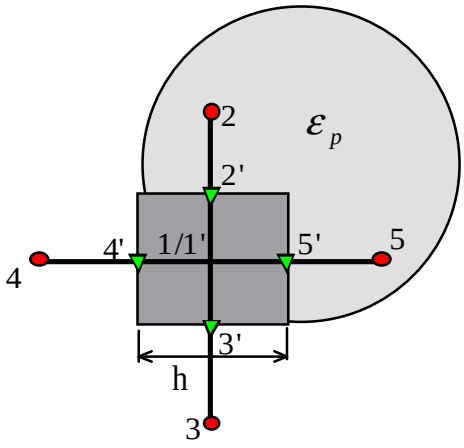

Figure 3.2: An example on the FD scheme.

A 2D example is shown in Figure 3.2 where the FD scheme spans both the particle and the outside region with different dielectric constants. This example is used to describe the construction of FD scheme based on the flux balance. An area is imagined, as the gray square shown. Each triangle points is the center of two element nodes. By the relation between electrical field and potential, (3.6) can be derived

$$E_{n'} \;=\; -\nabla V_{n'} \;=\; -\frac{V_n - V_1}{d_{n1}} \qquad n \;=\; 2,3,4,5 \tag{3.6}$$

where d_{n1} is the distance between points n and 1. Based on the flux balance, and assuming that there is no any source in the square area, we can get

$$\sum_{n=2}^{5} E_{n'} \cdot \varepsilon_{n'} \cdot h \;=\; 0 \tag{3.7}$$

Here h is the mesh size. For the example in Figure 3.2, points $2'$ and $5'$ belong to the particle area, with $\varepsilon_{2'} = \varepsilon_p$, $\varepsilon_{5'} = \varepsilon_p$. The dielectric constant for points $1'$, $3'$ and $4'$ is the same as that of a vacuum. Therefore, the FD scheme will be

$$\varepsilon_p V_2 + \varepsilon_0 V_3 + \varepsilon_0 V_4 + \varepsilon_p V_5 - (2\varepsilon_0 + 2\varepsilon_p) V_1 \ = \ 0 \tag{3.8}$$

In this example, it is clear that the FD mesh does not conform to the material interface. To demonstrate the accuracy of FLAME, it is meaningful to use results based on conventional FD for comparison. In this thesis, all FD calculations are based on the flux balance, which is introduced in this section.

3.3 The Trefftz-FLAME Schemes

Now let's go to the FLAME method. As discussed in Section 3.1, FLAME replaces the Taylor expansions of classical FD calculus with more accurate approximating functions. In the main version of FLAME, these functions are the local analytical solutions of local problem that includes one or none particle, which takes account the interface boundaries mentioned in Section 3.1.

Conceptually, one considers a set of overlapping patches ($\Omega^{(i)}$) covering the computational domain $\Omega = \cup\Omega^{(i)}, i = 1, 2, ..., n$ (Figure 3.3). The solution is approximated locally over each patch. Associated with each patch $\Omega^{(i)}$ ia a local approximation space,

$$\Psi^{(i)} \ = \ \mathrm{span}\{\psi_\alpha^{(i)}\}, \quad \alpha = 1, 2, \ldots m \tag{3.9}$$

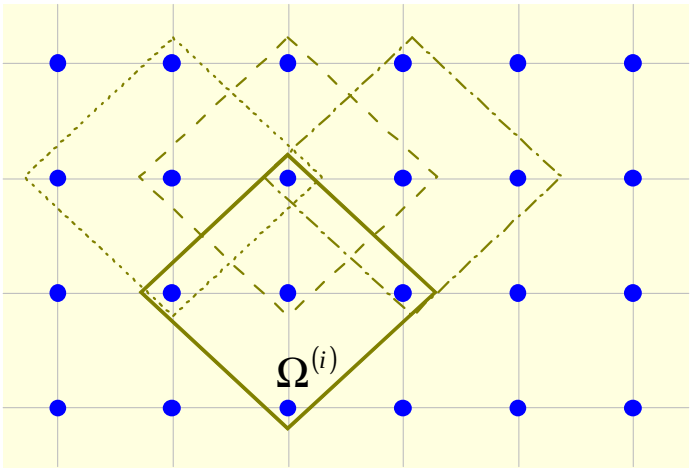

Figure 3.3: The stencil of one FLAME scheme example.

Here m is the number of approximating functions. The local solution $u_h^{(i)}$ in space $\Omega^{(i)}$ is a linear combination of the local basis functions $\psi_\alpha^{(i)}$.

$$u_h^{(i)} = \sum_{\alpha=1}^{m} c_\alpha^{(i)} \psi_\alpha^{(i)} \tag{3.10}$$

The definition of these basis functions depends on the specific physical problem, which will be illustrated by several examples in Section 3.6. For the time being, let us assume that the basis functions $\psi_\alpha^{(i)}$ have been determined. By relating the coefficient vector $c^{(i)} \equiv c_\alpha^{(i)}$ to the vector $u^{(i)} \equiv u_\alpha^{(i)}$, we can get

$$u^{(i)} = N^{(i)} c^{(i)} \tag{3.11}$$

where matrix $N^{(i)}$ comprises the nodal values of the basis functions on the patch.

$$N^{(i)} = \begin{pmatrix} \psi_1^{(i)}(r_1) & \psi_2^{(i)}(r_1) & \dots & \psi_m^{(i)}(r_1) \\ \psi_1^{(i)}(r_2) & \psi_2^{(i)}(r_2) & \dots & \psi_m^{(i)}(r_2) \\ \dots & \dots & \dots & \dots \\ \psi_1^{(i)}(r_M) & \psi_2^{(i)}(r_M) & \dots & \psi_m^{(i)}(r_M) \end{pmatrix} \tag{3.12}$$

The vector $\underline{s} \in R^M$ of the difference FLAME scheme is sought to yield

$$s^{(i)^T} u^{(i)} = 0 \tag{3.13}$$

Together with (3.11),

$$s^{(i)^T} N^{(i)} c^{(i)} = 0 \tag{3.14}$$

For this to hold for any set of coefficients $c^{(i)}$, $s^{(i)}$ can be calculated as [23]

$$\underline{s}^{(i)} \in \text{Null}(N^{(i)T}) \tag{3.15}$$

In other words, the coefficient vector of the FLAME scheme is in the null space of the nodal matrix. Typically, for the null space to be one-dimensional (thereby defining the scheme uniquely), the number of basis functions should be one less than the number of stencil nodes M. For example, four and eight basis functions are typically needed for the five- and nine-point FLAME schemes in 2D.

So far, the discussion is only for homogeneous governing equations. As for Inhomogeneous equations (i.e. with a nonzero right hand side) of the generic form,

$$\mathcal{L}u = f \tag{3.16}$$

they are handled by introducing a local splitting.

$$u^{(i)} \;=\; u_0^{(i)} \;+\; u_f^{(i)} \tag{3.17}$$

Here $u_f^{(i)}$ can be any particular solution of the inhomogeneous equation. $u_0^{(i)}$ is the solution of the homogeneous equation. The choice of $u_f^{(i)}$ depends on the specific physical problem (the 2D Poisson equation serves as an example in Section 3.6.2). Then,

$$\mathcal{L}u_0^{(i)} \;=\; 0; \qquad \mathcal{L}u_f^{(i)} \;=\; f \tag{3.18}$$

For the homogeneous solution, the coefficient vector $\underline{s}^{(i)}$ can be calculated by (3.15). Then the inhomogeneous FLAME scheme is

$$\underline{s}^{(i)T}\underline{u}^{(i)} \;=\; \underline{s}^{(i)T}\underline{u}_f^{(i)} \tag{3.19}$$

In the presence of sources in the vicinity of a given grid stencil, the right hand side of (3.19) is formed, as indicated, by applying the differential operator to the nodal values of the particular solution $u_f^{(i)}$.

The construction of Trefftz-FLAME scheme can be summarized as follows.

1. Generating regular grids and forming a set of overlapping patches.
2. Finding, for each patch, a set of local basis functions satisfying the governing differential equations and interface boundary conditions.
3. Computing the nodal matrix $N^{(i)}$ of the basis functions.
4. Generating the difference scheme by finding the null space of $N^{(i)T}$.

3.4 Trefftz FLAME Schemes of Varying Order

The accuracy of FLAME and the order of approximation depend on the grid stencil chosen. In 2D, the five- and nine-point stencils are especially popular (Figure 3.4). Similarly, in 3D seven- and nineteen-point stencils are commonly used (Figure 3.5).

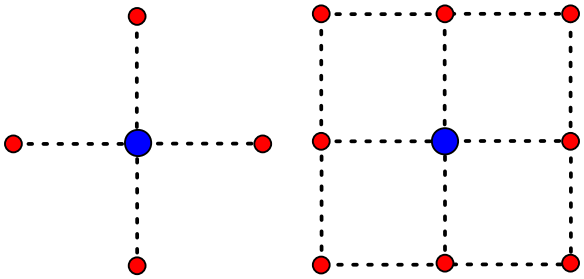

(a) Five-point stencil. (b) Nine-point stencil.

Figure 3.4: 2D Standard FLAME stencils.

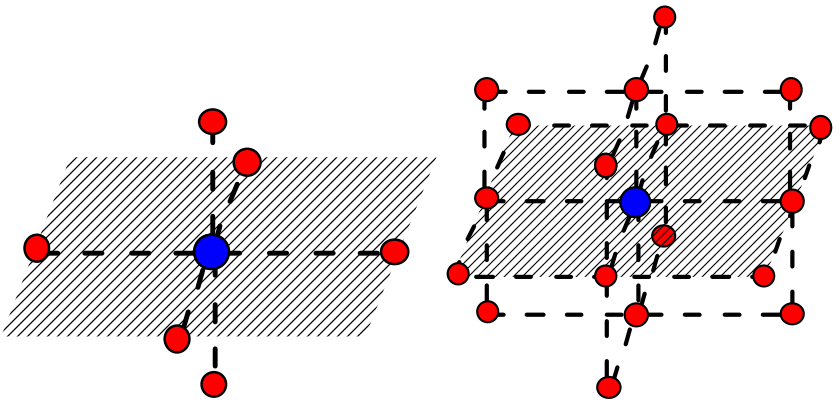

(a) Seven-point stencil (b) Nineteen-point stencil

Figure 3.5: 3D Standard FLAME stencils.

3.5 The Treatment of Boundary Conditions

For different patches, the FLAME approximations are completely independent. At the domain boundaries in particular, any standard FD schemes can be used. Alternatively, it may be possible to incorporate special features into the scheme at the boundary if such features are known [21].

3.6 Case Studies for Trefftz FLAME

The Trefftz FLAME basis functions depend on the governing equations of the specific physical problem. For illustrative purposes, several examples are given below. We start with simple 1D problems to fix ideas.

3.6.1 1D Laplace and Helmholtz Equations

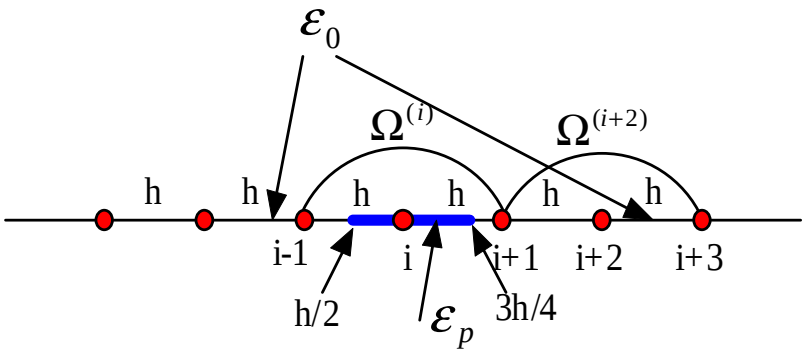

Figure 3.6: Sample problem for 1D Laplace equation with uniform distribution of nodes.

Consider a 1D electrostatic problem with two dielectrics (ε_0 and ε_p, Figure 3.6). Within each material, the electrostatic potential is governed by the Laplace equation.

$$u_{xx} = 0; \tag{3.20}$$

A regular Cartesian mesh is shown in Figure 3.6, and a three-node stencil is chosen. The two basis functions satisfying the Laplace equation, $\psi_1 = 1$ and $\psi_2 = x$, are chosen for the three-node patch. Then the numerical approximation over the patch is $u_h = c_1\psi_1 + c_2\psi_2$.

First, let us choose the $(i+2)th$ patch (including nodes $i+1$, $i+2$ and $i+3$), and the $(i+2)th$ node is treated as the origin of the Cartesian system. In this case, the three chosen nodes are located in the domain with unique material. The nodal matrix $N^{(i)}$ comprises the nodal values of basis functions ($\psi_1 = 1$, $\psi_2 = x$):

$$N^{(i)} = \begin{pmatrix} 1 & +h \\ 1 & 0 \\ 1 & -h \end{pmatrix} \tag{3.21}$$

The null space of $N^{(i)T}$ yields the Trefftz FLAME scheme as [1, -2, 1], which coincides with the standard three-node scheme for the Laplace equation.

Now let us consider a more complex example, with the ith patch (including nodes $i-1$, i and $i+1$) chosen, and assume $\varepsilon_p = 10\varepsilon_0$. For simplification, the ith node is treated as the origin of the Cartesian coordinate system. To construct a FLAME scheme, one starts with the basis functions for this patch. These basis

functions satisfy not only the governing equation, but also the boundary conditions of the interface Γ.

$$u_{in}|_{x=x_0} = u_{out}|_{x=x_0} \quad on\ \Gamma, \tag{3.22}$$

$$\varepsilon_p \frac{\partial u_{in}}{\partial x}|_{x=x_0} = \varepsilon_0 \frac{\partial u_{out}}{\partial x}|_{x=x_0} \quad on\ \Gamma, \tag{3.23}$$

Here x_0 is the coordinate of the interface, which is $-\frac{h}{2}$ for the left interface, and $\frac{3h}{4}$ for the right interface in the example. We first choose the basis functions for the section with ε_p as $\psi_1 = 1$ and $\psi_2 = x$. Then, the basis functions of ε_0 sections are calculated as $\{\psi_1 = 1, \psi_2 = 10x - \frac{27h}{4}\}$ in the right part, and $\{\psi_1 = 1, \psi_2 = 10x + \frac{9h}{2}\}$ in the left part through the boundary conditions. The corresponding nodal matrix $N^{(i)}$ is calculated as

$$N^{(i)} = \begin{pmatrix} 1 & +\frac{13h}{4} \\ 1 & 0 \\ 1 & -\frac{11h}{2} \end{pmatrix} \tag{3.24}$$

The Trefftz FLAME scheme then is $\mathrm{Null}(N^T)$ = [1.6923 -2.6923 1]. Because this scheme comes from the analytical solution, it represents that solution perfectly even though the mesh is not geometrically conforming to the interface boundary.

Another example, still for the 1D Laplace equation, is shown in Figure 3.7, and illustrates that FLAME grid does not need to be uniform. The same procedure as above is used to calculate the scheme of ith patch. The nodal matrix then is

$$N^{(i)} = \begin{pmatrix} 1 & +\frac{h}{2} \\ 1 & 0 \\ 1 & -h \end{pmatrix} \tag{3.25}$$

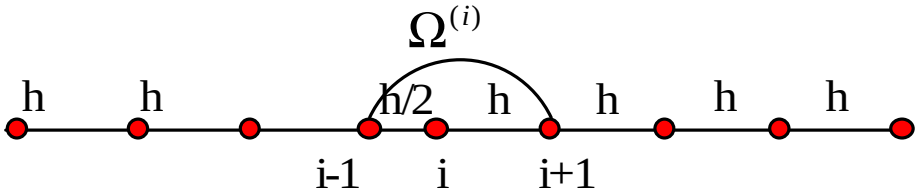

Figure 3.7: Sample problem for 1D Laplace equation with nonuniform distribution of nodes.

The scheme is calculated as $\mathrm{Null}(N^T)$ = [2, -3, 1]. This forms the basis of adaptive FLAME, and the much more complicated algorithms and meshes will be introduced in Chapter 4.

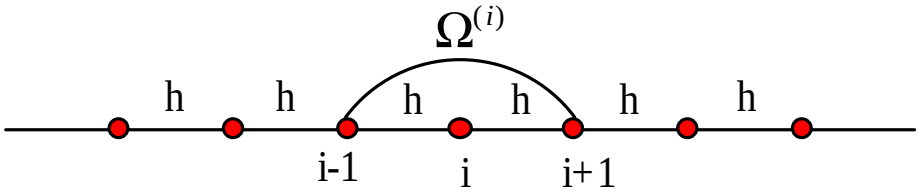

Figure 3.8: Sample problem for 1D Helmholtz equation.

The examples above are all for the Laplace equation. Now let us consider the problem governed by the 1D Helmholtz equation.

$$u_{xx} + \kappa^2 x \;=\; 0 \tag{3.26}$$

where κ is a given parameter. As Figure 3.8 shows, a series of nodes is generated. Two basis functions satisfying the Helmholtz equation are $\psi_1 = \cos(\kappa x)$ and $\psi_2 = \sin(\kappa x)$. For the ith patch (assuming the coordinate value for ith node is 0), the

nodal matrix is as

$$N^{(i)} = \begin{pmatrix} cos(\kappa h) & sin(\kappa h) \\ 1 & 0 \\ cos(-\kappa h) & sin(-\kappa h) \end{pmatrix} \tag{3.27}$$

The corresponding Trefftz-FLAME scheme is $\text{Null}(N^T) = [1 - 2cos(\kappa h)1]$.

3.6.2 2D Laplace, Poisson and Helmholtz Equations

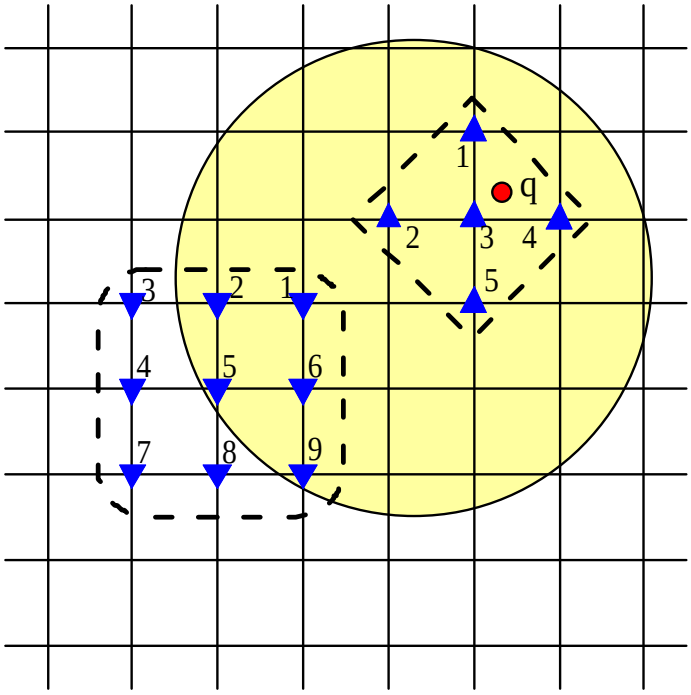

Figure 3.9: Five-node and nine-node stencils for the 2D Laplace and Poisson equations.

A 2D electrostatic example - a circular particle with permittivity ε_p in a vacuum (ε_0)- is shown in Figure 3.9. A point charge is located inside the particle.

The governing equations are,

$$\mathcal{L}u \;=\; -\nabla\cdot\varepsilon_p\nabla u \;=\; \sum_{\alpha} q_\alpha\delta_\alpha \qquad Inside\ the\ particle \tag{3.28}$$

$$\mathcal{L}u \;=\; -\nabla\cdot\varepsilon_0\nabla u \;=\; 0 \qquad Outside\ the\ particle \tag{3.29}$$

One five-node stencil and one nine-node stencil are chosen to demonstrate the construction of FLAME schemes

For the five-node stencil (dashed diamond in Figure 3.9), the presence of a point charge makes the equation inhomogeneous (nonzero r.h.s.). As discusses in Section 3.3, FLAME scheme is first constructed for the respective homogeneous equation. In this problem, the basis functions for the five-point FLAME scheme can be chosen as $[1,\ x,\ y,\ x^2-y^2]$. Then the nodal matrix for this patch is (node #3 is treated as the origin of 2D Cartesian coordinates and the grid length is h in both X and Y direction):

$$N^{(i)} \;=\; \begin{pmatrix} 1 & \frac{-h}{2} & \frac{h}{2} & 0 \\ 1 & \frac{-3h}{2} & \frac{-h}{2} & 2h^2 \\ 1 & \frac{-h}{2} & \frac{-h}{2} & 0 \\ 1 & \frac{h}{2} & \frac{-h}{2} & 0 \\ 1 & \frac{-h}{2} & \frac{-3h}{2} & -2h^2 \end{pmatrix} \tag{3.30}$$

The corresponding FLAME scheme is [1 1 -4 1 1], which is the same as the standard five-point FD scheme.

For the inhomogeneous equation (nonzero source within or in the vicinity of the patch), any particular solution $u_f^{(i)}$ of the inhomogeneous equation is needed. In this problem, this solution is given simply by

$$u_f \;=\; \frac{q}{2\pi\varepsilon_p}\ln r \tag{3.31}$$

This gives the FLAME scheme in accordance with equation (3.19).

In (3.31), r cannot be zero because of the logarithmic term. Therefore there must be no grid node right at the charge. Otherwise, the singularity renders the FLAME scheme invalid. A similar requirement also exists in 3D.

Now let us consider the nine-node stencil. For the construction of a nine-point FLAME scheme, the four-function basis set for the five-point FLAME is amended by four additional functions $\{xy,\ x^3-3xy^2,\ y^3-3yx^2,\ x^4-6x^2y^2+y^4\}$. For a patch at an interface boundary, two harmonic functions in each of the materials can be written in the polar system and matched via the interface boundary conditions.

More specifically, the Laplace equation in polar coordinates [25] is

$$\mathcal{L}u \;=\; \nabla^2 u \;=\; \frac{1}{r}\frac{\partial}{\partial r}\left(r\frac{\partial u}{\partial r}\right)+\frac{1}{r^2}\frac{\partial^2 u}{\partial\theta^2} \;=\; 0 \tag{3.32}$$

The solution can be expressed by separation of variables:

$$u \;=\; \sum_{l=0}^{\infty}(A_l r^l + B_l r^{-l})(C_1\cos(l\theta)+C_2\sin(l\theta)) \tag{3.33}$$

where A_l, B_l, C_1, C_2 are coefficients to be determined via the boundary conditions. Assuming there is no free charge on the particle surface, these boundary conditions are:

$$u_{in}|_{r=r_0} \;=\; u_{out}|_{r=r_0} \qquad on\ \Gamma, \tag{3.34}$$

$$\varepsilon_p \frac{\partial u_{in}}{\partial n}|_{r=r_0} \;=\; \varepsilon_0 \frac{\partial u_{out}}{\partial n}|_{r=r_0} \qquad on\ \Gamma, \tag{3.35}$$

where n represents the normal direction.

Consider the basis function x (inside particle) as an example. Its form in the polar coordinates is $r\cos(\theta)$. The corresponding function in a vacuum, is of the form $(A_1 r + B_1 \frac{1}{r})\cos(\theta)$. Though the boundary conditions, the constants are calculated as $A_1 = \frac{\varepsilon_0+\varepsilon_p}{2\varepsilon_0}$ and $B_1 = \frac{\varepsilon_0-\varepsilon_p}{2\varepsilon_0} r_p^2$, where r_p is the radius of the circular particle. In the particular case of $\varepsilon_p = \varepsilon_0$, A_1 = 1 and B_1 = 0, and the function is the same as $r\cos(\theta)$.

Now consider the 2D Helmholtz equation, shown in Figure 3.10, for two domains with different κ. The interface boundary conditions are the same as in the previous example.

$$\nabla^2 u + \kappa^2 u = 0 \tag{3.36}$$

In the polar coordinates with the center of the particle taken as the origin, the analytical solution is

$$\begin{cases} \psi_\alpha^{(i)} = a_n J_n(k_p r) exp(in\theta), \;\; r \;\leq\; r_0 \\ \psi_\alpha^{(i)} = [b_n H_n^{(2)}(k_0 r) + H_n^{(1)}(k_0 r)] exp(in\theta), \quad r \;>\; r_0 \end{cases} \tag{3.37}$$

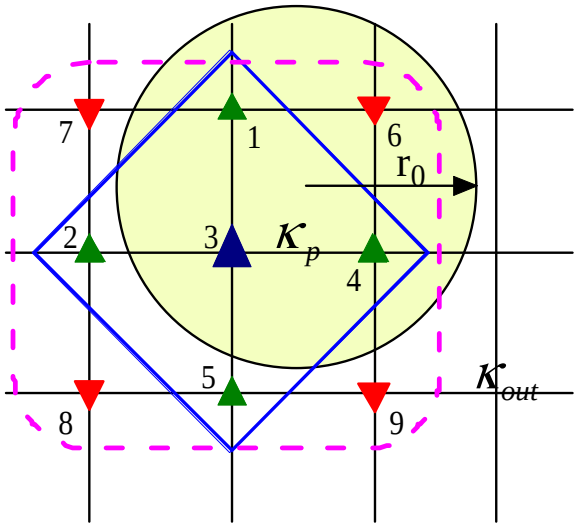

Figure 3.10: Five-node and nine-node stencils for the 2D Helmholtz equation.

where J_n is the Bessel function, $H_n^{(1)}$ and $H_n^{(2)}$ are the Hankel functions of the first and second kinds. a_n and b_n are coefficients to be determined. These coefficients can be found according to the standard conditions of the interface between the circular particle and the outer region.

To construct a five-point FLAME scheme, four basis functions are chosen: the monopole harmonic ($n = 0$), two harmonics of order 1 ($n = 1$), and one harmonic of order 2 ($n = 2$). For the eight-point FLAME scheme, in addition to the four functions for five-point FLAME, another four functions are needed. They can be the other harmonic of order 2 ($n = 2$), two harmonics of order 3 ($n = 3$), and one harmonic of order 4 ($n = 4$). With these basis functions, it is easy to generate the nodal matrices $N^{(i)}$ for any five-point patch or nine-point patch. The corresponding scheme is again the null space of N^T.

3.6.3 3D Laplace and the Linearized Poisson-Boltzmann Equations

So far we have described examples of 1D and 2D problems. This section covers a few 3D cases. FLAME schemes for the Laplace equation in 3D are found in complete analogy with the 2D case. For the standard seven-point stencil within uniform domain, six basis functions $\{1,\ x,\ y,\ z,\ x^2-y^2, -x^2-z^2\}$ are used to construct the scheme. The corresponding FLAME scheme is calculated to be [1, 1, 1, -6, 1, 1, 1], which coincides with the standard FD scheme. For the nine-point stencil (a 3×3 cluster of nodes), another 12 basis functions are added: $\{xy,\ xz,\ yz,\ x^3-3xy^2,\ y^3-3x^2y,\ x^3-3xz^2,\ z^3-3x^2z,\ y^2-3yz^2,\ z^3-3y^2z,\ x^4-6x^2y^2+y^4,\ x^4-6x^2z^2+z^4,\ y^4-6y^2z^2+z^4\}$.

A more complex example is a spherical particle immersed in a solvent. The potential inside the particle is governed by the Laplace equation. The region outside the particle is governed by the linearized Poisson-Boltzmann equation (see Chapter 6).

$$\nabla^2 u - \kappa^2 u = 0 \tag{3.38}$$

As for the linearized Poisson-Boltzmann equation, it will be introduced specifically in Chapter 6. For this problem, FLAME basis functions are written in the spherical coordinates:

$$\psi_{mn} = \begin{cases} P_n^m(\cos\theta)\exp(\mathrm{i}m\phi)r^n \quad \text{Region inside particle} \\ P_n^m(\cos\theta)\exp(\mathrm{i}m\phi)(f_{mn}j_n(\mathrm{i}kr) + g_{mn}n_n(\mathrm{i}kr)) \quad \text{Region outside particle} \end{cases} \tag{3.39}$$

Here $P_n^m(\cos\theta)$ is the associated Legendre polynomials, $j_n(z) = (\pi/(2z))^{1/2} J_{n+1/2}(z)$ and $n_n(z) = (\pi/(2z))^{1/2} Y_{n+1/2}(z)$ are the spherical Bessel functions of the first and second kinds, respectively. They are expressible in terms of the hyperbolic sine and cosine functions and are therefore fairly easy to work with. The coefficients c_{mn}, d_{mn}, f_{mn}, g_{mn} are found through the interface boundary conditions [15].

Chapters 4, 5 and 6 will cover several types of problems closely related to the above illustrative examples for FLAME schemes. Other applications of FLAME are considered in [15, 16, 22].

3.7 Conclusion

FLAME is a generalized FD calculus that generates FD schemes on regular grids (and even meshless versions of FLAME are possible [21]). In FLAME, the computational domain is covered by a system of overlapping patches. Within each patch, local basis functions satisfying the governing differential equation are found analytically, semi-analytically or numerically. The coefficients of the difference scheme are calculated as the null space of the nodal matrix as equation (3.15).

The construction of FLAME scheme depends on the specific physical problem. The examples of this chapter serve as a demonstration. In the following chapters, a number of practical applications are presented. In the future, FLAME could be extended to other classes of problems. Of particular interest are schemes for Maxwell equations in the time domain and schemes for nonlinear problems.

CHAPTER IV

ELECTROSTATIC PARTICLE INTERACTIONS IN SIMPLE DIELECTRIC MATERIALS

FLAME is applied to simulate electrostatic interactions in 2D and 3D electrostatic multiparticle problems. This chapter describes the calculation of the potential, electric field and force. Two approaches, analytical/numerical bases and adaptive mesh refinement, are developed to improve the accuracy when there are several particles in close proximity to one another.

4.1 Introduction

Electrostatic and magnetostatic multiparticle problems are important for the simulation of colloidal systems, polymers, macromolecules, magnetically driven assembly, drug delivery, and other applications [26, 27]. When these problems extend to the nanoscale, the number of objects in the system is usually significant. For this type of problem, conventional numerical methods have serious limitations. For example, the FEM requires geometrically conforming meshes that become extremely complex because of the large number of objects. The FMM is not effective either for dielectric/magnetic particles of finite size or for nonlinear problems.

FLAME was presented in detail in Chapter 3. The electrostatic problems can serve as models for testing this new computational technique. The following sections discuss the applications of FLAME to both 2D and 3D electrostatic multiparticle problems.

4.2 Case 1: Well-Separated Particles in 2D

2D multiparticle problems, being less complex than 3D ones, provide a good initial test for FLAME. 3D applications are considered in sections 4.4 and 4.5. Before presenting more realistic examples, it is helpful to separate the multiparticle problems into two cases. In the first case, any pair of particles are "well-separated" in the sense that the gap between them is greater than the mesh size. In the second case ("poorly-separated" particles), one or more such gaps are comparable to or smaller than the mesh size. This section deals with the case of well-separated particles, and the following section is for poorly-separated particles.

For definiteness, consider a 2D example with ten circular dielectric particles in a homogeneous dielectric medium (Figure 4.1). All particles have the same radius that is for convenience normalized to unity. The electrostatic potential is governed by the Laplace equation both inside and outside the particles, with standard boundary conditions [7] for the potential and its normal derivative across particle boundaries.

In the test example, the computational domain is chosen as a square 16×16, where the particles are placed quasi-randomly. To ensure sufficient gaps between

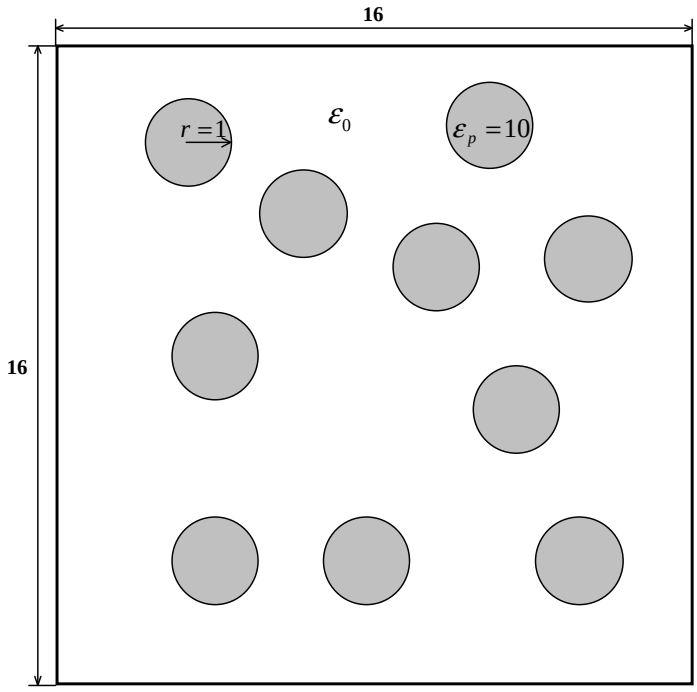

Figure 4.1: Geometric setup of the electrostatic well-separated multiparticle with ten particles. All particles have the same radius, for convenience normalized to unity.

them in the case with well-separated particles under consideration, the distance between any two particles (center to center) is set to be greater than 3 times the particle radius. The relative dielectric constants of all particles are chosen as 10. The medium around the particles is air. A uniform external field is applied. To eliminate the numerical error associated with the approximation of boundary conditions, the exact Dirichlet boundary condition is imposed on the outer boundary, as described in the following subsection.

4.2.1 Quasi-Analytical solution for the 2D Multiparticle Problem

For the 2D problem with a limited number of circular particles, the multipole-multicenter expansion can be used to obtain a quasi-analytical solution. This method is based on the binomial expansion [28] that can be used to translate the potential in one polar coordinate system to another polar system. This expansion is represented by the equation

$$(r - r')^n = \sum_{k=-\infty}^{\infty} \begin{pmatrix} \upsilon \\ k \end{pmatrix} r^k r'^{(n-k)} \tag{4.1}$$

where $\begin{pmatrix} \upsilon \\ k \end{pmatrix}$ is the binomial coefficient. The r and r' are radial coordinate values of the two polar coordinate systems and n is an arbitrary integer.

For the multipole-multicenter expansion, the global potential is the summation of all the potentials that related to all particles, plus the external field applied. Here, the potential related to particle is referred to as the *local potential*. The local potential related to particle p can be expanded into cylindrical harmonics.

$$u = \begin{cases} \sum_{i=0}^{\infty} g_{ip}(r_p e^{i\theta_p}) & Inside\ particle\ p \\ \sum_{i=0}^{\infty} d_{ip}(r_p e^{-i\theta_p}) & Outside\ particle\ p \end{cases} \tag{4.2}$$

Here, g_{ip} and d_{ip} are the coefficients that need to be determined, and r_p and θ_p are the coordinate values in the polar system, with the origin at the center of the particle p. The corresponding boundary conditions at the particle interface boundary Γ can be used to determine the coefficients g_{ip} and d_{ip}.

According to (4.2), there are two equations corresponding to each harmonic of one particle, one for the inside area and the other one for the outside area. If there are m particles altogether, then $2m$ equations are needed for each harmonic. If n harmonics are useed, the total number of equations is $n \times 2m$. Knowing the applied external field, the coefficients g_{ip} and d_{ip} can be calculated based on these equations. After these calcuations are made, the local potential related to each particle is obtained. Further, the global potential is calculated. Assuming there are total number of particles are q, the global potential distribution will be

$$\phi = \begin{cases} \phi_{ext} + \sum_{i=0}^{\infty} g_{ip}(r_p e^{i\theta_p}) + \sum_{j=1,j\neq p}^{q} \sum_{i=0}^{\infty} d_{ij}(r_j e^{i\theta_j}) & Inside\ particle\ p \\ \phi_{ext} + \sum_{j=1}^{q} \sum_{i=0}^{\infty} d_{ij}(r_j e^{-i\theta_j}) & Outside\ all\ particles \end{cases} \tag{4.3}$$

In practice, the potential converges rapidly as the number of harmonics increases. For all 2D multiparticle problems in this chapter, the harmonics are truncated at the term when the magnitude of the corresponding potential is 10^{-10} to obtain a quasi-exact solution for verification purposes.

4.2.2 Potential Calculation of Mesh Nodes

When FLAME is applied to the 2D electrostatic multiparticle problem, part of the procedure is the same as for the conventional FD method. Regular Cartesian grids are typically used. FLAME schemes for each grid stencil are generated as described in Chapter 3. This leads to a system of algebraic equations with a sparse matrix; the sparsity structure of this matrix is the same as it would be for the conventional FD

on the same grid stencils. The system of equations is solved to obtain the potential at the grid nodes.

The relative root mean square error (RMSE) is used to evaluate the numerical accuracy in this chapter.

$$relative\ RMSE\ =\ \frac{\sqrt{\sum \left(F(m) - \hat{F}(m)\right)^2}}{\sqrt{\sum F^2(m)}} \tag{4.4}$$

Here, $F(m)$ is the theoretical result and $\hat{F}(m)$ is the numerical result.

The numerical accuracy of the nodal potentials are plotted on the logarithmic scale as a function of the number of nodes, *n*, as shown in Figure 4.2. For comparison, the accuracy plots for standard five-point FD based on the flux balance, as well as first order and second order FEMs are also provided. The vertical axis shows the relative RMSE, which includes all the mesh nodes inside the domain (excluding the boundary nodes). In Chapters 4 and 5, all the FEM calculation results are obtained with the commercial software package, COSMOL Multiphysics. This software is a powerful, interactive environment for FE modeling of scientific and engineering problems.

From Figure 4.2, it can be seen that the order of convergence of the five-point FLAME scheme is approximately $\mathcal{O}(n^{-0.6})$, which is similar to that of the five-point FD. However, the accuracy of the five-point FLAME is about ten times higher than the accuracy of the five-point FD. Further, for a small number of nodes, the accuracy of the five-point FLAME is greater than the accuracy of the first order FEM.

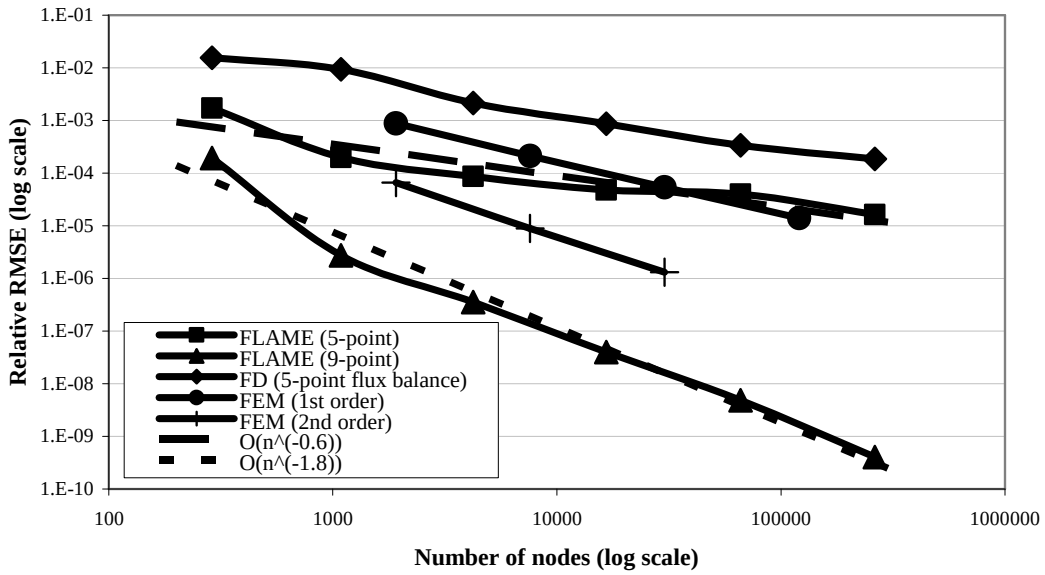

Figure 4.2: Numerical accuracy of the nodal potentials for the 2D electrostatic multiparticle problem with well-separated particles.

Among all methods, the nine-point FLAME has the highest accuracy and the highest order of convergence ($\mathcal{O}(n^{-1.8})$).

4.2.3 Potential Interpolation

The result in Section 4.2.2 is limited to the potentials at mesh nodes. It would be more useful if we were able to obtain the potential at any point in the geometry with a high level of accuracy. Referring to equation (3.10), it is clearly seen that the potential of any point in a given patch can be approximated by a linear combination of the basis functions. Therefore, to determine the corresponding potential value at any point, the patch that the point belongs to needs to be found and the coefficient series, $c_\alpha^{(i)}$, based on the nodal potentials of the patch needs to be calculated.

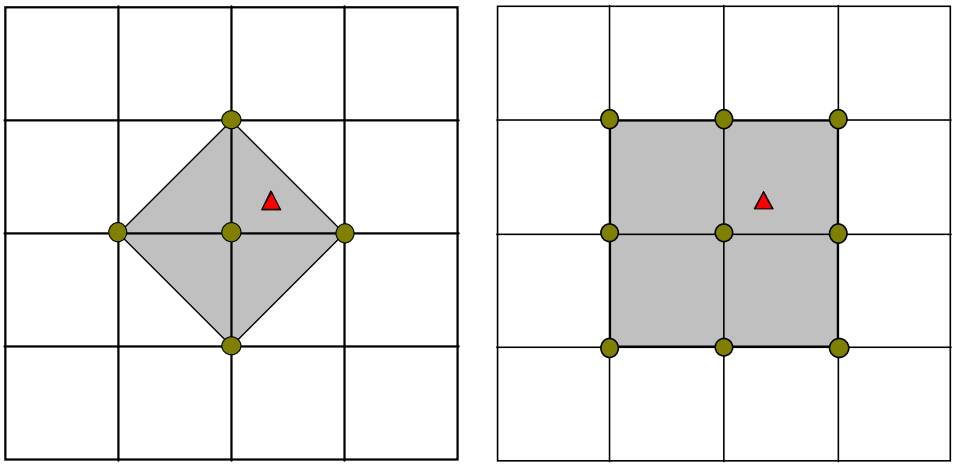

(a) Regular 5-point FLAME (b) Regular 9-point FLAME

Figure 4.3: Potential interpolation for the FLAMEs.

Figure 4.3 presents an example of a patch to which the interpolation point (triangle in the figure) belongs, for both five-point and nine-point schemes. The gray parts are the local patches chosen for interpolation because their centers are closest to the interpolation point. By moving the matrix $N^{(i)}$ from the right to the left in equation (3.11) of Chapter 3, the coefficient series is calculated by dividing the potential vector of the nodes in the patch into the matrix $N^{(i)}$, which can be got based on the basis functions for the patch. Then, the interpolation potential can be calculated by this coefficient series and the basis functions.

In the 2D electrostatic multiparticle model shown in Figure 4.1, 1000 sampling points are chosen randomly in the computational domain for testing. Figure 4.4 shows the interpolation errors at these sampling points. The errors of the nodeal potentials are included for comparison. For both five-point and nine-point

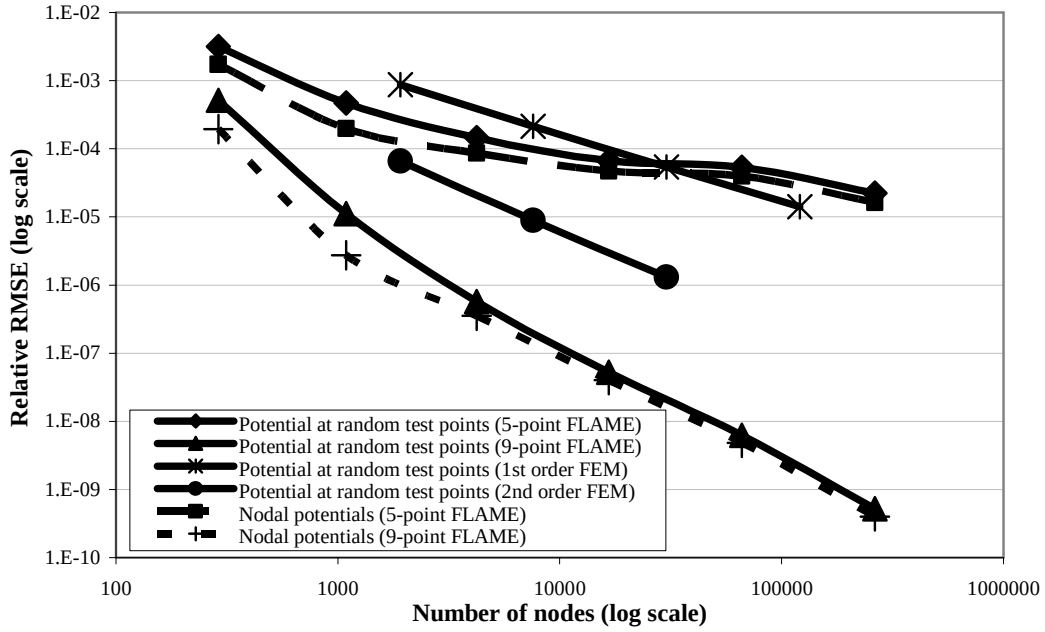

Figure 4.4: Numerical accuracy of the potential interpolation for the 2D electrostatic multiparticle problem with well-separated particles.

FLAME schemes, the interpolation accuracy at random points is comparable with that of the nodal potentials, especially for finer meshes. Furthermore, the accuracy of the nine-point FLAME is much greater than the accuracy of other numerical schemes, such as five-point FLAME, first and second order FEMs.

4.2.4 Electric Field Interpolation at Random Points

The same approach as above is applied to the interpolation of the electric field at any point in the domain. The relationship between the potential and the electric field is

$$E = -\nabla u \tag{4.5}$$

Since the potential can be expressed by a linear combination of the FLAME basis functions, the electric field will be the corresponding linear combination of the gradients of the basis functions. Combining equations (4.5) and (3.10), one writes the electric field as

$$\tilde{E} \;=\; -\nabla \sum_{k=1}^{n} c_k \psi_k \;=\; \sum_{k=1}^{n} (-c_k \nabla \psi_k) \tag{4.6}$$

To demonstrate the accuracy of this electric field interpolation, the same 1000 sampling points as in Section 4.2.3 are used for testing.

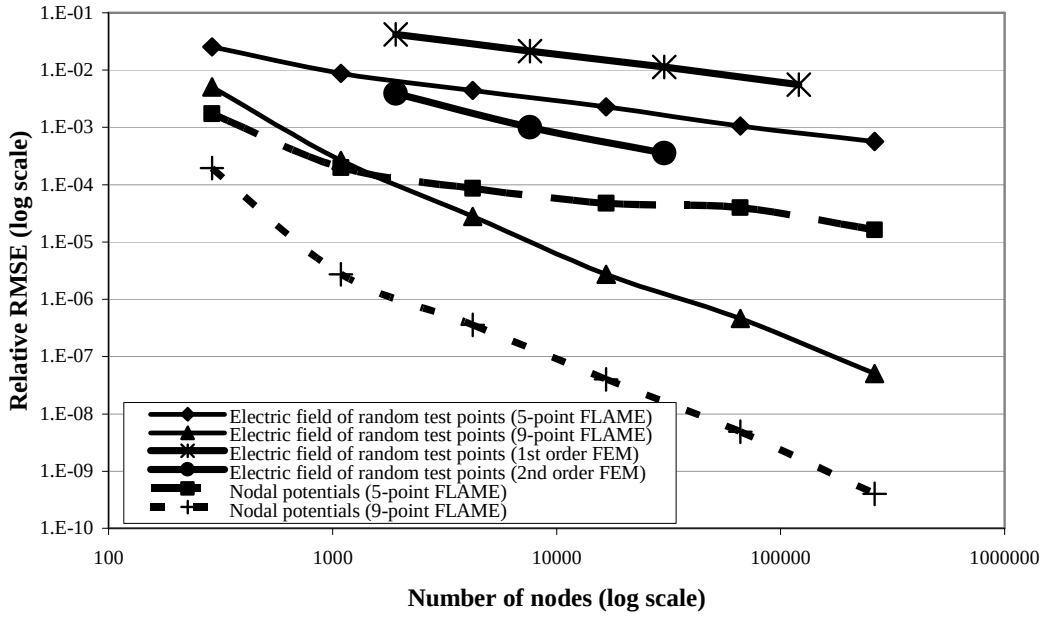

Figure 4.5: Numerical accuracy of the electric field interpolation for 2D electrostatic multiparticle problem with well-separated particles.

Figure 4.5 shows the electric field interpolation results for both five-point and nine-point FLAME schemes. The results of the mesh-node potentials are in-

cluded for comparison. The accuracy of the electric field interpolation for both five-point and nine-point schemes are about ten times lower than the accuracy of the mesh-node potentials. This accuracy loss for gradients is not surprising. The accuracy of the five-point FLAME in the field interpolation is much greater than the accuracy of first order FEM. The same conclusion is drawn by comparing the nine-point FLAME with second order FEM. Overall, FLAME produces more accurate values of the electric field at any point than FEM (five-point FLAME to first order FEM, nine-point FLAME to second order FEM).

4.2.5 Electromagnetic Force Calculation for Particles

There are two different approaches to the calculation of electromagnetic forces. The first one is based on the energy conservation, while the second one comes from direct source-field interaction, such as Coulomb's force on the dipole of equivalent magnetic charge and Lorentz's force on conduction or equivalent magnetization currents [29]. The Maxwell stress tensor [30], which belongs to the first category, is adopted in this section to calculate the electromagnetic forces among the particles.

In the calculation of 2D problems, the Maxwell stress tensor is given as

$$T = \begin{bmatrix} T_{xx}\ T_{xy} \\ \\ T_{yx}\ T_{yy} \end{bmatrix} = \begin{bmatrix} E_x^2 - \frac{E^2}{2} & E_x \cdot E_y \\ \\ E_y \cdot E_x & E_y^2 - \frac{E^2}{2} \end{bmatrix} \tag{4.7}$$

where E is the electrostatic field, x and y are the Cartesian coordinates.

The electromagnetic force acting on each particle can be calculated by the integration of the stress tensors:

$$\begin{cases} F_x &= \int_l T_{xx} n_x dl + \int T_{xy} n_y dl \\ F_y &= \int_l T_{yx} n_x dl + \int T_{yy} n_y dl \end{cases} \tag{4.8}$$

where n represents the normal direction. Computationally, equations (4.7) and (4.8) are found as numerical quadratures, as illustrated by examples below. To determine the accuracy of the force calculation, the quasi-exact value of the force is calculated using the Maxwell stress tensor for the semi-analytical electric fields (via the multipole-mutilcenter method) of 100,000 sampling points. These sampling points are the points even distributed in the circle path around one particle ($R = 1.1r$).

One important requirement for the integration path is that it must be a closed path outside the designated particle. In this section, a circlular path of radius d around a particles of radius r is chosen for the force calculation, as Figure 4.6 shows.

The force calculation shows that similar results can be obtained with different R as long as the condition $R > r$ is satisfied. The difference among calculations with $R = 1.01r, 1.1r, 1.2r$ are in 10^{-9}. For the calculations below, R is fixed as $1.1r$. To make numerical quadratures quasi-exact, the number of integration knots is chosen to be 40,000 for all of the calculations.

Figure 4.7 the results of five-point and nine-point FLAME schemes. The results of first and second order FEMs with the same number of integration points

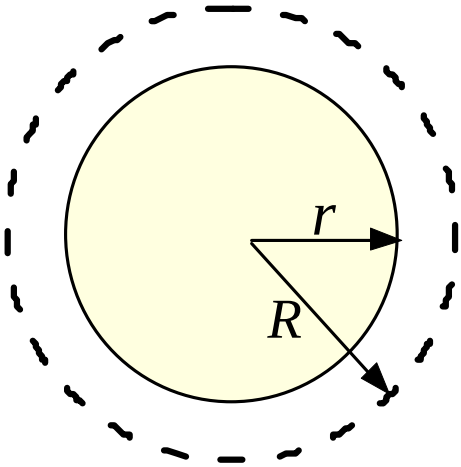

Figure 4.6: Field integration path for the force calculation.

are used for comparison. In general, the accuracy of the FLAME is higher than the accuracy of the FEM. Of all the calculations, the nine-point FLAME demonstrates the greatest accuracy. It is also found that the accuracy of force calculation is about ten times lower than the accuracy of the nodeal potentials, which is similar to the results of the electric field interpolation. This result is not surprising since the force calculation is based on electric fields that are less acurate than the potential.

4.3 Case 2: Poorly-Separated Particles in 2D

Calculations above are all for the 2D well-separated particles. Now let's go to the 2D poorly-separated particles. For these problems with poorly-separated particles, regular FLAME usually needs the side length of mesh grid is at most the smallest gap between two particles to get great accuracy. Therefore, the number of mesh nodes

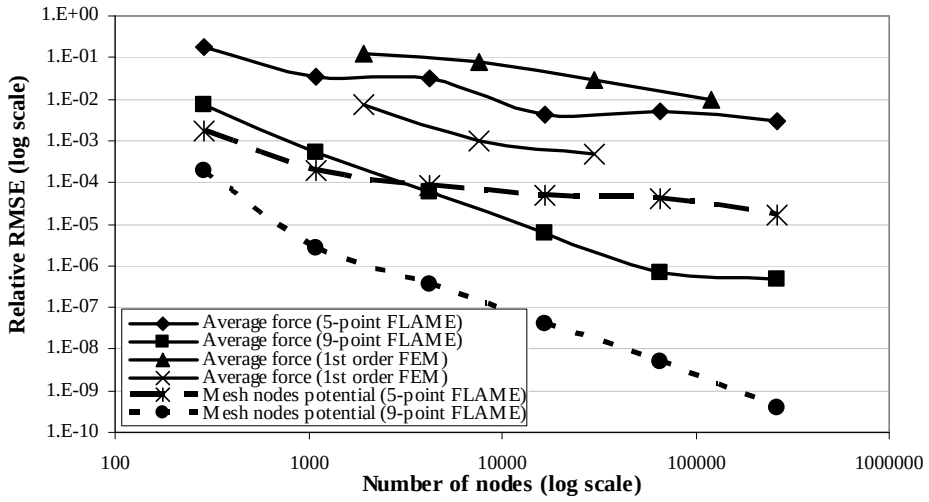

Figure 4.7: Numerical accuracy of the force calculation for the 2D electrostatic multiparticle model.

needs to be relatively large. This requirement makes regular FLAME computational impractical for the system that has a large number of components, unless some extra strategies are used.

4.3.1 An Illustration for Two Poorly-Separated Particles

Before discussing strategies for problems with poorly-separated particles, it first needs to be made clear why this situation leads to poor accuracy in regular FLAME. The FLAME scheme in the vicinity of any given particle is obtained by matching spherical harmonic expansions inside and outside the particle. This approach works well, but its area of applicability has limitations. If the shape of particles (or other dielectric objects) is not cylindrical or spherical, it is substantially more difficult to construct accurate local analytical approximations of the potential. Furthermore, if

two or more particles are separated by the distances (surface to surface) equal to or smaller than the grid size, the nodes associated with a patch may "belong" to different particles, as shown in Figure 4.8.

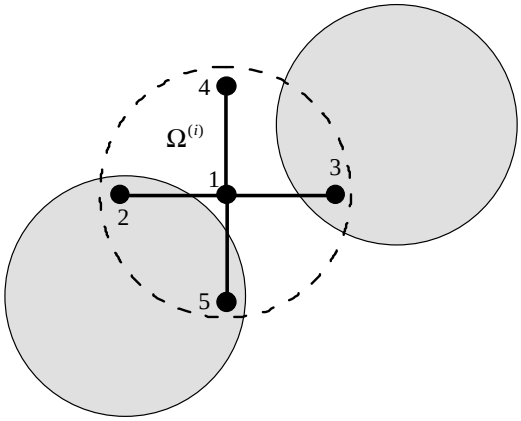

Figure 4.8: Patch $\Omega^{(i)}$ (dashed line) intersects two nearby particles.

A simple example of a pair of circular particles with the same radii is used to demonstrate the relationship between the numerical accuracy and the separation distance of the particles. As shown in Figure 4.9, two particles, with a gap d, have the same relative dielectric constant of 10. A uniform external field along the x-coordinate is applied. To determine the overall accuracy of the FLAME, the relative RMSE of potentials is calculated based on more than 1,000 randomly selected points.

To verify the numerical accuracy as a function of the separation distance, the grid size is fixed at one-quarter of the particle radius in both x and y directions, and the five-point FLAME is chosen for the sample calculation. Figure 4.10 shows

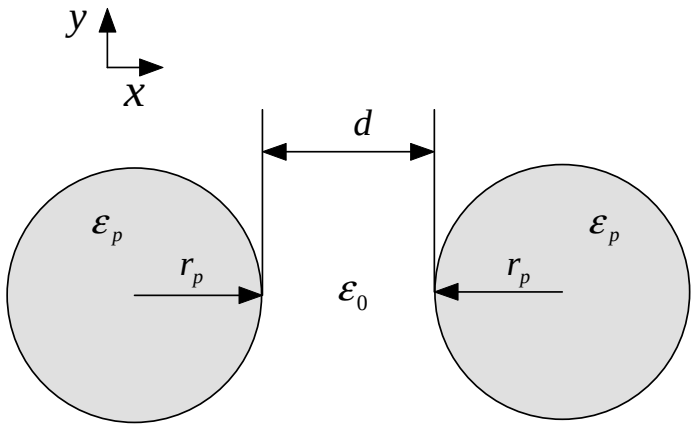

Figure 4.9: Example problem with two circular particles.

that the relative RMSE of potentials quickly increases with the decrease in the gap. When the gap is equal to r_p, the relative RMSE is only 0.089%, which proves that the regular FLAME works well as long as the particles are well-separated. When the gap diminishes to $0.125r_p$, which is relatively small compared to the grid size of $0.25r_p$, the relative RMSE increases by more than two orders of magnitude, to $\sim$23.2%. For this case, the particles are too close to each other for the local approximation based on just one of them to be physically meaningful.

The easiest method would be to refine the global mesh and to make the grid size smaller than the smallest gap. This method works for simple problems, such as the problem shown in Figure 4.9 when the gap is $0.125r_p$. However, for problems with a large number of particles, or with some of the gaps between the particles much smaller than their radii, refining the global mesh would increase the computational cost tremendously.

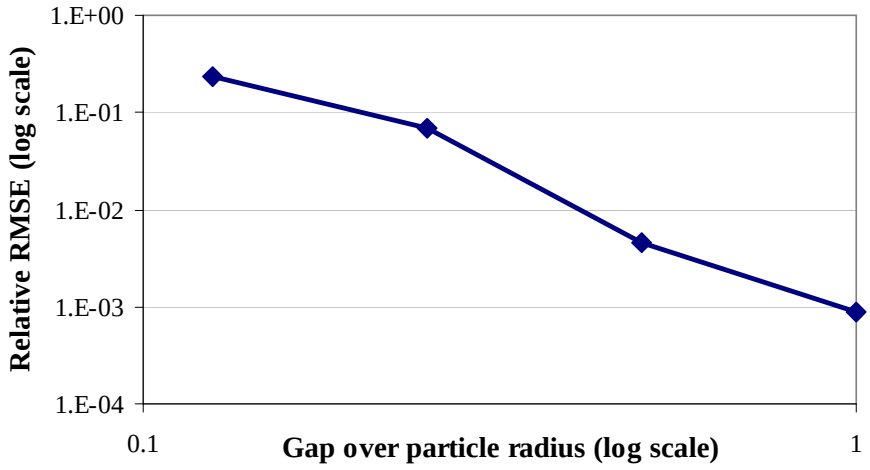

Figure 4.10: The relative RMSE as a function of the gap (expressed as a fraction of the radius).

4.3.2 Analytical vs. Numerical Bases

Two practical strategies for the FLAME, analytical/numerical bases and adaptive meshing, are proposed to improve the calculation accuracy by increasing relatively little computation complexity. The analytical/numerical bases FLAME treats a group of particles that are in close proximity to one another (compared with the grid size) as an auxiliary local problem and generates the corresponding FLAME bases, as shown in Figure 4.11. The local domain, which includes the clustered particles, is much smaller than the global domain, and therefore FLAME bases can be computed at a relatively low cost. Two ways for creating such bases are introduced in this section.

The multipole-multicenter expansion, which was introduced in Section 4.2.1, can produce analytical solutions to be used as the bases. On the other hand, in cases

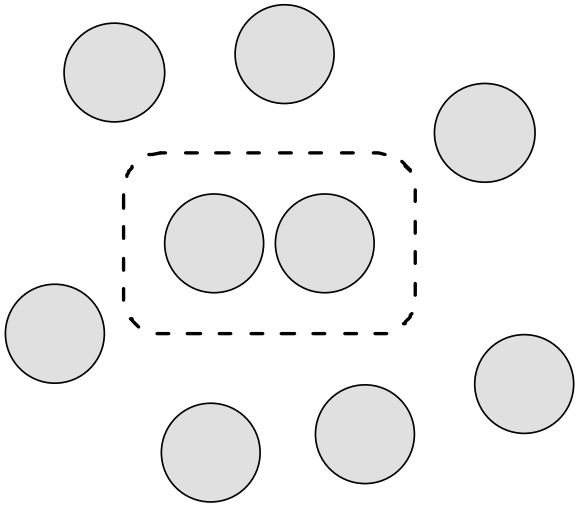

Figure 4.11: Local domain chosen for the analytical/numerical bases FLAME.

where local analytical approximations are unavailable, FLAME bases can be found as accurate *numerical* solutions of a local problem in the patch containing any given stencil. Among all traditional numerical methods, FEM is the most powerful tool that can be used toward this end. Solution of the local problem is relatively inexpensive because it does not require the construction of globally conforming FE meshes.

4.3.3 Adaptive FLAME

Adaptive FLAME refines the mesh locally in the areas where the particles are in close proximity to each other. Adaptive algorithms have a long history in FE analysis [31]. For FLAME, the computational domain is comprised of a system of overlapping patches. When two or more patches intersect, there is a discrepancy between the

potential interpolations. Once the grid is refined, this discrepancy is expected to diminish.

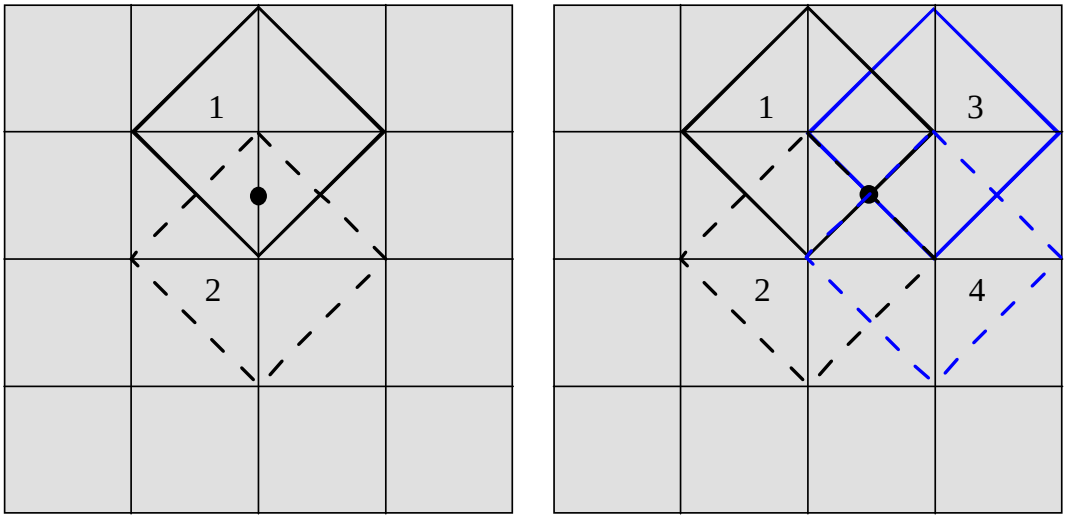

(a) Two overlapping patches (b) Four overlapping patches

Figure 4.12: Overlapping patches carrying the different local FLAME approximations (after [32], (c) 2008 IEEE).

More specifically, consider two overlapping patches, patch 1 and patch 2, as shown in Figure 4.12(a). The potential of the edge midpoint (black dot) can be interpolated using either patch 1 or patch 2, as explained in Section 4.2.3. The discrepancy between these two interpolated values at the edge midpoint may serve as an *a posteriori* error measure. One possible error indicator for a grid cell is the sum of the indicators at the four edge midpoints of the cell [32].

There are many other choices for error indicator. As shown in Figure 4.12(b), the nearest four patches can be used to interpolate the potential of the cell midpoint

(black dot). Either the standard deviation or the sum of the four interpolational discrepancies can be used as an error indicator for adaptive refinement.

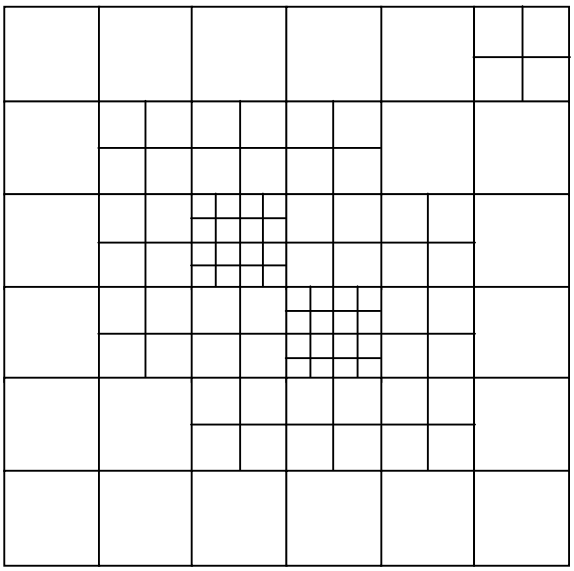

Figure 4.13: One-step *gradual* refinement strategy (after [32], (c) 2008 IEEE).

Although there are many choices for adaptive refinement strategies, one specific refinement strategy referred to as "One-step *gradual* refinement" is adopted here, as shown in Figure 4.13. Let the mean value of the error indicator over all cells be ϵ_{mean}. Cells with the indicator below ϵ_{mean} are not refined. Cells with the indicator in the range $[\epsilon_{\text{mean}}, 2\epsilon_{\text{mean}}]$ are subdivided into 2×2 subcells. Cells with the indicator in the range $[2\epsilon_{\text{mean}}, 3\epsilon_{\text{mean}}]$ are subdivided into 4×4 subcells, etc. To this end, for each cell subdivided into $2^l \times 2^l$ subcells, all neighboring cells are forced to be subdivided into at least $2^{l-1} \times 2^{l-1}$ subcells. Obviously, there are many possible variations of this strategy [32].

4.3.4 Numerical Results for Analytical/Numerical Bases FLAME

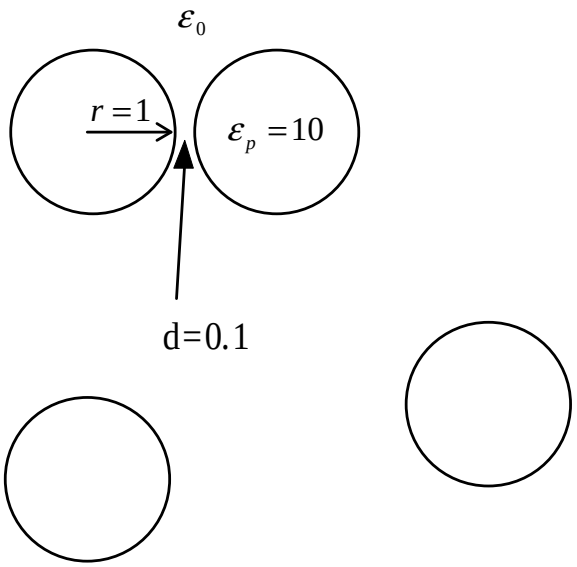

Figure 4.14: A 2D model with four particles for analytical/numerical bases FLAME.

The analytical/numerical bases FLAME is tested with the sample problem shown in Figure 4.14. The particles in the air have the relative dielectric constant $\epsilon_{\mathrm{p}} = 10$. A uniform external field is applied. All particles have the same radius that is normalized to unity. To eliminate the numerical error associated with the approximation of global boundary conditions, the semi-analytical (multipole-multicenter) Dirichlet condition is applied on the domain boundary. In this model, the two closest particles, which have the gap of one tenth of the radii, are treated as a local group for the purpose of constructing a FLAME basis. Two types of FLAME bases introduced in Section 4.3.2 are used, one of which is the local multipole-multicenter expansion and the other, purely numerical, is computed using FEM.

The overall accuracy of the analytical/numerical bases FLAME is dependent on two main factors. One source of the error is the finite-difference discretization by FLAME itself. This error primarily depends on the grid size of the global Cartesian mesh in FLAME. The other source of the error is the function of the accuracy of the local bases. For the analytical bases FLAME constructed by the multipole-multicenter expansion, this error is governed by the number of harmonics chosen. For the numerical bases FLAME determined by FE analysis, this error is governed by the FEM parameters, such as the FE mesh size, the order of finite elements, and the geometric shape of the elements.

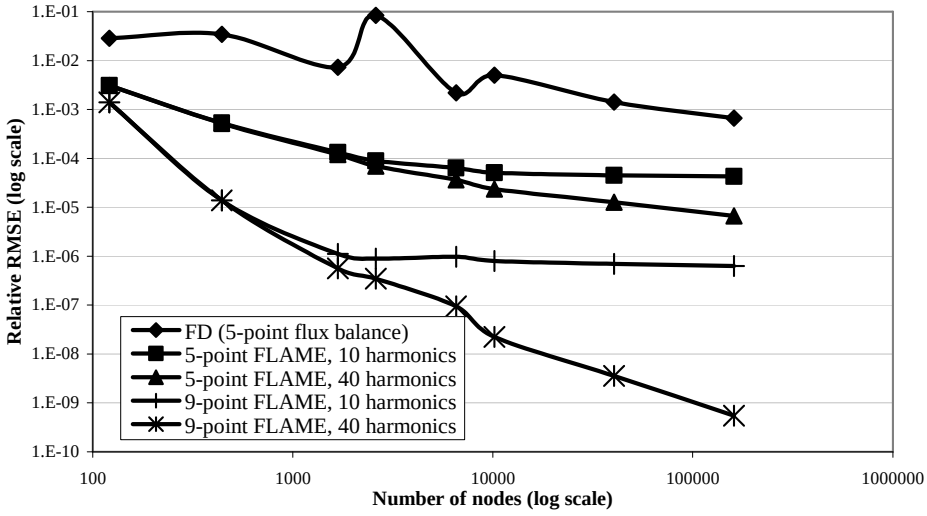

Figure 4.15: Numerical accuracy of analytical base FLAME for the electrostatic problem with poorly-separated particles.

Figure 4.15 shows the FLAME simulation result for the analytical bases constructed by the multipole-multicenter expansion. It can be easily seen that the accu-

racy of FLAME is much higher than that of the standard FD based on flux balance. When the grid size is greater than half of the smallest gap between the particles, FD provides a very crude approximation at best. The accuracy of standard FD begins to improve only after the grid size falls below half of the smallest gap.

For the five-point FLAME scheme with multipole-multicenter bases, provided that a sufficient number (in our example 40) of harmonics are used to generate the FLAME basis, the accuracy improves as the global mesh is refined. For a smaller number of harmonics (10), the FLAME accuracy increases only to some saturation level commensurate with the accuracy of the FLAME bases themselves. Similar observations are valid for the nine-point FLAME scheme (compare the error plots in Figure 4.15 for 10 and 40 harmonics in the construction of the basis).

The accuracy of the nine-point FLAME scheme is much greater than the accuracy of the five-point FLAME scheme. From our numerical data, the asymptotic behavior of the error in the potential is approximately $\mathcal{O}(n^{-0.8})$ for the five-point scheme and $\mathcal{O}(n^{-1.85})$ for the nine-point scheme.

For the numerical bases FLAME, the FEM is applied to calculate the local bases. Two FLAME basis functions computed by COSMOL Multiphysics are plotted in Figure 4.16. The functions correspond to two particles with a gap of one tenth of the radii.

Figure 4.17 shows the FLAME simulation result with the numerical bases. The number of FE degrees of freedom (d.o.f.) is a simulation parameter that affects the accuracy of the FE solution for the numerical FLAME bases. For the five-point

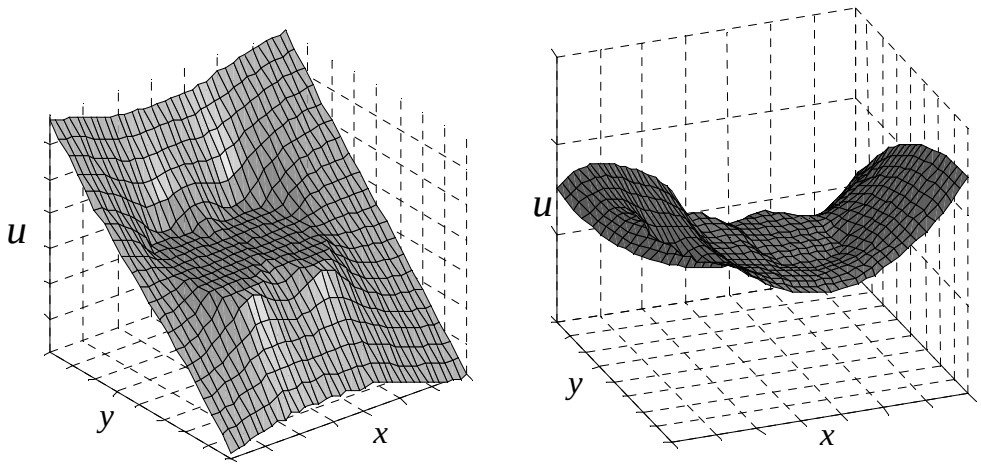

Figure 4.16: Examples of FLAME basis functions generated by FEM for a pair of nearby cylindrical particles, Left: basis function corresponding to the external applied field with potential $u_{\text{ext}} = y$, Right: $u_{\text{ext}} = x^2 - y^2$.

scheme, 5,401 d.o.f. and 59,371 d.o.f. yield similar accuracies, which shows that the numerical error in this case is primarily due to FLAME, rather than to the local FEM discretization.

The plot for the nine-point FLAME scheme with 59,371 d.o.f. has an anomaly. When the number of nodes becomes greater than 10,000, the accuracy deteriorates. This is caused by the limited accuracy of the FE solution for the FLAME bases. With limited accuracy, the null space of matrix N^T chas dimension greater than one in some patches. Fortunately, the dimension of the null space is not hard to monitor. If it becomes greater than one, the accuracy of the local FE solution needs to be increased (via h- or p-refinement).

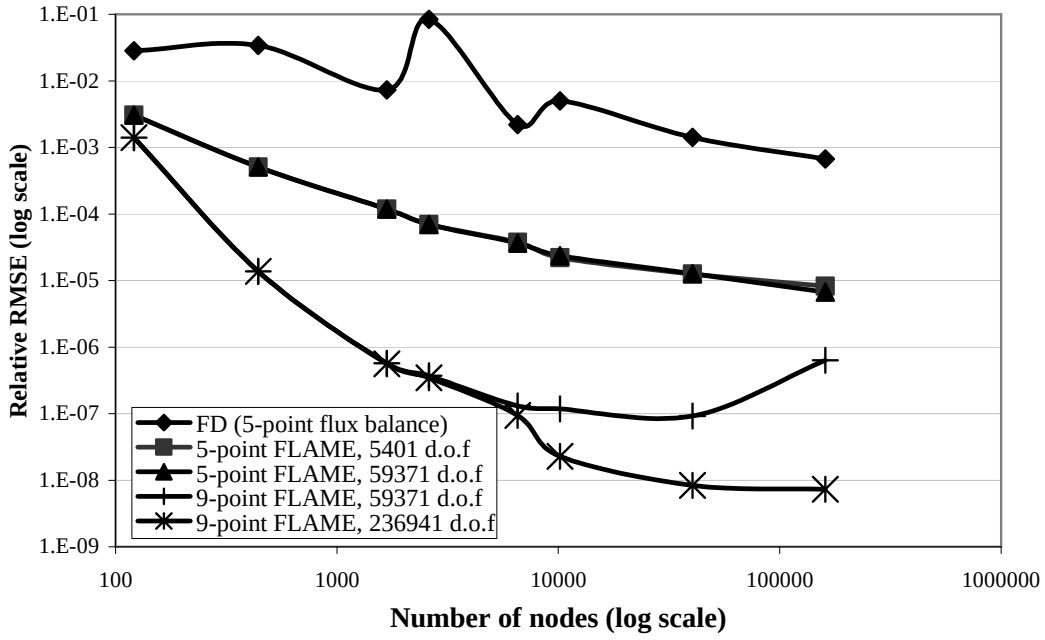

Figure 4.17: Numerical accuracy of numerical base FLAME (finite-element) for electrostatic problem with poorly-separated particles.

4.3.5 Numerical Result for Adaptive FLAME

As mentioned in Section 4.2, five-point and nine-point FLAME schemes are suitable for 2D models. After grid refinement, the schemes become distorted, as shown in Figure 4.18. Calculation shows that the five-point scheme on nonstandard stencils leads to much higher error compared to the nonstandard nine-point scheme. This error reduces or eliminates any advantage of adaptive grid refinement for the five-point FLAME scheme. On the other hand, the result in Section 4.2 shows that the nine-point scheme produces much greater accuracy than the five-point scheme. Therefore, our focus here is on the nine-point FLAME scheme for adaptive refinement.

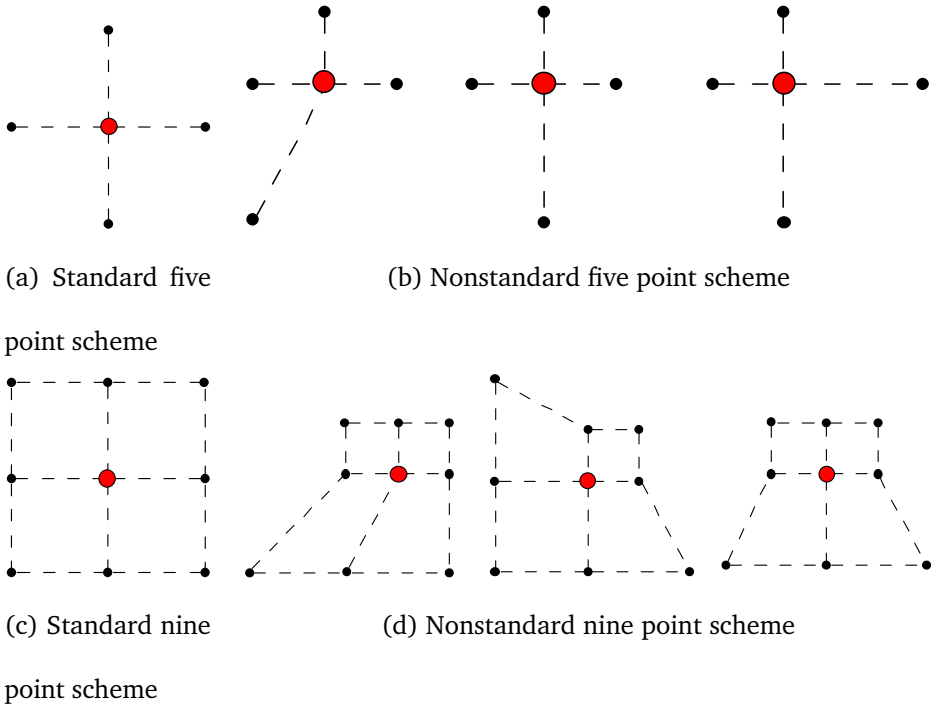

(a) Standard five point scheme

(b) Nonstandard five point scheme

(c) Standard nine point scheme

(d) Nonstandard nine point scheme

Figure 4.18: Examples of standard and nonstandard stencils (after [32], (c) 2008 IEEE).

The specific problem used to test adaptive FLAME involves the arrangement of four particles, as shown in Figure 4.19. The relative dielectric permittivities of the particles are $\epsilon_{\mathrm{p}} = 2, 4, 6, 8$. A few of the particles are deliberately placed in close proximity to one another, to make the problem nontrivial for standard FD analysis with a relatively coarse mesh. To eliminate the numerical error associated with the approximation of boundary conditions, the exact (theoretical) Dirichlet condition is applied on the exterior domain boundary.

Figure 4.20 shows a coarse Cartesian grid 11×11, as well as the grid obtained by gradual refinement. It can be seen that the mesh refinement is sensible

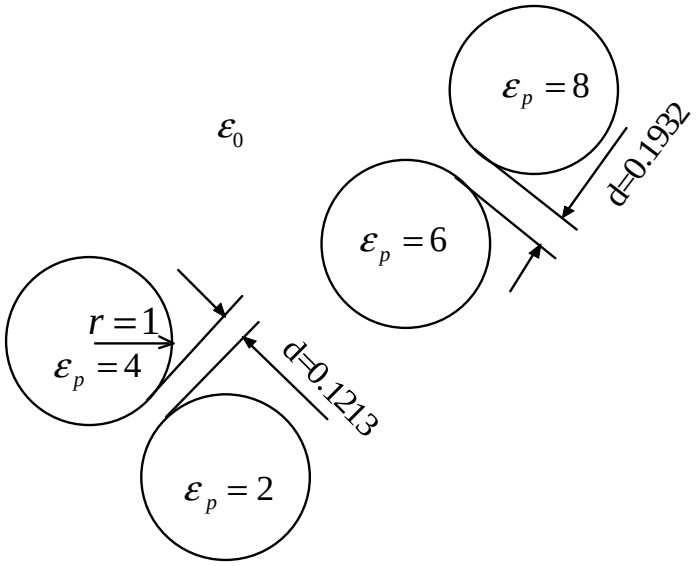

Figure 4.19: A 2D model with four particles for adaptive FLAME (after [32], (c) 2008 IEEE).

overall; the grid is refined in the "right" places, where two or more particles are in close proximity to one another. In such places, the behavior of the potential is more complicated than the potential's behavior in other regions.

The numerical accuracy of the potentials at 81 sample points is plotted in Figure 4.21 on the logarithmic scale as a function of the number of nodes. For comparison, accuracy plots for the standard five-point FD flux balance scheme, the regular FLAME scheme, and the first order and second order non-adaptive FEMs are also provided. Convergence of adaptive FLAME with gradual refinement is much faster than that of other methods. The asymptotic behavior of the accuracy is approximately $\mathcal{O}(n^{2.2})$.

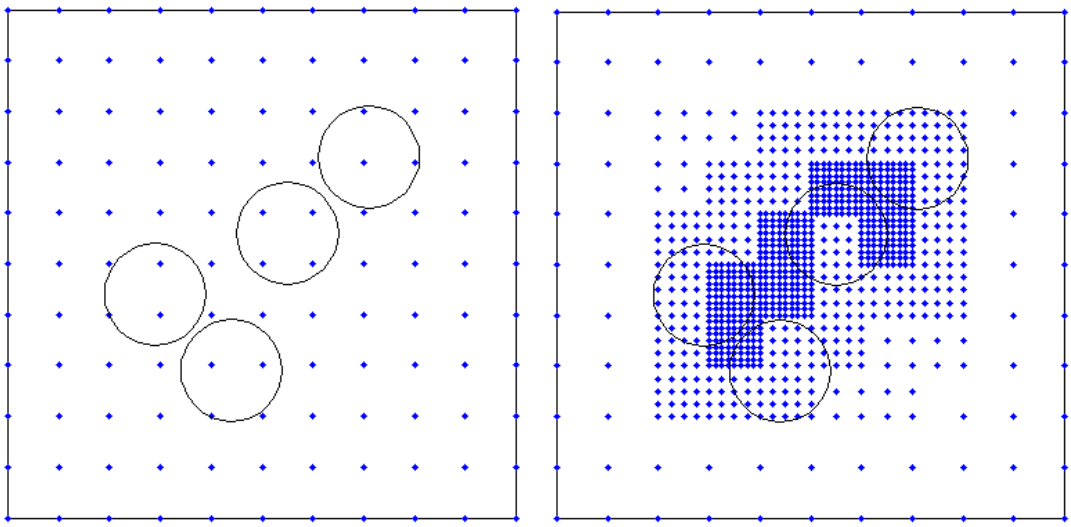

(a) Initial grid (b) Grid after refinement

Figure 4.20: Adaptive gradual grid refinement for 2D model of adaptive FLAME (after [32], (c) 2008 IEEE).

4.4 Case 3: Well-Separated Particles in 3D

All results presented in the preceding sections of this chapter have come from 2D electrostatic multiparticle problems. However, it is desirable to demonstrate the applications of FLAME in 3D. 3D problems are also divided into situations with well-separated and poorly-separated particles for discussion. This section focuses on the case with well-separated particles.

4.4.1 Quasi-Analytical solution for the 3D Multiparticle Problem

Similar to the 2D electrostatic model, quasi-analytical solution is used for accuracy evaluation in 3D problems. The multipole-multicenter expansion is used in the 3D

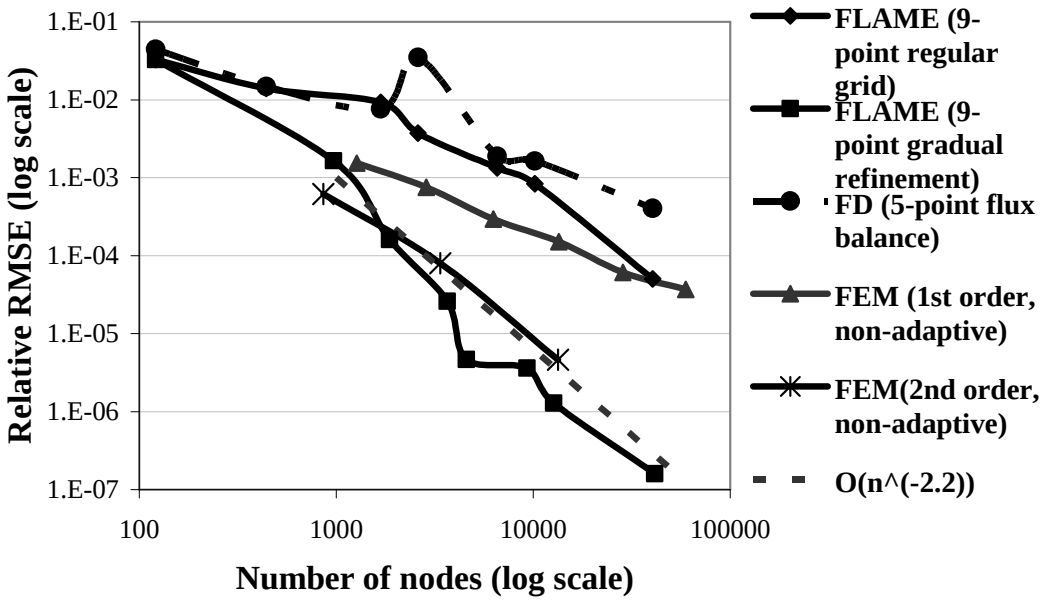

Figure 4.21: Numerical accuracy of adaptive FLAME for the poorly-separated electrostatic multiparticle problem (after [32], (c) 2008 IEEE).

model. However, this expansion is now based on the multipole algorithm instead of on the binomial expansion used in the 2D model. The multipole algorithm also relies on the transformations of the potential from one coordinate system to another one [14].

In the multipole-multicenter expansion, the global potential distribution is the summation of all the potentials that related to each particle, plus the external field applied for a 3D multiparticle system. The potential related to one particle's center can be expressed as

$$\phi = \begin{cases} \sum_{n=0}^{\infty} \sum_{m=-n}^{n} D_n^m \rho^n Y_n^m(\theta, \varphi) & Inside\ the\ particle \\ \sum_{n=0}^{\infty} \sum_{m=-n}^{n} O_n^m / \rho^{n+1} Y_n^m(\theta, \varphi) & Outside\ the\ particle \end{cases} \tag{4.9}$$

and

$$Y_n^m(\theta,\varphi) = \sqrt{\frac{n-|m|!}{n+|m|!}} \cdot P_n^{|m|}(cos\theta)\, e^{im\varphi} \tag{4.10}$$

where P_n^m is the associated Legendre function, and D_n^m and O_n^m are the coefficients that need to be determined from the boundary conditions. The potentials are referred to as the local expansion inside of the particle and the multipole expansion outside of the particle, as equation (4.9) shows.

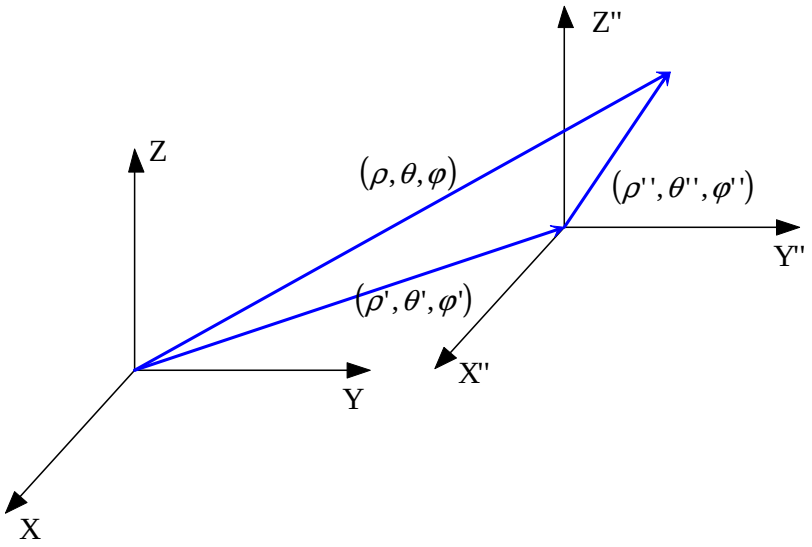

Figure 4.22: Coordinate translation for multipole-multicenter expansion.

Referring to Figure 4.22, there are two translations that are important for the multipole algorithm. One is the conversion from a multipole expansion to a local expansion. The other is the translation between local expansions. For the translation between multipole and local expansions, the multipole expansion with

coefficient O_n^m based on (X, Y, Z) can be converted to the local expansion based on (X'', Y'', Z'').

$$\phi \;=\; \sum_{j=0}^{\infty} \sum_{k=-j}^{j} L_j^k \left(\rho''\right)^j Y_j^k \left(\theta'', \varphi''\right) \tag{4.11}$$

where

$$L_j^k \;=\; \sum_{n=0}^{\infty} \sum_{m=-n}^{n} \frac{O_n^m \cdot i^{|k-m|-|k|-|m| \cdot A_n^m} \cdot A_j^k \cdot Y_{j+n}^{m-k}\left(\theta', \varphi'\right)}{\left(-1\right)^n A_{j+n}^{m-k} \cdot \left(\rho'\right)^{j+n+1}} \tag{4.12}$$

with A_n^m defined by the formula

$$A_n^m \;=\; \frac{\left(-1\right)^n}{\sqrt{(n-m)! \cdot (n+m)!}} \tag{4.13}$$

In regard to translation between local expansions, the local expansion with coefficient D_n^m based on (X, Y, Z) is translated to the other local expansion based on (X'', Y'', Z'').

$$\phi \;=\; \sum_{j=0}^{p} \sum_{k=-j}^{j} L_j^k \left(\rho''\right)^j Y_j^k \left(\theta'', \varphi''\right) \tag{4.14}$$

with

$$L_j^k \;=\; \sum_{n=0}^{p} \sum_{m=-n}^{n} \frac{D_n^m \cdot i^{|m|-|m-k|-|k| \cdot A_{n-j}^{m-k}} \cdot A_j^k \cdot Y_{n-j}^{m-k}\left(\theta', \varphi'\right) \cdot \left(\rho'\right)^{n-j}}{\left(-1\right)^{n+j} \cdot A_n^m} \tag{4.15}$$

By combining these two translations, the boundary condition and the applied external uniform field, the coefficients D_n^m and O_n^m can be calculated. Then, the potential distribution of the 3D multiparticle problem is the superposition of the potentials related to all the particles, plus the external potential applied. For all 3D electrostatic models in this chapter, the harmonics are truncated at the magnitude of 10^{-8} for the potential.

4.4.2 Accuracy of Nodal Potentials

A model with five particles in air is used as a 3D example with well-separated particles. All particles have the same radius, normalized to unity. The dielectric constants of all particles are 10. The distances between any two particles (center to center) are kept greater than 3.6 times the radii. A uniform external field is applied. To eliminate the influence of the boundary condition, the semi-analytical Dirichlet boundary condition is imposed on the outer boundary.

Figure 4.23 displays the nodal potential errors. For comparison, the results of standard seven-point FD based on flux balance, first order FEM and second order FEM are also provided. The errors are calculated in relative RMSE for the nodes excluding those at the outer boundary.

In this 3D electrostatic multiparticle model, the overall accuracy of the seven- and nineteen-point FLAMEs is much better than the other methods listed in Figure 4.23. The accuracy of the seven-point FLAME converges with the order $\mathcal{O}(n^{-0.7})$. The nineteen-point FLAME, which is in the order $\mathcal{O}(n^{-1.61})$, is much better than the seven-point FLAME. The relative RMSE is on the order of 10^{-8} when the number of grid nodes is 274625, when the corresponding grid size is $1/8$ of the particles' radii.

4.4.3 Potential Interpolation at Random Points

Using the theory introduced in Section 4.2.3, the potential at any point can be interpolated using the FLAME basis functions. To determine the accuracy, 1,000

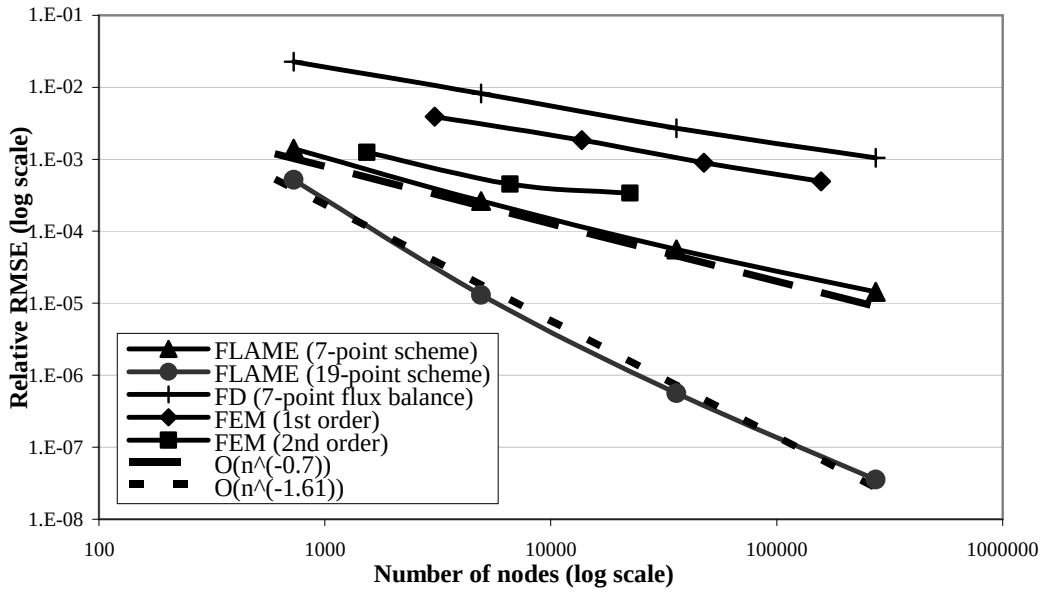

Figure 4.23: Numerical accuracy in mesh nodes potentials for problem with 3D well-separated particles.

points are randomly chosen in the domain. The overall accuracy is demonstrated by the relative RMSE.

Figure 4.24 shows the accuracy of potential interpolation for the seven-point and nineteen-point FLAME schemes. The accuracy of nodal potentials are also included for comparison. The nineteen-point FLAME shows the best accuracy compared with the seven-point FLAME, first and second order FEMs. It is of course not surprising that the accuracy of the interpolated potential is a little worse than that of the nodal potentials.

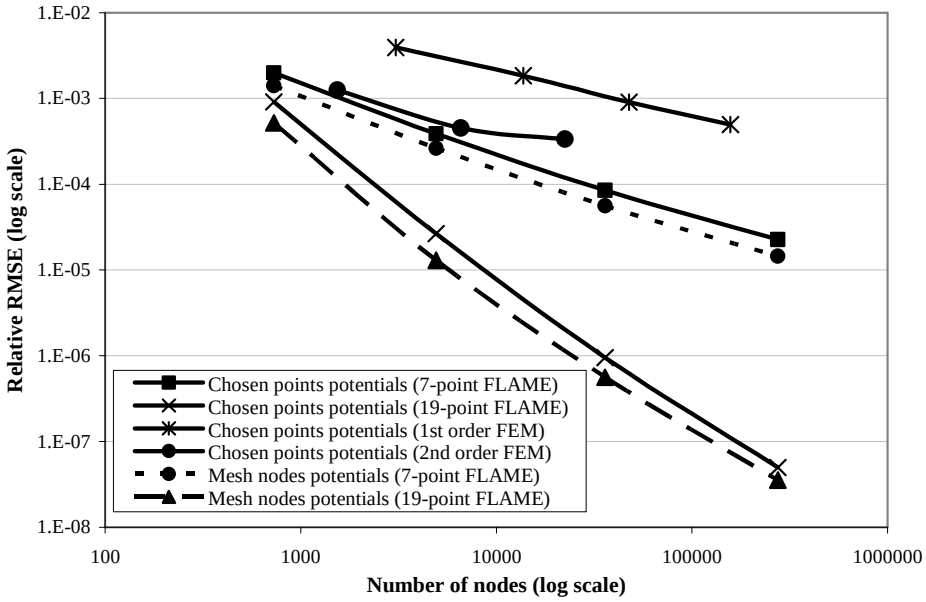

Figure 4.24: Numerical accuracy in potential interpolation for problem with 3D well-separated particles.

4.5 Case 4: Poorly-Separated Particles in 3D

Now let us consider 3D problems with poorly-separated particles. The example includes four particles with the same normalized radii $r_{\mathrm{p}} = 1$ and the dielectric constant $\epsilon_{\mathrm{p}} = 2$. The particles are immersed in a medium (e.g. a solvent) with $\epsilon_{\mathrm{s}} = 80$. There are two particles that are in close proximity to one another, with the gap of $\sim$0.1459 between them. A uniform external field is applied. For comparison and verification, the analytical solution is obtained via the multipole-multicenter expansion (truncated at the terms with the magnitude of 10^{-8}). To eliminate the effects of domain truncation, the semi-analytical Dirichlet condition is imposed on the boundary.

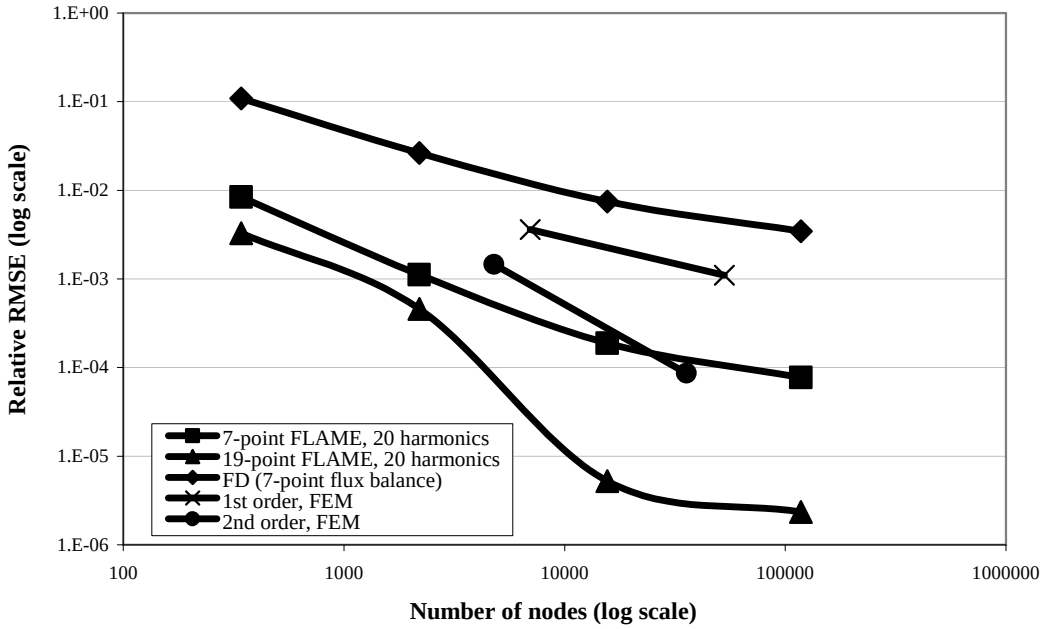

Figure 4.25: Accuracy in potential of grid nodes for electrostatic problem with the 3D poorly-separated particles based on multipole-multicenter expansion.

As Figure 4.25 shows, the nineteen-point scheme yields much greater accuracy than the seven-point scheme when the FLAME bases are computed with sufficient accuracy. The asymptotic convergence rate for the potentials is $\sim O(n^{1.5})$ for the seven-point scheme and $\sim O(n^{3.5})$ for the nineteen-point scheme.

4.6 Conclusion

FLAME is a new finite-difference calculus that incorporates accurate local approximations into the difference scheme. For particles that are well-separated (gaps greater than the mesh size), regular FLAME provides greater accuracy compared with the standard FD based flux balance, first and second order FEMs.

The special situation, where particles are in close proximity to one another, is more difficult. Two approaches, analytical/numerical base FLAME and adaptive FLAME, are proposed and tested with electrostatic multiparticle models. The analytical/numerical base FLAME treats the area that has poorly-separated particles as a local problem, and two strategies of computing the basis functions are suggested. The first strategy employs a local multipole-multicenter expansion. The second strategy is purely numerical, and the FEM is used to generate FLAME bases. In either case, solving local problems requires much less computation than solving the global problem, since no complicated meshes and no large systems of equations are involved.

Adaptive FLAME borrows some general ideas from adaptive FEM but, being a finite-difference method, is substantially different. The solution is approximated on the individual subdomains (patches) covering the global computational domain. The discrepancy between the patch-wise numerical solutions in the areas of overlap serves as an *a posteriori* error indicator. Electrostatic problems with multiple dielectric particles provide meaningful test cases for grid refinement. The error indicator correctly identifies the regions around particle clusters and small air gaps as target areas for grid refinement. As a result, convergence of the adaptive algorithm as a function of the number of nodes is much faster than that of global refinement.

Numerical examples show that the accuracy of FLAME is much higher than that of the standard FD (flux balance), even that of FEM. This paves the way for solving problems with a large number of particles on relatively coarse grids, and

with mesh sizes comparable to or even greater than the radii of the particles, and the separation distances between them.

CHAPTER V

WAVE SCATTERING FROM CYLINDRICAL DIELECTRIC PARTICLE MATERIALS

This chapter introduces the applications of FLAME to structures composed of cylindrical dielectric particles. Such strucutres have many promising applications in photonics; of particular interest are photonic crystals [34]. The construction of FLAME schemes is discussed, together with analytical calculations for wave scattering problems. Several examples are demonstrated for FLAME simulation in both situations with well-separated and poorly-separated particles.

5.1 Introduction

Electromagnetic wave scattering is a general physical phenomenon that is governed by the Maxwell equations. The study of electromagnetic wave scattering has many applications, such as in radar systems, astronomy, optics, and solid state physics [33]. Figure 5.1 shows a scattering problem of waveguide composed of cylindrical particles, where the field varies in the XY-plane and there is no variation in the Z direction. The problem can then be formulated in 2D as the scalar time-harmonic

wave equations can be used as the governing euqations.

$$\left[\frac{\partial}{\partial x}\left(\frac{1}{\mu}\frac{\partial}{\partial x}\right)+\frac{\partial}{\partial y}\left(\frac{1}{\mu}\frac{\partial}{\partial y}\right)+\omega^2\epsilon\right]E_z \;=\; j\omega J_z \tag{5.1}$$

$$\left[\frac{\partial}{\partial x}\left(\frac{1}{\epsilon}\frac{\partial}{\partial x}\right)+\frac{\partial}{\partial y}\left(\frac{1}{\epsilon}\frac{\partial}{\partial y}\right)+\omega^2\mu\right]H_z \;=\; -\frac{\partial}{\partial x}\left(\frac{1}{\epsilon}J_y\right)+\frac{\partial}{\partial y}\left(\frac{1}{\epsilon}J_x\right) \tag{5.2}$$

There are two basic modes in a homogeneously filled waveguide: transverse electric (TE) mode and transverse magnetic (TM) mode. TE mode has no electric field component in the propagation direction, and TM mode has no magentic field component in that direction instead. The general wave problems can be treated as a linear combination of these two modes.

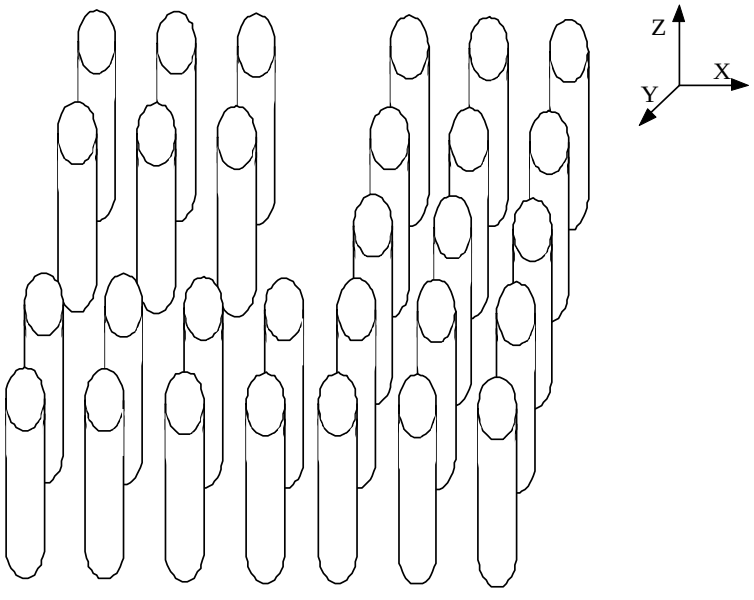

Figure 5.1: Wave propagation and scattering from cylindrical particles can be treated as a 2D problem in the xy-plane.

Numerical calculation plays an important role in the analysis and design. FDTD is a very useful and versatile method for wave scattering problems in general and for optical devices in particular [11, 34]. FEM has also been widely used, especially in recent years due to substantial improvements in commercial FE software [35]. As mentioned in Chapter 1, both methods have their advantages and disadvantages for this type of problem. For problems with a large number of particles, FDTD and FEM need extremely fine meshes to achieve reasonable accuracy, which makes the computation difficult. FLAME has been proved to be successful in solving the electrostatic multiparticle problems in Chapter 4. In this chapter, this method is applied to wave scattering.

5.2 FLAME for Wave Scattering from Cylindrical Particles

According to (5.1) and (5.2), the scalar wave equations of TM and TE modes are derived assuming no source current exists.

$$\nabla \cdot \mu^{-1} \nabla E_z \; + \; \omega^2 \epsilon E_z \; = \; 0 \;\; TM \; mode \tag{5.3}$$

$$\nabla \cdot \epsilon^{-1} \nabla H_z \; + \; \omega^2 \mu H_z \; = \; 0 \;\; TE \; mode \tag{5.4}$$

The FLAME basis functions, which satisfy the scalar wave equations ((5.3) for TM mode, (5.4) for TE mode), are chosen as cylindrical harmonics in the vicinity

of each particle based on cylindrical coordinate.

$$\psi_{\alpha}^{(i)} = \begin{cases} a_n J_n(k_{cyl} r) exp(in\theta), & r \leq r_0 \\ [b_n H_n^{(2)}(k_{out} r) + H_n^{(1)}(k_{out} r)] exp(in\theta), & r > r_0 \end{cases} \tag{5.5}$$

where J_n is the Bessel function, $H_n^{(1)}$ and $H_n^{(2)}$ are the Hankel functions of the first and second kinds, respectively, a_n and b_n are coefficients to be determined via the boundary conditions.

For the five-point FLAME scheme, four basis functions are required. They can be chosen as one monopole harmonic ($n = 0$), two dipole harmonics ($n = \pm 1$), and one quadrupole harmonic ($n = 2$). For the nine-point FLAME scheme, harmonics with $n = 0, n = \pm 1, n = \pm 2, n = \pm 3, n = 4$ are retained for eight basis functions. Using these basis functions, the schemes for all patches can be constructed.

5.3 Quasi-Analytical Calculation for Wave Scattering from Cylindrical Particles

The quasi-analytical result is used to evaluate the accuracy of FLAME in cylindrical wave scattering problems. Similar to the 2D and 3D electrostatic problems, such result is obtained using multipole-multicenter expansion. According to multipole-multicenter expansion for wave scattering problems, the global field distribution is the summation of all the fields that related to each particle, plus the external field applied. Assuming one cylinder in the wave scattering model is centered at the origin, the electric field (TM mode) or magnetic field (TE mode) related to this

cylinder can be expressed as

$$u = \begin{cases} \sum_{m=-\infty}^{\infty} G_n r^n J_n(\kappa_r r) e^{in\theta} & Inside\ particle \\ \sum_{m=-\infty}^{\infty} F_n r^n H_n^{(p)}(\kappa_r r) e^{in\theta} & Outside\ particle \end{cases} \tag{5.6}$$

Here, u is the electric field for the TM mode or the magnetic field for the TE mode, $J_n(x)$ is the Bessel function, $H_n^{(p)}(x)$ represents the Hankel function where p is its order, G_n and F_n are constant coefficients to be determined.

The coefficients G_n and F_n can be calculated based on the addition theorem [36] by matching the boundary conditions between particles and the surrounding medium. The addition theorem expresses wave functions in one coordinate system as functions of another coordinate system (Figure 5.2). For the Hankel function, this translation is

$$H_m^{(p)}(k_r|r-r'|)e^{im\theta''} = \begin{cases} \sum_{n=-\infty}^{\infty} J_{n-m}(k_r r') H_n^{(p)}(k_r r) e^{in\theta - i(n-m)\theta'}, r > r' \\ \sum_{n=-\infty}^{\infty} H_{n-m}^{(p)}(k_r r o') J_n(k_r r) e^{in\theta - i(n-m)\theta'}, r < r' \end{cases} \tag{5.7}$$

For the Bessel function, the translation is

$$J_m(k_r|r-r'|)e^{im\theta''} = \sum_{n=-\infty}^{\infty} J_{n-m}(k_r r') J_n(k_r r) e^{im\theta - i(n-m)\theta'} \tag{5.8}$$

For two contiguous media, the tangential and normal components of E, D, B, and H must satisfy equation (5.9), where $\hat{n}$ is the normal direction:

$$\begin{cases} \hat{n} \times (E_1 - E_2) = 0 \\ \hat{n} \cdot (D_1 - D_2) = \rho_s \\ \hat{n} \times (H_1 - H_2) = J_s \\ \hat{n} \cdot (B_1 - B_2) = 0 \end{cases} \tag{5.9}$$

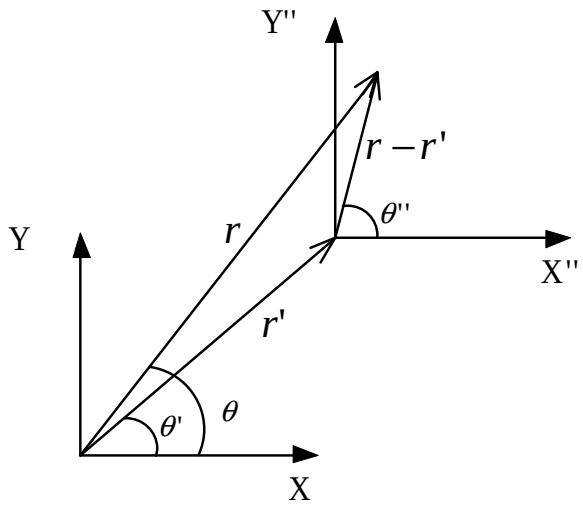

Figure 5.2: Translation between two cylindrical coordinate systems.

Once the coefficients G_n and F_n for all cylinders are calculated, the field distribution can be determined. In practice, the result converges rapidly as the number of harmonics n in (5.6) increases. For all the cylindrical wave scattering problems in this chapter, the harmonics are truncated at the magnitude of 10^{-9} to obtain a quasi-exact solution for verification purposes.

5.4 Case 1: Wave Scattering from the Well-Separated Cylindrical Particles

As in the case of electrostatic multiparticle problems, wave scattering problems are separated into two categories for discussion: well-separated and poorly-separated particles. Figure 5.3 shows a wave scattering example with well-separated particles, which includes six cylinders with equal radii $r_p = 40$ nm. The relative permittivities of all nonmagnetic cylinders in the air are shown in the figure. The incident wave

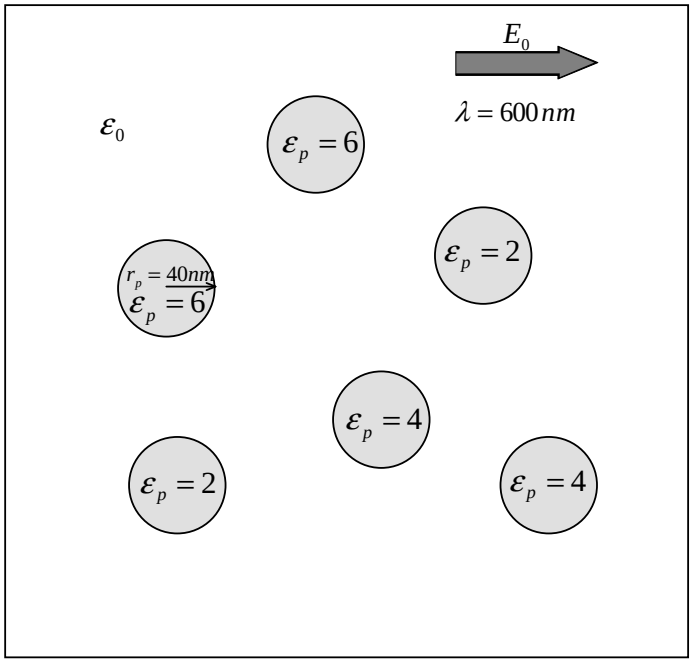

Figure 5.3: 2D geometric setup for wave scattering from well-separated cylindrical particles.

with $\lambda = 600$ nm propagates in the x-direction. To eliminate any numerical error associated with the domain boundary, the quasi-exact Dirichlet field is imposed on this boundary.

Figures 5.4 and 5.5 show the results for the wave scattering problems with well-separated cylindrical particles for the TM and TE modes. For both modes, the five-point FLAME scheme yields greater accuracy than first order FEM. A similar conclusion can be drawn for the nine-point FLAME scheme as compared with second order FEM. For TM mode, the accuracy of the nine-point FLAME scheme is increased quickly as the number of nodes increases, and then maintains when the

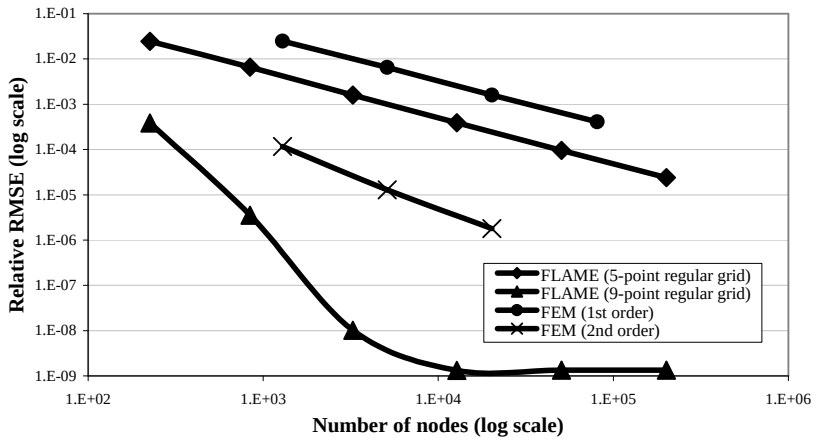

Figure 5.4: Relative accuracy vs. the number of nodes, well-separated particles, wave scattering, TM mode.

nodes goes to certain number due to the accuracy limitation of analytical calculation. Overall, FLAME yields greater accuracy than FEM for this problem.

5.5 Case 2: Wave Scattering from the Poorly-Separated Cylindrical Particles

The wave scattering example with poorly-separated particles includes four cylinders with equal radii $r_{\mathrm{p}} = 40$ nm and relative permittivities ϵ_{p} = 2, 4, 6, 8 (Figure 5.6). All materials are nonmagnetic. The first three cylinders are placed close to each another and relatively far from the fourth one. The incident wave with $\lambda = 600$ nm propagates in the x-direction. The same adaptive refining strategy introduced in Section 4.3.3 of Chapter 4 is used in this problem.

A Cartesian 15×15 grid, with and without refinement, is shown in Figure 5.7. It is clear that the entire area around the three-cylinder cluster has been

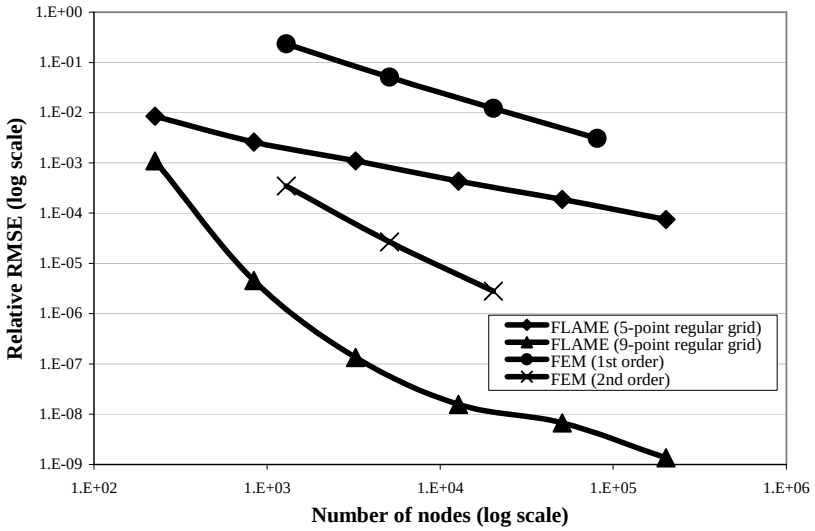

Figure 5.5: Relative accuracy vs. the number of nodes, well-separated particles, wave scattering, TE mode.

refined. In this particular example, the refinement pattern happens to coincide for the TM and TE modes, but this is not necessarily the case in general.

Figures 5.8 and 5.9 demonstrate the accuracy of FLAME for the TM and TE modes in this sample with poorly-separated particles. For both modes, the overall accuracy of adaptive gradual grid refinement is greater than those of other methods, with the asymptotic convergence rate for the field in the range of $\mathcal{O}(n^{-1.6})$–$\mathcal{O}(n^{-1.8})$. It is interesting to note the anomalously rapid convergence of FLAME when the number of nodes n is around 1000 . With n in the order of a few thousand, the grid sizes become smaller than the gaps between the particles. As a result, nodes of the same patch can no longer belong to different particles, which bodes well for convergence.

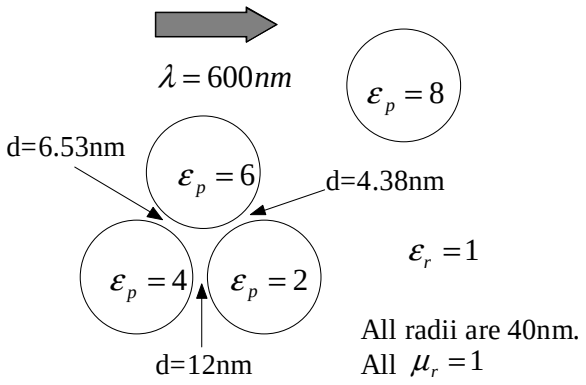

Figure 5.6: 2D geometric setup for the wave scattering problem with poorly-separated cylindrical particles (after [32], (c) 2008 IEEE).

5.6 Conclusion

The emphasis of this chapter is on the application of FLAME to wave scattering by cylinders. The results of FLAME are compared with those of FEM, and demonstrate higher accuracy. For the situation with poorly-separated particles, the proposed error indicator (refer to Chapter 4) is used to identify correctly the areas that have small air gaps for grid refinement. The convergence of the adaptive algorithm is much faster than that of the global refinement.

This chapter deals only with scattering from infinite cylinrical particles, which can be formulated as a 2D problem. Applications of FLAME to 3D electromagnetic problems may also be expected to yield greater accuracy but need substantial further development and investigation [24].

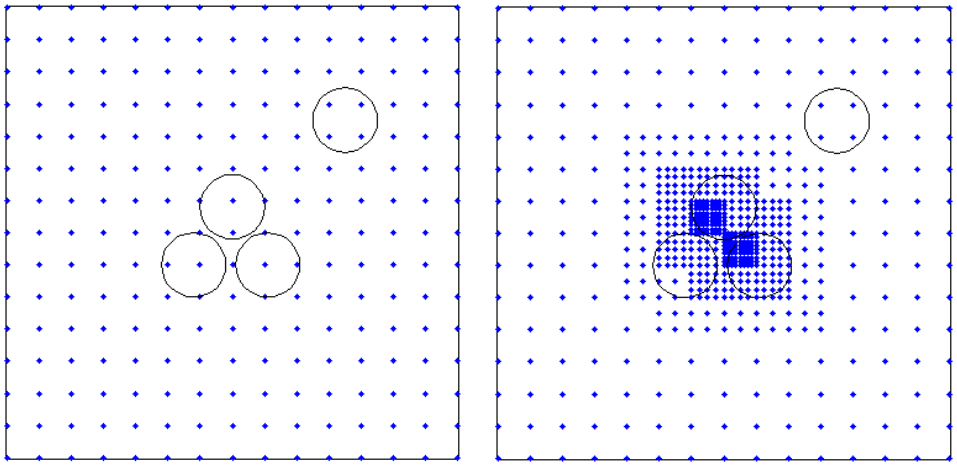

(a) Initial grid (b) Grid after refinement

Figure 5.7: Adaptive gradual grid refinement for wave scattering (after [32], (c) 2008 IEEE).

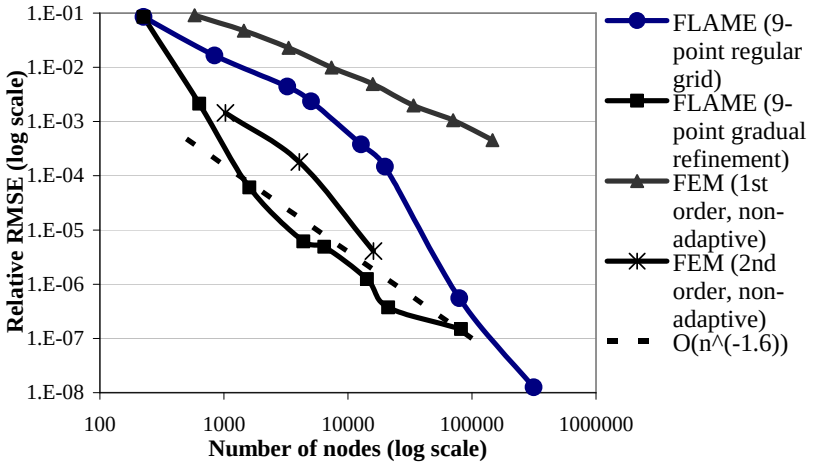

Figure 5.8: Relative error vs. the number of nodes, poorly-separated particles, wave scattering, TM mode (after [32], (c) 2008 IEEE).

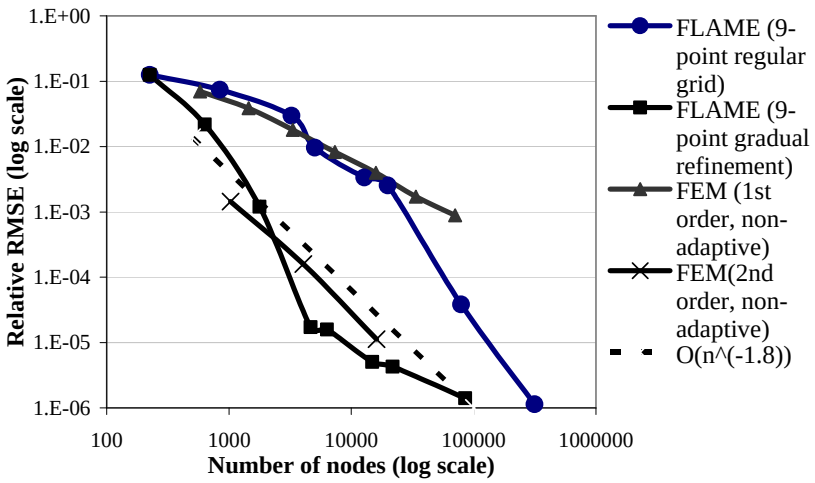

Figure 5.9: Relative error vs. the number of nodes, poorly-separated particles, wave scattering, TE mode (after [32], (c) 2008 IEEE).

CHAPTER VI

ELECTROSTATIC INTERACTIONS FOR THE PARTICLES IN ELECTROLYTES

This chapter applies FLAME to electrostatic interactions for macromolecules (e.g., protein molecules) in solvents. The background and formation of the problem are presented first. Then, the construction of FLAME schemes and the analytical calculation of the field are introduced. Finally, numerical results demonstrate the efficiency of this model.

6.1 Electrostatic Interactions for Macromolecules in Solvents

Proteins are large organic compounds made of amino acids arranged in a linear chain. The patterns of molecular surface groups and absorbed counter-ions around the surface strongly affect the electrostatic interaction in proteins [37, 38]. The electrostatic interactions depend strongly on the structure and configuration of the molecule [39]. The electrostatic interactions play a critical role in defining the structure, stability, and chemical properties of proteins [40].

Experiments and computer simulations have been used extensively to probe the electrostatic and dielectric properties of proteins. Research by Kumar et al. [41] shows that electrostatic interactions are sensitive to protein flexibility, since they

depend upon the location and orientation of the interacting charges as well as their neighborhoods. For this type of problem, the traditional numerical method, such as FEM and FD method, usually requires extremely complex mesh generation to maintain certain accuracy.

6.2 Model of Macroscopic Continuum Electrostatics

The model of macroscopic continuum electrostatics is one of the most widely used to evaluate electrostatic interactions in the protein-solvent systems (e.g. [42–45]). In this model, the protein medium is considered as a region with low dielectric constant (around 2-4 [38]). It is immersed in an aqueous solvent. The solvent has a relatively high dielectric constant ($\sim$80). Such a model provides reasonable accuracy in determining the short-distance interactions within the interior of proteins. In the long-distance interactions, however, the result is not good enough in estimating these interactions accurately within any region of a protein due to the existance of point charges [46].

The concept of non-local electrostatics and phenomenological theory of the polar solvent is used by Rubinstein et al. [46]. The electrostatic problem with the standard boundary conditions is solved for a planar interface in terms of the spatial Fourier transforms $\epsilon_1(k)$. The $\epsilon_1(k)$, which is the dielectric function, characterizes the bulk properties of the two condensed media in contact. As discussed, the protein-like medium is considered as a uniform dielectric with a low dielectric constant: $\epsilon_1(k) = \epsilon_1 = 4$. The orientation Debye polarization in an aqueous sol-

vent (determined by the hindered rotations of the water dipoles due to hydrogen-bonding chains in bulk water) is considered by the simplest approximation of the dielectric function:

$$\epsilon_2(k) \;=\; \epsilon_* \;+\; \frac{\epsilon_s - \epsilon_*}{1 + (Lk)^2 \epsilon_s/\epsilon_*} \tag{6.1}$$

where $\epsilon_* = 6$ and $\epsilon_s = 78.3$ are short- and long-wavelength dielectric constants of the solvent at room temperature. L, the correlation length of water dipoles, is proportional to the characteristic length of the hydrogen-bonding network of water molecules (~ 5 Å). For short-range pair-wise electrostatic interactions (inter-charge distances $< L$) in protein in close proximity ($< L$) to the interface, the value of the effective dielectric function is found to be very low.

According to research of Rubinstein et al. [46], this suggests that the low value of the effective dielectric function in the protein in close proximity to the interface is a result of a low-dielectric interfacial solvent layer from the physical standpoint. The thickness of this layer is comparable with the correlation length L. The effective dielectric permittivity of the layer in close proximity to the dielectric boundary is determined by the short-wavelength dielectric constant of the bulk phase of the solvent ($\epsilon_* = 6$), which is much smaller than the bulk value ϵ_s. This model is consistent with the experimental data on partially structured boundary water layer ('dynamically ordered water') on the surface of the protein native structure [47]. Overall, the data obtained by Rubinstein et al. [46] suggests that the low-dielectric solvent layer on the protein surface is a critical factor that determines the electrostatic fields in the vicinity of the protein-solvent interface. The

significant decrease in the screening of the field at the protein-solvent interface has been underestimated in traditional electrostatic models.

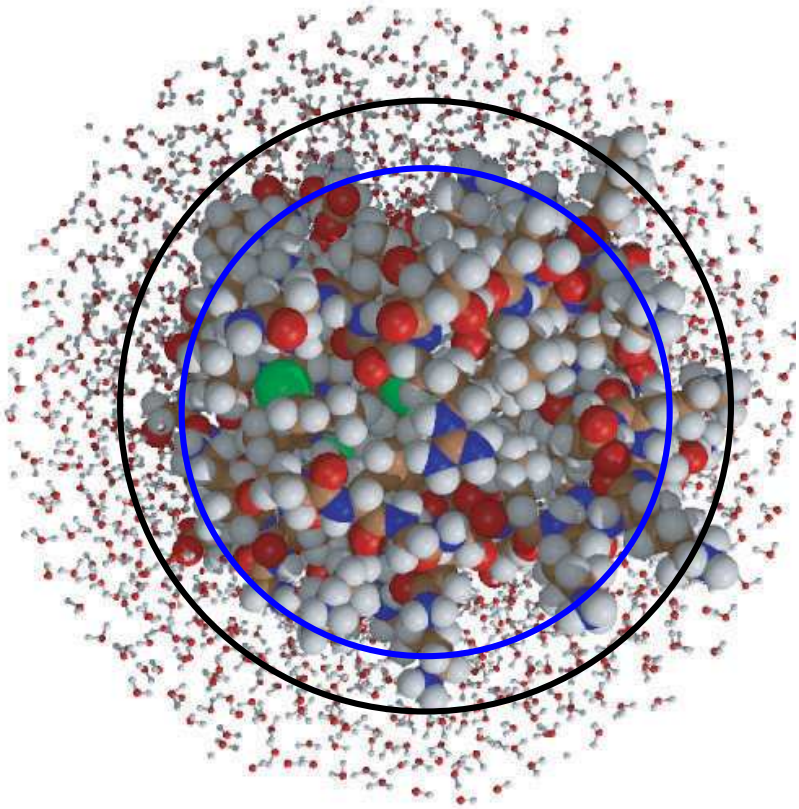

Figure 6.1: Schematic diagram of one protein sample.

Figure 6.1 shows a protein sample. The protein core is tightly packed, surrounded by the solvent. Accordingly, a practical model with three dielectric layers is proposed as Figure 6.2. The protein molecule is simplified as a spherical particle with radius 30 Å, which is the inner layer. The intermediate layer is the solvent ($\sim$6 Å) adjacent to the protein molecule; the dielectric constant of this layer is determined by the short-wavelength dielectric constant of the sovlent $\varepsilon_* = 6$.

Finally, the outer layer represents the bulk phase of the solvent, with the relative dielectric constant of $\sim$80.

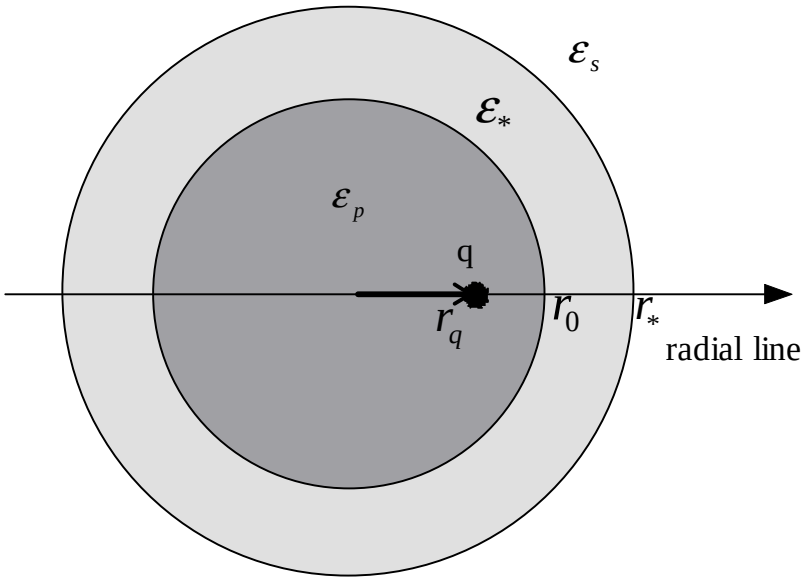

Figure 6.2: Two dimensional representation of model with three layers (after [23], (c) 2008 IEEE).

For the inner and intermediate layers, the potential u is governed by the electrostatic equation

$$\nabla \cdot \varepsilon \nabla u \; = \; \sum_{\alpha} q_\alpha \delta(\mathbf{r} - \mathbf{r}_\alpha) \tag{6.2}$$

where q_α are the point charges corresponding to the protein atoms at locations $\mathbf{r}_\alpha$ inside the protein.

The solvent plays a significant role in determining the electrostatic potential energy of the protein [48]. For the outer solvent layer, under the assumption of

mean-field theory, the Poisson-Boltzmann equation (PBE) is used to determine the electrostatic potential.

The main physical assumption of the PBE is that each mobile charge is in the mean field of all other charges, and has the Boltzmann probability of a given energy level [49]. The charge density ρ due to the microions in the solvent is

$$\rho \;=\; \sum_{\alpha} n_{\alpha} z_{\alpha} q \tag{6.3}$$

where n_α is the number of charges per unit volume (refer to as number density), $z_\alpha = \pm 1$ which depends on the polarity of charge, q is the unit value of ion (1.6×10^{-19} Coulomb). Let

$$q_{\alpha} \;=\; z_{\alpha} q \tag{6.4}$$

The number density of ions is given by the Boltzmann equation

$$n_i \;=\; n_i^0 exp\left(-\frac{q_\alpha \phi}{k_B T}\right) \tag{6.5}$$

where k_B is the Boltzmann constant, and T is the absolute temperature. Together with the Poisson equation, (6.6) can be obtained

$$-\nabla \cdot \varepsilon \nabla \phi \;=\; \sum_{\alpha} n_{\alpha}^0 q_{\alpha} \exp\left(-\frac{q_\alpha \phi}{k_B T}\right) \tag{6.6}$$

The nonlinearity of the PBE due to the exponential dependence of the mobile ion concentrations on the potential complicates the numerical solution, especially for complex geometries and charge distributions [13].

When the electrostatic energy of ions is much lower than their thermal energy, the term $q_\alpha u/(k_B T) \ll 1$. Therefore, the PBE can be linearized by retaining

the first two terms of the Taylor series of the exponential part [50, 51]. Due to the electroneutrality, $\sum_\alpha n_\alpha q_\alpha = 0$, the linearized PBE becomes

$$\nabla^2 u \; - \; \kappa^2 u \; = \; 0, \qquad \kappa^2 = \sum_\alpha \frac{n_\alpha q_\alpha^2}{k_B T \varepsilon_s} \tag{6.7}$$

This equation is also known as the Debye-H$\ddot{u}$ckel model. The potential will typically exhibit an exponential decay with the rate controlled by κ. The inverse of κ is the Debye-H$\ddot{u}$ckel length.

In the three-layer protein-solvent model, the solvent is modeled as a continuum function that is approximated by PBE, while the protein is modeled using discrete atoms. It makes traditional numerical methods difficult to use for this type of problem. FLAME incorporates accurate local approximations of the solution into the difference scheme and often yields greater accuracy on simple Cartesian grids than classical FD and even than FEM with its complex meshes. This protein-solvent model is treated as an initial step for testing and validating of the applications of FLAME for the simulation of macroscopic continuum electrostatics.

6.3 FLAME Applied in the Protein-Solvent Model

For the protein-solvent model, a set of basis functions satisfying the Poisson equation and PBE are needed to generate a FLAME scheme. The basis functions can be constructed using spherical harmonics:

$$\psi_{mn} = \begin{cases} P_n^m(\cos\theta)\exp(\mathrm{i}m\phi)r^n \quad \text{Inner layer} \\ P_n^m(\cos\theta)\exp(\mathrm{i}m\phi)(c_{mn}r^n + d_{mn}r^{-n-1}) \quad \text{Intermediate layer} \\ P_n^m(\cos\theta)\exp(\mathrm{i}m\phi)(f_{mn}j_n(\mathrm{i}kr) + g_{mn}n_n(\mathrm{i}kr)) \quad \text{Outer layer} \end{cases} \tag{6.8}$$

Here $j_n(z) = (\pi/(2z))^{1/2}J_{n+1/2}(z)$ and $n_n(z) = (\pi/(2z))^{1/2}Y_{n+1/2}(z)$ are the spherical Bessel functions of the first and second kinds, respectively. They are expressible in terms of the hyperbolic sine and cosine functions and are therefore fairly easy to work with. The coefficients c_{mn}, d_{mn}, f_{mn}, g_{mn} are determined from the interface boundary conditions [15].

Figure 6.2 shows a prototype protein-solvent problem with point charge. It originates from the two-layer protein-solvent problem developed by Gilson et al. [43]. Due to the existance of point charge, it makes governing equation inhomogeneous (i.e. the right hand side is nonzero). The FLAME scheme is then constructed by splitting the solution as equation (3.17) of Chapter 3. For this model, seven- and nineteen-point FLAME schemes are considered.

In the traditional FD method, the point charge is usually projected onto the nearest eight grid points [52]. This charge discretization introduces additional errors, especially when the charge is located close to the protein boundary [53]. For FLAME scheme construction based on potential splitting, the electrostatic potentials at charge site are accurately determined using the exact analytic forms according to Coulomb's law. Using the potential splitting and Coulomb's law, there is *no*

numerical error due to the potential of point charges, as this potential is represented analytically and exactly.

6.4 Quasi-Analytical Calculation for the Particle in an Electrolyte

In the model shows in Figure 6.2, the point charge inside the molecule is the source of the field. The location of this charge may vary. Assuming a point charge q is laid in the place with radius r_q, the potential in the molecular layer is calculated by the equation below.

$$\phi \;=\; \frac{q}{4\pi\varepsilon_p \left|r - r_q\right|} \tag{6.9}$$

The outer layer is governed by the linear PBE. The analytical solution there can be written as a linear combination of spherical Bessel functions of first and second kinds. So, the potential of the three layers can be separately represented as

$$\phi \;=\; \begin{cases} \frac{q}{4\pi\varepsilon_p|r-r_q|} + \sum_{n=0}^{\infty} B_n r^n P_n\left(cos\theta\right) & Inner\ layer \\ \sum_{n=0}^{\infty}\left[C_n j_n\left(ik_{mid}r\right) + D_n n_n\left(ik_{mid}r\right)\right] P_n\left(cos\theta\right) & Intermediate\ layer \\ \sum_{n=0}^{\infty} G_n F\left[j_n\left(ik_{out}r\right),\ n_n\left(ik_{out}r\right)\right] P_n\left(cos\theta\right) & Outer\ layer \end{cases} \tag{6.10}$$

where $P_l(x) = \frac{1}{2^l l!}\frac{d^l}{dx^l}(x^2-1)^l$, $j_r(z)$ is the Legendre polynomial, $j_r(z)$ and $n_r(z)$ are the spherical Bessel functions of first and second kinds, respectively, and $F[j_n\left(ik_{out}r\right)$, $n_n\left(ik_{out}r\right)]$=$i^{n+2}j_n\left(ik_{out}r\right) + i^{n+3}n_n\left(ik_{out}r\right)$.

According to the translation theorem for the multipole expansion [14], equation (6.9) can be translated to

$$\frac{q}{4\pi\varepsilon_p\left|r-r_q\right|} \;=\; \sum_{n=0}^{\infty} A_n r^{-n-1} P_n\left(cos\theta\right) \tag{6.11}$$

By matching the boundary conditions of layers' interfaces, the coefficients A_n, B_n, C_n, D_n and G_n can be determined and the electrostatic potential distribution in the whole domain can be found. The accuracy of the analytical result depends on the number of harmonics and the location of the point charge. In this chapter, the analytical result is truncated at the terms with the magnitude of potential less than 10^{-5}.

6.5 Numerical Result for the Protein-Solvent Model

In the protein-solvent model, the origin of the coordinate system is at the center of the prototype protein molecule. The relative error in the numerical calculations is defined as

$$\mathrm{err}(x,y,z) \;=\; \frac{\left|u_{\mathrm{num}}(x,y,z) \;-\; u_{an}(x,y,z)\right|}{\left|u_{num}(x,y,z)\right|} \times 100\% \tag{6.12}$$

where u_{num} is the numerical potential and u_{an} is the quasi-analytic result introduced in Section 6.4. To eliminate the numerical error associated with the approximation of boundary conditions, the exact (theoretical) Dirichlet condition is applied on the domain boundary.

First, let the point charge be located inside the molecule, 6 Å from the surface, at (x, y, z) = (0, 0, 24 Å). The mesh size is 1.5 Å in each of the three direc-

tions. The error as a function of distance from the center of the protein molecule is evaluated as the relative RMSE over 100 points on any spherical surface of a given radius. These sample points are distributed evenly with respect to the θ and ϕ angles and with the step of 1 Å in the radial direction over all three layers of the protein-solvent model.

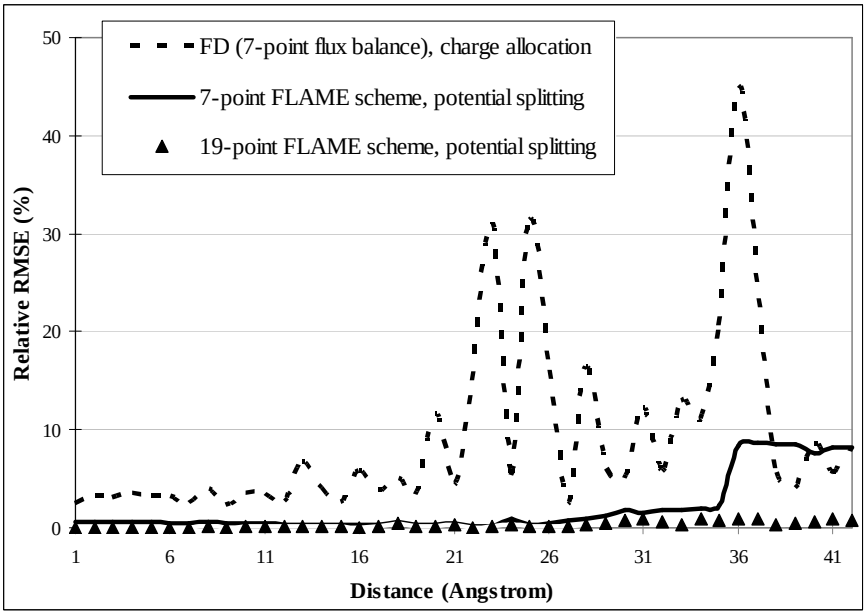

Figure 6.3: Errors as a function of distance from the center of protein. The protein has radius 30 Å, and the charge is located 6 Å below the protein surface (after [23], (c) 2008 IEEE).

Figure 6.3 shows that the accuracy of the FLAME solutions is much greater than that of standard FD with charge assignment. Note that the accuracy of FLAME is great even in the area around the point charge, where the potential is singular; this is because the potential of the charge is represented in FLAME exactly, by the

potential splitting described above. The average RMSE of seven-point FLAME and nineteen-point FLAME are 1.98% and 0.32% respectively compared to 8.96% for standard FD method. The nineteen-point FLAME scheme yields greater accuracy, at the increase of computation complexity.

In the second example, the point charge is much closer to the protein surface. Since in actual calculations all charges would lie at least 1 Å below the surface, the charge is assumed to be located at (x, y, z) = (0, 0, 29 Å), the worst-case scenario. In this case, to achieve high accuracy, the particular solution $u_f^{(i)}$ needs to contain a large number of harmonics in the expansion.

In the second example, the numerical errors are evaluated the same way as previous (Figure 6.4). FLAME again has much greater accuracy than the standard FD method. The average relative RMSE for the seven-point and nineteen-point FLAME schemes are 1.70% and 0.54%, respectively, compared with that for the standard FD scheme of 12.62%. Similar to the previous example, the accuracy for the seven-point FLAME scheme is slightly worse in the outer solvent layer; for the nineteen-point FLAME. the accuracy is high throughout the entire computational domain.

6.6 Conclusion

This chapter introduces a new computational model for the electrostatics of macromolecules (e.g. protein molecules) in solvents. Three dielectric layers are used: the interior of the protein with a low dielectric constant of $\sim$2 – 4; a thin layer of

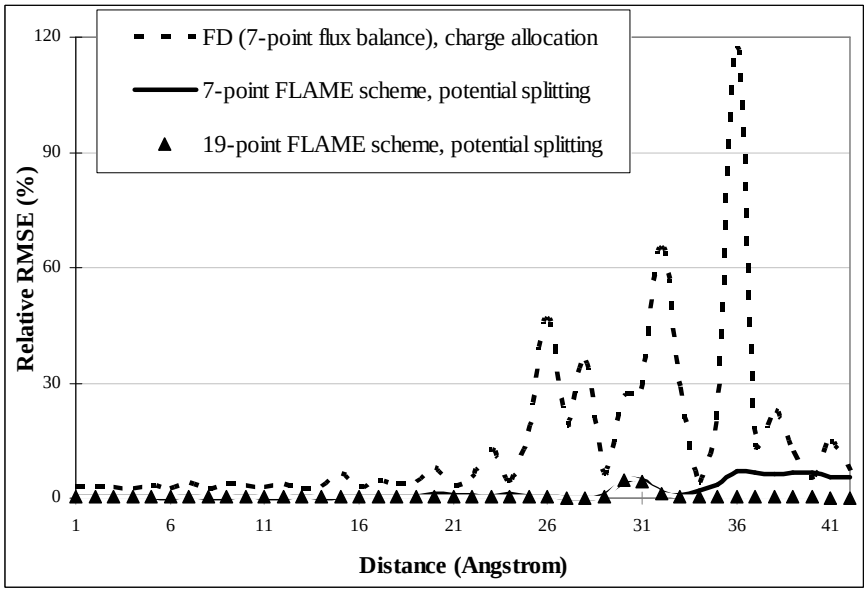

Figure 6.4: Errors as a function of distance from the center of the molecule. The radius of the molecule is 30 Å, and the charge is located 1 Å from the protein surface. $u_f^{(i)}$ is approximated by 50 harmonics (after [23], (c) 2008 IEEE).

solvent near the molecule with the dielectric constant of $\sim$6; and the bulk of the solvent, with the dielectric constant of $\sim$80. The electrolyte in the solvent layer is described by the linearized PBE. This model takes into account both short- and long-range dielectric response of solvent accurately.

The new general FD calculus of FLAME is used to discretize the electrostatic problem. With point charges as sources of the field, the potential splitting is used in FLAME instead of the conventional charge allocation to the grid. The numerical result shows much greater accuracy of FLAME, as compared with the standard FD analysis.

The accuracy of FLAME depends on the particular solution $u_f^{(i)}$ in the potential splitting. In the model problem, Coulomb's potential is used as this particular solution. A more accurate approximation, via spherical harmonics, may be needed if the point charge is close to the surface. Standard FD with charge allocation to the grid leads to substantially high errors, especially in the vicinity of the point charge due to the singularity [44]. FLAME produces great accuracy even for the area that is very close to the charge.

CHAPTER VII

MODELING OF FERROFLUID WITH VARYING CONCENTRATION

In this chapter, a model based on FEM is introduced to model the behavior of ferrofluids in the presence of external magnetic fields. This problem is important, in particular, for magnetic assembly of micro- and nanoscale systems, the technology developed by G. Friedman and B. Yellen [59, 60]. First, the background of magnetic self-assembly is presented. Then, this chapter focuses on the formulation of the ferrofluid concentration model. Finally, several simulation results are demonstrated to show the efficiency of the model.

7.1 Introduction

On the nanoscale, systems are difficult to fabricate or assemble, especially in traditional ways such as by humans with tweezers and microscopes or with high-precision pick-and-place robots. Self-assembly has been advocated as an automatic technology for forming a disordered system of pre-existing components into an organized structure or pattern as a consequence of specific local interactions [54]. This approach can be used as a controlled and directed nanofabrication process for desired patterns and functions.

Self-assembly techniques can be based on chemical recognition, surface tension, stress, electric, magnetic or optical forces [55]. Among these different types, only a few can easily program or dynamically control the movement and placement of individual components. Magnetically driven assembly is one of such techniques. This technology can be used to fabricate devices in low-temperature environments and in solvents compatible with virtually any biological material [56–58]. The magnetic force is usually not as strong as the electrostatic, Van der Waals, and surface tension forces [1]. However, it has advantages that facilitate its application in self assembly technology. The magnetic force in liquids can act over a much longer range than Van der Waals and surface tension forces, and the range can be varied (nanometers to meters) according to real applications. Also, the magnetic force can take advantage of the nonlinear behavior of magnetic materials [59]. Furthermore, magnetic interactions are insensitive to the surrounding medium and to the details of surface chemistry [54].

7.2 Magnetic Control of Ferrofluids

A ferrofluid contains tiny magnetic nanoparticles, roughly 10 to 20 nm in diameter, suspended in a non-magnetic liquid carrier. Due to the small size, ferrofluid particles remain stably suspended even under the influence of either gravity or moderate magnetic fields. The magnetic control of ferrofluid particles can be applied to prevent a given material from reaching a surface desired. This technology

is very important for the monolithic integration, photolithographic synthesis, and so on [61, 62].

For magnetic self-assembly of ferrofluid, the large number of ferrofluid particles poses an enormous computational challenge. To investigate the assembly process, a model is developed in this chapter to simulate magnetic self-assembly of ferrofluid. In this model, the phenomenon of ferrofluid accumulation is studied as a function of applied external field and the position with respect to the magnetic traps [1]. With different external fields, the ferrofluid is attracted variously to the magnetic trap, as Figure 7.1 shows [25].

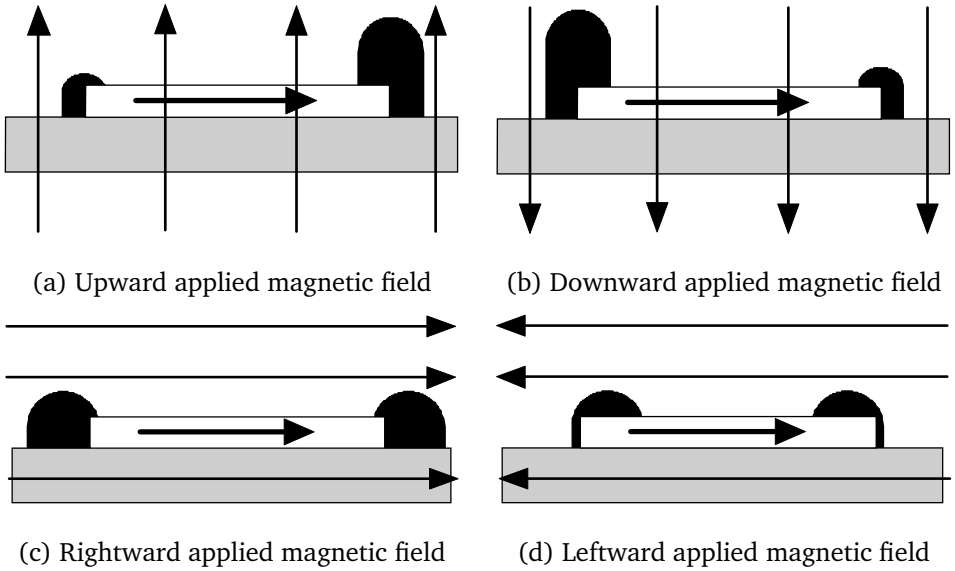

(a) Upward applied magnetic field (b) Downward applied magnetic field

(c) Rightward applied magnetic field (d) Leftward applied magnetic field

Figure 7.1: Ferrofluid assembly with different applied magnetic fields.

Based on the analysis of Yellen & Friedman [1, 2], the general relationship between particle concentration and magnetic field can be found by considering the

flux of particles and the quasi-continuum description of ferrofluid concentration. Caused by magentic forces, the flux can be separated into two components: one is due to diffusion and the other is due to drift [63].

$$\vec{J} = \vec{J}_{diff} + \vec{J}_{drift} = -D\nabla c + c\vec{v} \tag{7.1}$$

where D is the diffusion coefficient for the ferrofluid particle, $\vec{v}$ is the velocity of the particles, c is their volume concentration.

After an external magnetic field is applied, a transient flux of particles will occur until a new balance state is reached (the net fluid velocity becomes zero again at the new balance). In the new balance, the magnetic force acting on a uniformly magnetized particle is proportional to the difference in the particle magnetization and average fluid magnetization [64]. Then, the particle's velocity, approximately proportional to the magnetic force, is

$$\vec{v} = \gamma\vec{F_m} = \gamma\mu_0 V(\vec{M}_p - \left\langle \vec{M} \right\rangle) \cdot \nabla\vec{H} \tag{7.2}$$

where $\vec{F_m}$ is the magnetic force, γ is the mobility, $\vec{H}$ is the local magnetic field, $\vec{M}_p$ is the particle magnetization (magnetic moment per unit volume), $\left\langle \vec{M} \right\rangle$ is the average magnetization of the fluid surrounding the particle, μ_0 is the permeability of a vacuum, and V is the particle volume. The average magnetization is given as

$$\left\langle \vec{M} \right\rangle = \vec{M}_p c \tag{7.3}$$

The flux is zero ($\vec{J} = 0$) at equilibrium. Combining equations (7.2) and (7.3), we get

$$D\nabla c = \gamma\mu_0 V c(1-c)\vec{M}_p \cdot \nabla\vec{H} \tag{7.4}$$

This equation can be further transformed as

$$\frac{1}{c(1-c)}\nabla c = \frac{\gamma}{D}\mu_0 V \vec{M}_p \cdot \nabla \vec{H} \tag{7.5}$$

The left side can be written as

$$\frac{1}{c(1-c)}\nabla c = \left(\frac{\nabla c}{c} + \frac{\nabla c}{1-c}\right) = \nabla \ln \frac{c}{1-c} \tag{7.6}$$

According to the Einstein relation [65], the ratio of mobility of diffusivity is

$$\frac{\gamma}{D} = \frac{1}{k_B T} \tag{7.7}$$

where k_B is the Boltzmann constant and T is the absolute temperature. Together with (7.5) and (7.6), we get

$$\frac{1}{c(1-c)} = A \exp\left(\frac{\mu_0 V \vec{M}_p}{k_B T}\vec{H}\right) \tag{7.8}$$

where A is a constant to be determined. When there is no magnetic field applied ($\vec{H} = 0$), the ferrofluid particles are uniformly distributed (assuming the initial corresponding concentration of ferrofluid is c_i). Based on this condition, it is easily calculated as $A = \frac{c_i}{1-c_i}$.

Using field-dependent effective susceptibility [66], we can get

$$\vec{M}_p = \chi(\vec{H})\vec{H} \tag{7.9}$$

where the initial susceptibility $\chi(\vec{H})$ (later written simply as χ) is equal to $\frac{\mu_0 V {M_s}^2}{3k_B T}$ when assuming there are no magnetic interactions among the particles. Here M_s is saturation magnetization of particles. From now on, it can be seen that the

ferrofluid concentration is a function of $\vec{H}$. The ferrofluid concentration is then as

$$c(\vec{H}) = \frac{1}{1 + A^{-1} exp\left(-\frac{B^2 \vec{H}^2}{6}\right)} \tag{7.10}$$

where $B = \frac{\mu_0 V_p M_s}{k_B T}$.

Having found the general relationship between particle concentration and magnetic field, we can now formulate a self-consistent problem for the magnetic field. The magnetic field of the domain outside the trap is governed by

$$\nabla \cdot B = \nabla \cdot \left(\chi c(\vec{H}) + 1\right) \mu_0 \vec{H} = 0 \tag{7.11}$$

Here, the concentration $c\left(\vec{H}\right)$, instead of magnetic potential or field, is the main variable of interest for the ferrofluid assembly model. The scalar magnetic potential instead of the vector one is used to reduce the computational cost substantially. By the relation of $\vec{H} = -\nabla\Psi$ where Ψ is the scalar magnetic potential, (7.11) goes to

$$-\nabla \cdot (\chi c\,(\Psi) \;+\; 1)\,\mu_0 \nabla\Psi \;=\; 0 \tag{7.12}$$

Inside the magnetic trap, the governing equation is

$$-\nabla \cdot \left(\mu_0 \nabla\Psi - \vec{M}\right) \;=\; 0 \tag{7.13}$$

7.3 The Setup for the Ferrofluid Concentration Model

In the real experiment, there are several magnetic traps forming a regular pattern on the substrate (Figure 7.2) [1]. The whole structure is placed in a container filled

with ferrofluid. An external magnetic field that is parallel or perpendicular to the direction of the magnetic traps is applied.

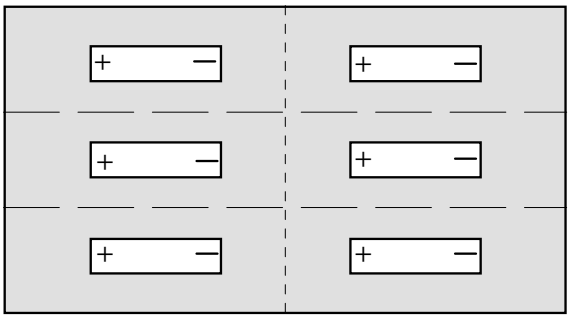

Figure 7.2: Placement of magnetic traps.

The previous chapters dealt primarily with FLAME. In this Chapter, we use FEM, as the most powerful tool for problems with complex geometries and non-homogeneous media. COSMOL Multiphysics^{TM} is used for the simulation. This requires setting up the geometry, boundary conditions and governing equations. The bigger the computational domain, the more accurate the numerical result will generally be. However, the computational cost is greater for larger domains. To reduce this cost, only one magnetic trap is modeled. A large, rectangular micro-magnet trap of approximately 100nm in thickness is used in the simulation with planar dimensions of 4 by 20μm. The computational domain is as 40 by 40μm in the surface of the substrate and 20μm in perpendicular direction, which is large enough to get sufficient accuracy with reasonable computation cost. The geometric setup is shown in Figure 7.3.

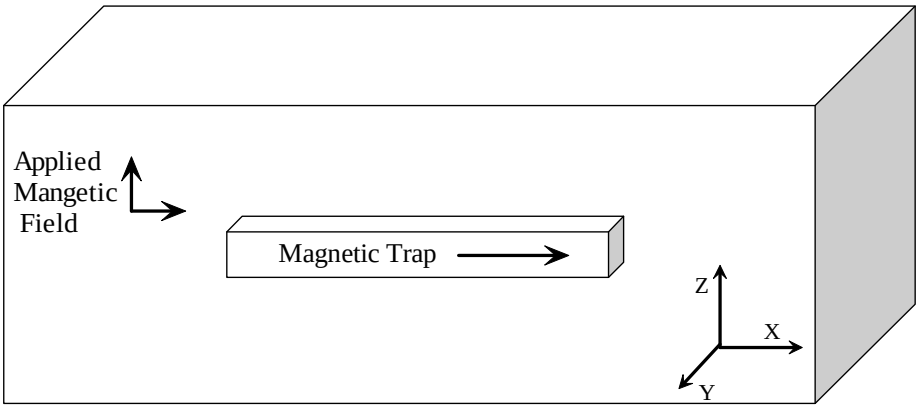

Figure 7.3: Setup for ferrofluid assembly.

In the simulation, ferrofluid is assumed to be a suspension particle about $15nm$ in diameter with saturation magnetization of 4600 Gauss, with the initial concentration of 1% solids by volume. On the YZ interface the Dirichlet condition and on the XZ interface the Neumann condition are imposed. Due to the sufficient separation between the boundary and the trap in the Z direction, the XY interface could also be set as a Dirichlet condition.

7.4 Numerical Results for the Ferrofluid Concentration Model

When the magnetic trap is magnetized as in Figure 7.3 and an uniform magnetic field is normal to the plane, the ferrofluid accumulates near one magnetic pole depending on the direction of the field bias with respect to the trap's magnetization, as Figure 7.1 (a) and (b) shows. Figure 7.4 demonstrates the ferrofluid distribution with an external magnetic field in an external 150 Gauss magnetic field applied

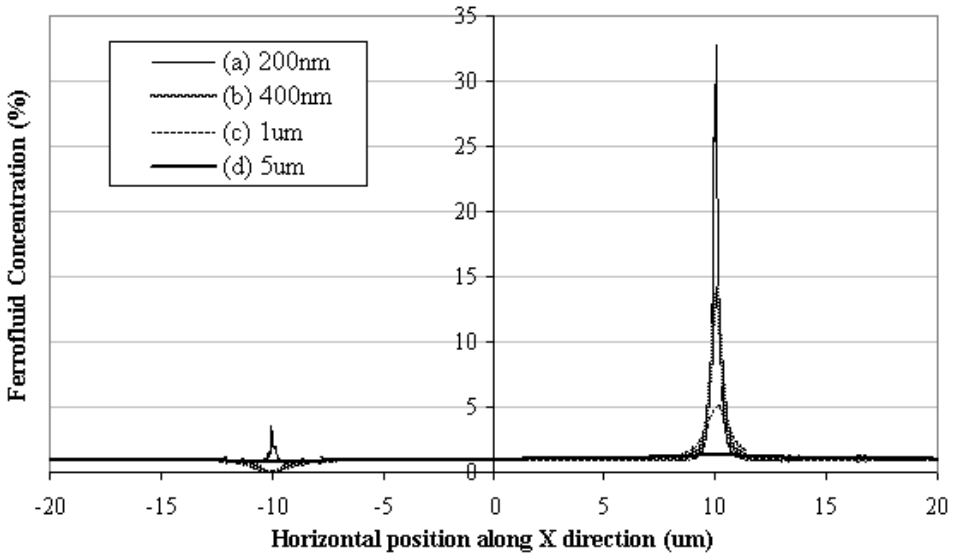

Figure 7.4: Ferrofluid concentration profiles in the horizontal lines with a field applied upward.

upward. The ferrofluid concentration is depicted as a function of position. In reference to Figure 7.3, the magnetic trap is located from -10μm to 10μm along the X axis, -2μm to 2μm along the Y axis, and 0 to 100 nm along the Z axis. The line in Figure 7.4 labeled as "(a) 200 nm" represents the horizontal line in the X direction, with Z = 200 nm. Similar definitions are used for other three lines.

When the magnetic trap is uniformly magnetized from left to right, the applied field is the same upward direction as the externally applied field on the right side and the ferrofluid accumulates on the right side, with an intuitive explanation that "opposite poles attract" (refer to Figure 7.1(a)). Solution of (7.12) for the right side of the trap shows that the concentration decreases away from the trap, as can be expected Figure 7.5. The starting point on the horizontal axis in the

figure corresponds to the top of the trap (100 nm). The simulation result can be approximated accurately enough by the simple rational function $f(x) = \frac{a_1}{x} + a_2$.

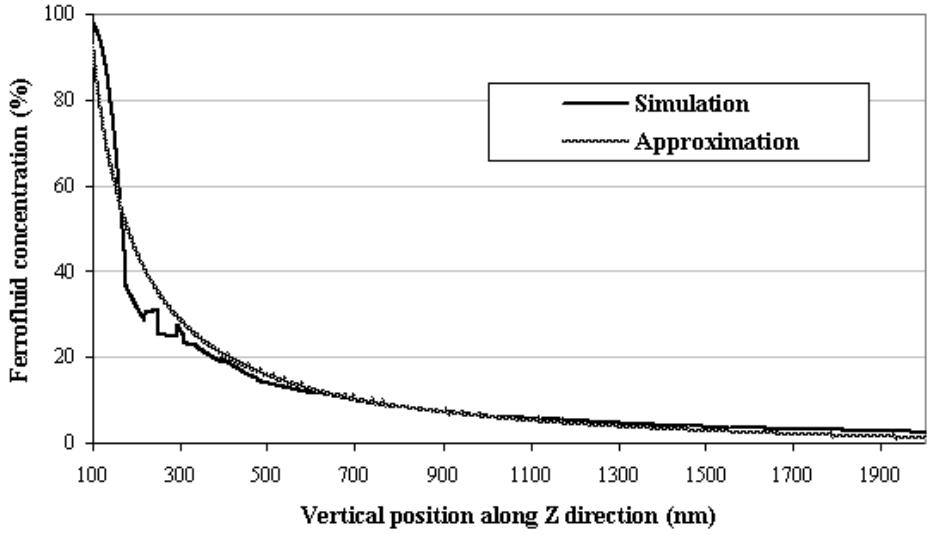

Figure 7.5: Ferrofluid concentration simulation and approximation for applying upward field.

Similarly, the ferrofluid accumulates on the left side of the trap when the external magnetic field is applied downward. Figure 7.6 shows the ferrofluid distribution with an external magnetic field of 150 Gauss applied downward. Figure 7.6 has the same definition for the lines as Figure 7.4 and exhibits an almost opposite result compared with Figure 7.4.

When the external magnetic field is applied horizontally, the ferrofluid accumulates either on top of or extends to the edges of the micro-magnet depending on the orientation of the external field with respect to the trap's direction of mag-

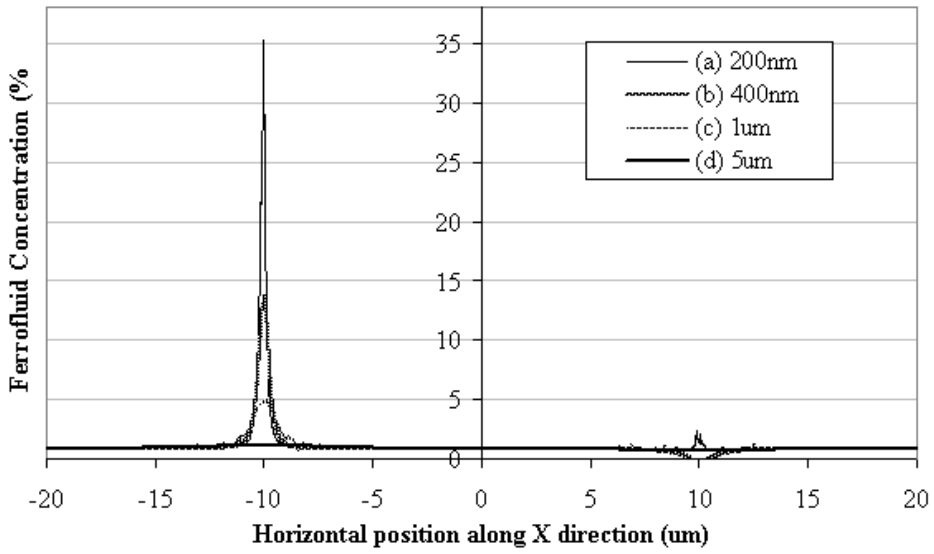

Figure 7.6: Ferrofluid concentration profiles in the horizontal lines with a field applied downward.

netization. The diagram in Figure 7.7 shows the ferrofluid arrangement with the external magnetic field applied anti-parallel or parallel to the trap's magnetization.

Due to the symmetric ferrofluid distribution, for both the anti-parallel and parallel applied magnetic field, Figure 7.7 only shows the left part of the geometry (trap). Anti-parallel or parallel is related to the direction of the trap's magnetization. Since "opposite poles attract", the ferrofluid tends to accumulate on the trap for the anti-parallel applied field. When the external magnetic field is parallel, the ferrofluid extends off the ends of the trap.

In order to give a general idea of how the ferrofluid concentration varies as a function of the magnitude of the applied magnetic field, a graph is provided in Figure 7.8. The series of curves in the graph represents the ferrofluid concentrations

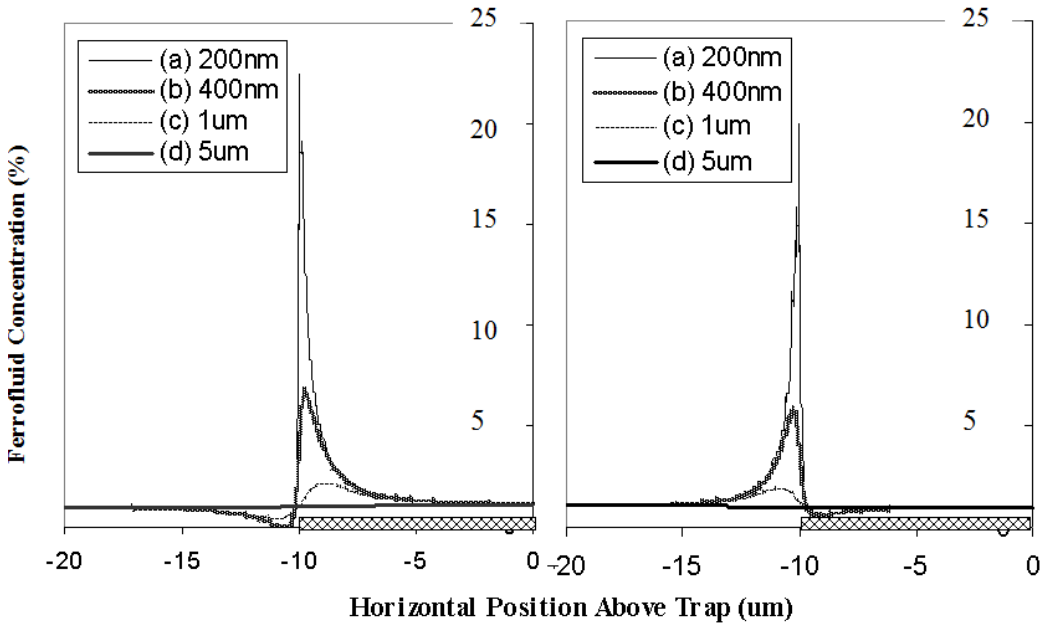

Figure 7.7: Ferrofluid concentration profiles in the horizontal lines with anti-parallel and parallel external applied field.

with 0, 50, 100, and 150 Gauss magnetic fields applied toward the right of the trap's magnetization. These curves are for the horizontal line that is 400 nm above the bottom surface of the magnetic trap. This graph indicates that the stronger the magnetic fields applied, the higher the ferrofluid concentration above the trap, and the concentration extends farther off the trap.

7.5 Conclusion

This chapter introduced a model of ferrofluids with varying magnetic particle concentration. The magnetic self-assembly technology can be very useful in monolithic integration and photolithographic synthesis because the ferrofluid has several ad-

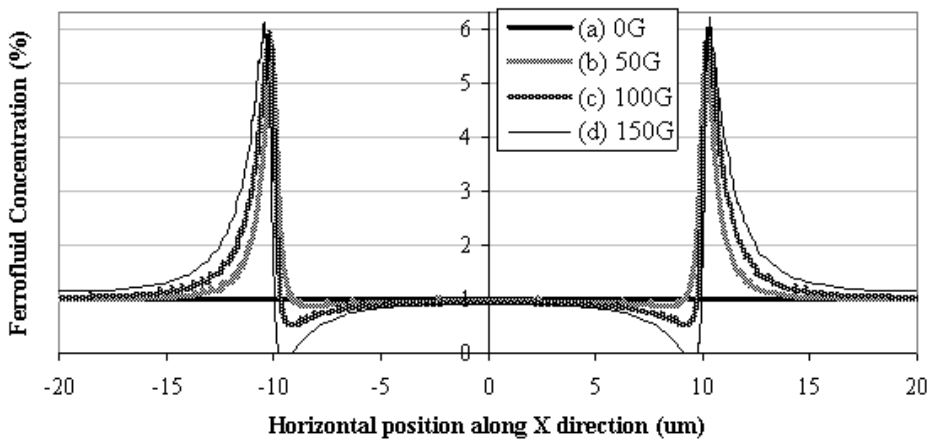

Figure 7.8: Ferrofluid concentration profiles in the horizontal lines, with a field applied parallel.

vantages as a masking material. With the quasi-continuum approach of ferrofluid concentration, the general relationship between particle concentration and magnetic field is approximated by the equation (7.11). To further minimize the computational cost, the field problem is formulated in terms of the scalar, rather than vector, magnetic potential.

The simulation of this chapter is based on FEM, and only one magnetic trap is selected for simplification. The results correspond to the analysis as Figure 7.1 shows. The determining factors are the direction and magnitude of both the magnetic trap's magnetization and the external applied magnetic field. Simulations provide a useful insight into experiments and analysis of magnetic self-assembly.

CHAPTER VIII

ELECTRODYNAMIC EFFECTS IN PLASMONIC NANOLENSES

In this chapter, plasmonic field enhancement is studied using the FEM. A nanolens comprised of three spherical metal particles (also refer to as particle cascade) produces very high plasmonic field enhancement. Electrodynamic resonances are identified and a significant local field enhancement (by a factor of hundreds) is found for different sizes and fractal ratios of the particle cascade system, and for different polarizations and directions of incidence of the excitation radiation. The simulation results give an insight into the optimal design of such nanolenses for their applications in spectroscopy and sensing.

8.1 Introduction

The study of optical phenomena related to the electromagnetic response of metals on the nanoscale has been termed as nanoplasmonics. It is one of the key investigations in nanooptics, which is experiencing a period of explosive growth in both its fundamental development and applications. This rapidly growing field of nanoscience is primarily concerned with the control of optical radiation on the subwavelength scale. Nanoplasmonics has practical applications in many areas, such

as sensor technology, apertureless near-field spectroscopy, optoelectronics, high-density lithography, and biomedical labeling. It deals with electric (surface plasmons [SPs]) and electromagnetic (surface plasmon polaritons [SPPs]) excitations at metal surfaces and metal/dielectric interfaces. The noble metals, such as gold and silver, can efficiently excite the SPs using their similar free-electron behavior. When the particles are much smaller than the wavelength of the exciting light, all conduction electrons of the particles are excited in phase, which leads to remarkable SPs. The frequency of the highest SPs depends on the particle material, the particle structure, and the refractive index of the surrounding medium [69].

Optical near-fields are localized either in the source region of optical radiation or in the materials' surfaces that interact with free radiation. These near-fields determine the enhancement of the plasmonic fields. This enhancement plays a key role in many effects and applications of nanoplasmonics, particularly in near-field scanning optical microscopy (NSOM) and in detectors of chemical and biological objects. Both SPs and near-fields deal with optical interactions on a subwavelength scale [67, 68]. For the optical structure excited by light, the size needs to be at the nanometer level, which is less than the wavelength of the exciting light.

The surface plasmons exist in various nanostructures, from thin metal films to small noble metal particles of different shapes. Plasmon resonances are dependent on the type of metal used and the dielectric constant of the surrounding medium. They are also strongly dependent on the size and shape of the nanostructure [70, 71]. Many plasmonic effects can be analyzed in the framework of

classical electrodynamics [71]. Therefore, the electrodynamics theory can be used to explore the properties of nanostructures.

8.2 Modeling of Electrodynamic Effects in Plasmonic Nanolenses

We use numerical simulation to explore the large field enhancement by nanoparticles, with wave effects taken into account. According to equation (1.8) in Chapter 1, electric field $\mathbf{E}$ is governed by the following wave equation (in the absence of source currents):

$$\nabla \times \left(\frac{1}{\mu} \nabla \times \mathbf{E} \right) - \omega^2 \epsilon \mathbf{E} \; = \; 0 \tag{8.1}$$

where the standard notations for the angular frequency ω and the (absolute) permittivity and permeability ϵ and μ are used. All interface boundaries that cause scattering are assumed to be inside the computational domain Ω. The solution of (8.1) can be decomposed into two parts, the incident field $\mathbf{E_{inc}}$ and the scattered field $\mathbf{E_s}$, i.e.

$$\mathbf{E} \; = \; \mathbf{E_{inc}} \; + \; \mathbf{E_s} \tag{8.2}$$

where

$$\mathbf{E_{inc}} \; = \; E_0 e^{-j(\omega_c t - \theta_0)} \tag{8.3}$$

Here, E_0 and θ_0 are the amplitude and phase of the incident field. Thus, the governing equation for the scattered field is ($\mu = \mu_0$ for nonmagnetic material)

$$\nabla \times \nabla \times \mathbf{E}_{\mathrm{s}} - \omega^2 \mu_0 \epsilon \mathbf{E}_{\mathrm{s}} \; = \; -(\nabla \times \nabla \times \mathbf{E}_{\mathrm{inc}} - \omega^2 \mu_0 \epsilon \mathbf{E}_{\mathrm{inc}}) \tag{8.4}$$

The differential operators should be understood in the sense of distributions that include surface delta functions for charges and currents. The right side of the equation is nonzero due to these surface terms and the volume term inside the particles. The incident field is governed by the wave equation with the wavenumber of free space.

A significant problem in plasmonics is the design and arrangement of metal particles that would produce the strongest possible field enhancement. One possible solution to this problem is a self-similar chain of particles with decreasing diameters, as depicted in Figure 8.1.

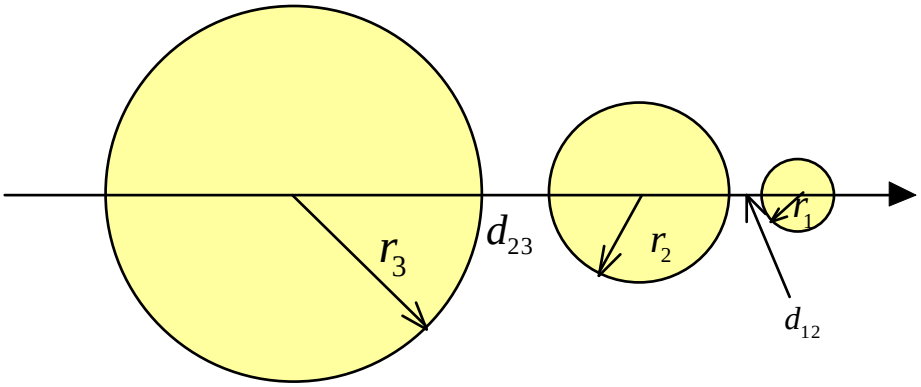

Figure 8.1: A two dimensional representation of the metal cascade.

In this model, the three nanoparticles have the radii r_1, r_2, and r_3, with air gaps of d_{12} and d_{23}. They follow the relation as $r_1 = \kappa r_2$, $r_2 = \kappa r_3$, $d_{12} = \kappa d_{23}$, $d_{12} = \eta r_1$, where κ and η are constants that are both less than 1. Under the plasmon resonance condition [72], the middle particle experiences the electric field

that is strongly enhanced by the large one. The middle particle further amplifies the field at the location of the small particle. If the parameters of the system are chosen judiciously, extremely high local field enhancement is produced near the small particle. This phenomenon can be interpreted as "nano-focusing". The field enhancement in this chapter is defined as $g = |\mathbf{E}| / |\mathbf{E_{inc}}|$. As analyzed in Li et al. [73], the greatest field enhancement that the small nanoparticle of the silver cascade can achieve is really high. In reality, the field enhancement is affected by the size of the cascade, the material of the nanoparticles, the wavelength, the direction and polarization of the incident wave. The field behavior needs to be analyzed as a funtion of multiple varying factors.

Silver and gold nanoparticles exhibit relatively stronger plasmonic enhancement compared with other materials or morphologies [73, 74]. The simulations in the present chapter focus on silver models. The model problem is formulated in an unbounded spatial domain. It is common practice to enclose the bounded domain of real interest with an artificial computational boundary. The boundary conditions for the scattered field should accurately represent the outward radiation of energy. Thus outgoing waves should be absorbed by the computational boundary so that no artificial reflections are sent back into the interior. Two kinds of boundary conditions, perfectly matched layers (PML) and radiation boundary conditions, are used for this purpose.

The PML is a fictitious layer specially designed to absorb the electromagnetic waves without reflection from the vacuum layer interfaces [75]. The perme-

ability and the permittivity of this fictitious material are complex anisotropic [76]. The radiation boundary condition is [77]

$$(\nabla \times \mathbf{E})_{tan} \;=\; jk_0\mathbf{E_{tan}} - \frac{j}{h_0}\nabla_{tan} \times (\nabla_{tan} \times \mathbf{E_{tan}}) + \frac{j}{k_0}\nabla_{tan}(\nabla_{tan} \cdot \mathbf{E_{tan}}) \qquad (8.5)$$

where E_{tan} is the component of the E-field that is tangential to the surface, and k_0 is the free space phase constant $\omega\sqrt{\mu_0\epsilon_0}$. The accuracy of the approximation depends on the distance between the boundary and the object from which the radiation emanates.

8.3 A Crude Approximation of the Cascade Enhancement

To get higher plasmonic enhancement, the wavelength of the incident light should be much longer than the structure. With this in mind, the electrostatic crude analysis can be used as a first approximation. We consider silver nanoparticles in free space, with frequency dispersion $\epsilon = \epsilon(\omega)$ taken into account. In the example under consideration, the dimensions are $r_1 = 5$nm, $\kappa = \frac{1}{3}$ and $\eta = 0.6$, so the total length of the structure is 142 nm.

For a single silver nanoparticle, the field enhancement is easily calculated via the respective dipole field. Assuming the incident light has the frequency 814.8 THZ, the corresponding dielectric constant is calculated as $-2.7407 + 0.2320i$ according to Johnson & Christy [78]. Using this value, the field enhancement for one particle is $g_{static} = 10.93$. In the three-particle cascade of Figure 8.1, the middle particle is relatively small compared with the large one. The field that is induced

by the large particle can be treated as the incident light for the middle one. The same crude approximation can be considered for the relation between the middle nanoparticle and the smallest one. Thus, finally, the small nanoparticle will yield the greatest field enhancement, on the order of g_{static}^3 (about $1,000$).

8.4 Numerical Results for Silver Nanoparticles

The silver cascade model with three particles is shown in Figure 8.2. The physical dimension is the same as for quasistatic analysis in Section 8.3. Under the electrostatic analysis, the maximum field enhancement is calculated to occur in the near-ultraviolet zone at $\hbar\omega = 3.37$ eV, with the corresponding wavelength of $\sim$367.9 nm (the same frequency was taken in Section 8.3).

Four independent combinations of the directions of wave propagation and polarization (left-right and up-down direction are in reference to Figure 8.2) are considered:

- The incident wave propagates from right to left. Electric and magnetic fields are both perpendicular to the axis of the cascade. (Mnemonic label: $\Leftarrow\perp$.)
- Same as above, but the wave impinges from the left. ($\Rightarrow \perp$)
- The direction of propagation and electric field are both perpendicular to the axis of the cascade. ($\Uparrow \perp$)
- The direction of propagation is perpendicular to the cascade axis and the electric field is parallel to it. ($\Uparrow \parallel$)

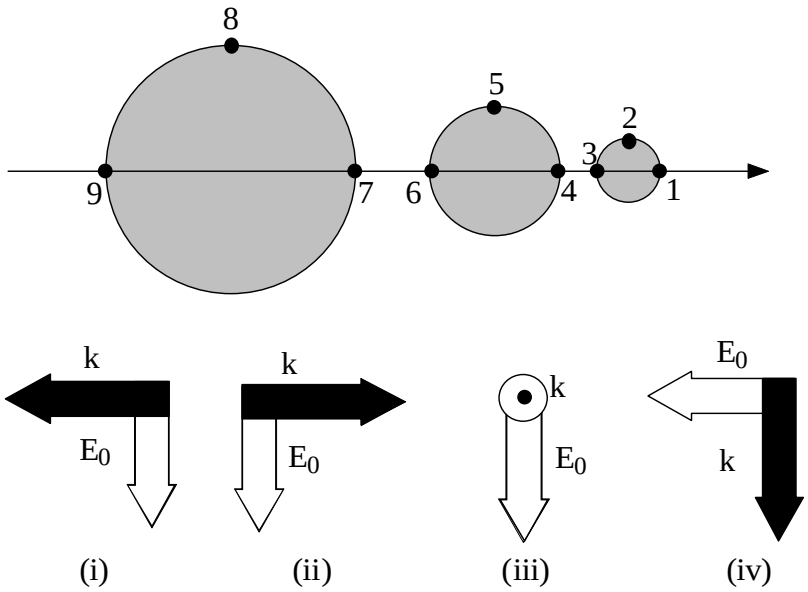

Figure 8.2: Two dimensional representation of the silver cascade of three particles and the wave propagation (after [79], (c) 2008 APS).

Several popular numerical methods can be used for nanooptics simulations. Optical excitations on a single silver nanosphere and nanosphere composites were investigated by FDTD method [11]. As mentioned in Chapter 1, FDTD method is subject to the notorious "staircase effect" at curved boundaries. Thus spherical boundaries of the nanoparticles produce relatively significant errors in the simulation. COMSOL Multiphysics, a software package based on FEM, was used to simulate the field distribution of optical antennas constiting of several nanoparticles [35]. Since field enhancement is very highly localized and decreases very rapidly away from the "hot spot" in the structure, the area around the hot spot requires an extremely fine mesh.

For wave analysis, we use the commercial software package HFSS™ by Ansoft corporation. Caution should be exercised when representing the measured Johnson & Christy data [78], with its $\exp(-\mathrm{i}\omega t)$ convention for phasors, as the HFSS input, with its $\exp(+\mathrm{i}\omega t)$ default. In the electrostatic case, we use COMSOL Multiphysics. Both HFSS and COSMOL are FEM based; second-order triangular nodal elements for the electrostatic problem and tetrahedral edge elements with 12 degrees of freedom for wave analysis are used. HFSS employs automatic adaptive mesh refinement for greater accuracy. Either radiation boundary or PML is used to truncate the unbounded domain.

To assess the numerical accuracy of HFSS, wave scattering from a single particle is analyzed by HFSS and the Mie theory [80] for comparison. The Mie theory is a complete analytical solution of Maxwell's equations for the scattering of electromagnetic radiation by spherical particles. For the radius of a single particle varying from 5 to 60 nm, the numerical accuracy for the electric field at the "hottest spot" is within 1.2–3.5% for a dielectric particle with $\varepsilon = 10$ and within 3.4–6.3% for a silver particle with $\varepsilon = -2.7407 + 0.2320i$.

Figure 8.3 illustrates a sample distribution of the magnitude of the total electric field in the cross section of the cascade. In this sample, the incident wave is polarized along the axis of the cascade and propagates downward. It shows that the area around the smallest silver particle has the greatest field enhancement.

An example mesh created by HFSS is shown in Figure 8.4. The entire computational domain is subdivided into 99,168 tetrahedral elements for wave analysis.

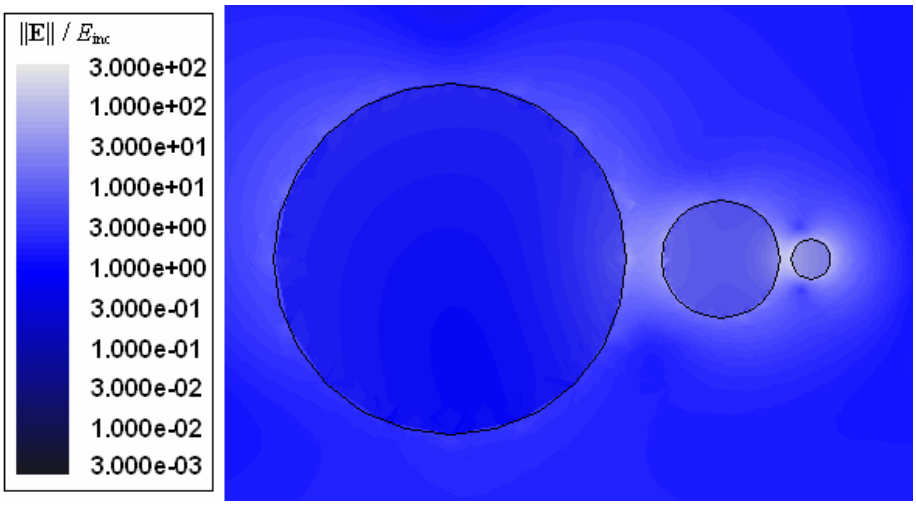

Figure 8.3: Electric field enhancement factor around the cascade of three plasmonic spheres (after [79], (c) 2008 APS).

HFSS adopts adaptive mesh refinement. The smallest side length of the tetrahedra is only about 0.5 nm compared with the wavelength, which is 367.9 nm. To make the mesh clearer, a hybrid 2D/3D view is used in Figure 8.4, with some of the elements in the volume omitted.

Table 8.1 shows field enhancement factors at the reference points for cases (i)–(iv) (see Figure 8.2). The hottest spot, i.e. the point of maximum enhancement, is indicated in bold and is different in four cases. Here, the field enhancement is measured by the $ComplexMag\_\mathbf{E}$:

$$ComplexMag\_\mathbf{E} = \sqrt{|\mathbf{E_x}|^2 + |\mathbf{E_y}|^2 + |\mathbf{E_z}|^2} \tag{8.6}$$

When the electric field is perpendicular to the axis of the cascade, the local field is amplified by a very modest factor $g < 40$. Not surprisingly, the enhancement is

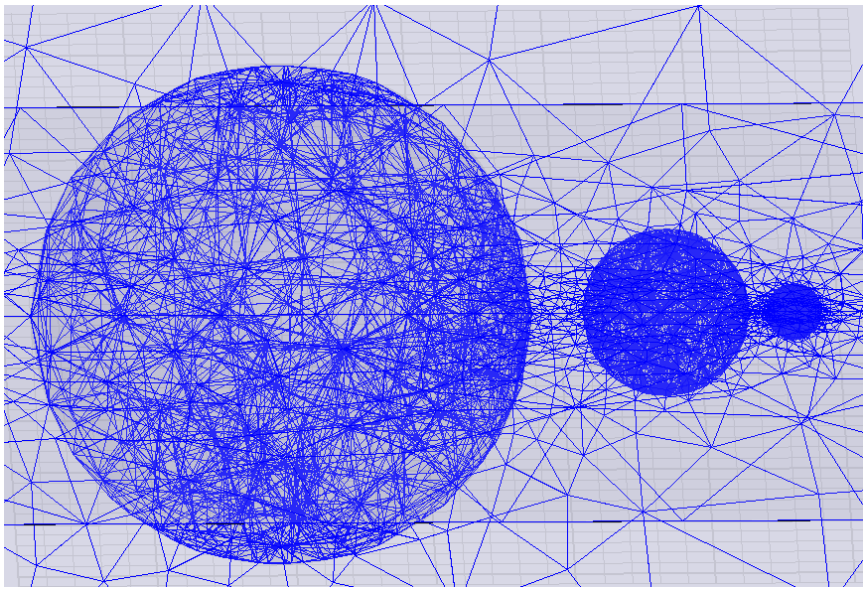

Figure 8.4: A sample HFSS mesh around the cascade , hybrid 2D–3D rendition of the 3D mesh used for visual clarity (after [79], (c) 2008 APS).

much greater ($g \approx 250$) in case (iv), when the field and the dipole moments that it induces are aligned along the axis.

The corresponding COMSOL Multiphysics electrostatic model related to case (iv) above, shows the field enhancement of $\sim$640. This enhancement is much greater than in the electrodynamic case. To gauge the influence of electrodynamic effects, more simulations are conducted to analyze the field enhancement as a function of the system size. Scaling is applied across the board: all the radii of the particles and the air gaps between them are multiplied by the same factor. The radius of the smallest particle, with its original value of 5 nm as reference, is used as the independent variable for plotting the result (Figure 8.5).

Table 8.1: Field enhancement at the reference points (Figure 8.2) for different propagation and polarization of the incident wave (after [79], (c) 2008 APS).

Case	Point 1	Point 2	Point 3	Point 4	Point 5	Point 6	Point 7	Point 8	Point 9
$\Leftarrow\perp$	5.45	17.3	10.2	9.43	**34.4**	10.7	5.53	10.4	3.21
$\Rightarrow\perp$	6.37	6.49	2.41	1.43	4.17	3.39	3.91	**11.2**	2.00
$\Uparrow\perp$	2.44	8.48	6.65	7.60	**23.3**	8.31	4.69	10.1	2.61
$\Uparrow\parallel$	90.8	35.9	**250**	146	10.3	70.9	51.9	2.72	6.47

The enhancement factor drops rapidly as the system expands for $r_1 > 3$nm. This can be easily explained by dephasing effects. The result also shows an interference pattern typical for antennas with very low enhancement numbers around $r_1 = 7.5$nm and $r_1 = 15$nm, where destructive interference takes place. The enhancement factor stays near the value $g = 630$ (the quasistatic approximation at Ref. [73]) for $r_1 < 1nm$ and is close to this value for $r_1 \leq 2.5$nm. At $r_1 = 1.2$nm, the nanolens exhibits an electrodynamic resonance with $g \approx 750$, which exceeds the quasistatic value significantly.

The result in Figure 8.5 applies to the nanolens with the fractal ratio $\kappa = 3$. The highest enhancement factor happens when the radii of the silver particles are $r_1 = 1.2$nm, $r_2 = 3.6$nm, $r_3 = 10.8$nm, and the particle gaps $d_{12} = 0.72$nm, $d_{23} = 2.16$nm. In practice, these dimensions are too small. Therefore, optimization of the nanolens for maximum enhancement as a function of the fractal ratio κ is of

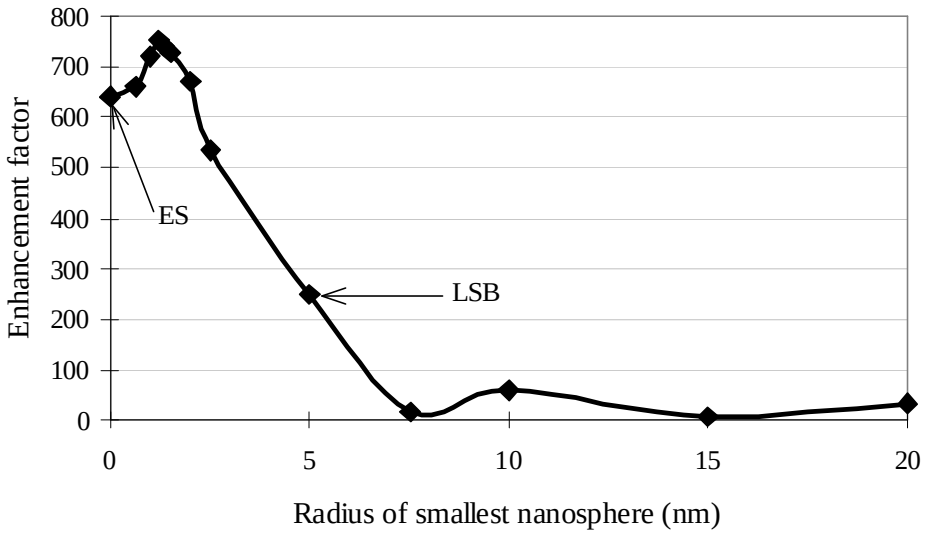

Figure 8.5: Maximum field enhancement vs. radius of the smallest particle, all dimensions of the system are scaled proportionately (LSB: dimensions as in the specific example in [73]; the radius of the smallest particle 5 nm, ES: the electrostatic limit, After [79], (c) 2008 APS).

interest. The relevant simulation results is shown in Figure 8.6. The wavelength and the polarization of the incident wave are the same as those of Figure 8.5. The greatest field enhancement is found at $\kappa \approx 2.6$ and is approximately 25% greater than for the original value, $\kappa = 3$. The electrostatic calculation based on the multipole-multicenter expansion is also shown in Figure 8.6. It is found that the quasi-static enhancement factor keeps increasing with the fractal ratio κ.

In the actual application of an optical sensor or antenna, the system is very likely to be placed on a substrate, as shown in Figure 8.7. The substrate is chosen to be constituted by the silicon dioxide ($\epsilon = 1.5$). In the simulation, the smallest par-

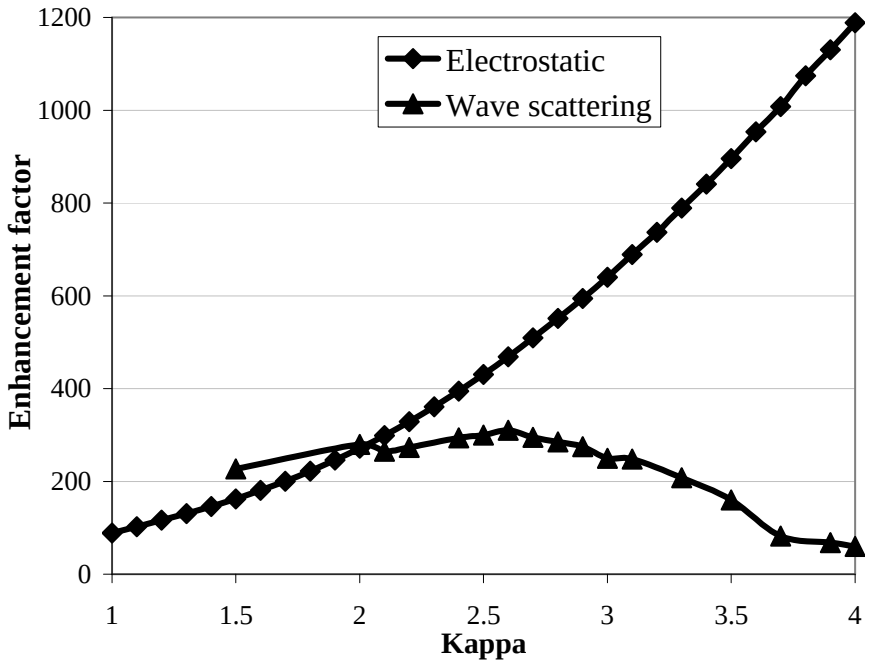

Figure 8.6: Maximum field enhancement vs. coefficient κ, with the smallest radius of silver particle 5 nm and the smallest air gap 3 nm (after [79], (c) 2008 APS).

ticle and air gap goes to 5 nm and 3 nm, respectively. Two kinds of incident waves are considered in the simulations: (I) One wave travels vertically, and is polarized parallel to the substrate; (II) The other wave travels vertically, and is polarized parallel to the cascade line. The enhancement factors at two points, shown as a and b in Figure 8.7, are listed in Table 8.2.

Comparing points a and b, the greater enhancement factor always happens at point a, no matter which kind of incident wave is applied. This is not surprising, since point a is the closest point from the smallest particle to other particles. It is found that the applied incident field in case I will cause a greater enhancement fac-

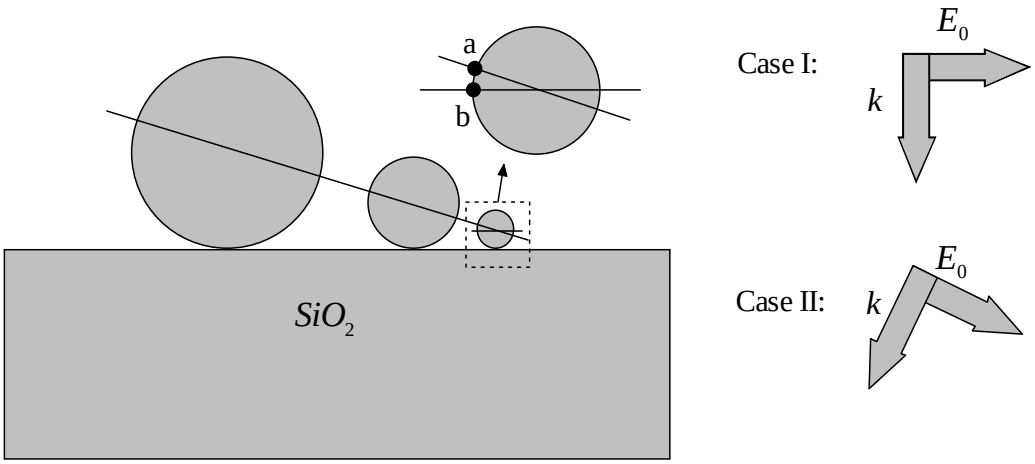

Figure 8.7: Particle cascade on a substrate (after [79], (c) 2008 APS).

tor than that of case II. Interestingly, the maximum enhancement is found when the excitation field is polarized at an angle (approximately 22.5^o) to the axis of the cascade for both situations, with and without the substrate. The multipole-multicenter calculation for cylindrical silver particles yields qualitatively similar results.

8.5 Conclusion

While electrostatic analysis provides a useful insight into plasmonic field enhancement, electrodynamic effects lead to appreciable corrections. The results confirm that field enhancement factors are on the order of a few hundred. For a self-cascade of silver nanoparticles, there exists a pronounced nanofocus where the local field is significantly enhanced (by a factor of several hundreds) with respect to the incident field. These simulations, both in wave and electrostatic situations, show that elec-

Table 8.2: Maximum field enhancement factor with and without substrate (after [79], (c) 2008 APS).

	With substrate		Without substrate	
	Case I	Case II	Case I	Case II
Point a	292	209	338	250
Point b	217	154	252	178

trodynamic effects are determined by the dimensions of nanolenses system if keep the particle's parameters and incident wavelength unchanged, with both positive and negative resonances possible. The positive resonance part shows significantly greater enhancement than the quasistatic case. The negative resonance part, the greatest enhancement vanishes quickly with the increase of the system dimensions. Maximum enhancement does not necessarily correspond to polarization along the axis of the cascade and to the electrostatic limit; hence, the size of the system is a nontrivial variable in the optimization of optical nanolenses. Another clear possibility for optimizing and improving the nanofocusing of optical radiation would be to decrease the air gaps between nanoparticles. However, for smaller gaps, the continuous electrodynamics approach is no longer applicable.

CHAPTER IX

CONCLUSION

A number of simulation models for multiobject nanoscale systems have been developed, studied and implemented in the thesis. The models are focused on electromagnetic interactions, both quasistatic and dynamic, and employ traditional as well as novel computation techniques. Multi-object systems are quite challenging to model, as they typically require substantial or even impractical computation resources. The thesis explores new methods and ways to overcome these difficulties. The main developments and models are summarized below.

9.1 Brief Summary of Models

Computer simulation includes two major steps, (i) development of a physical and mathematical model; (ii) efficient solution. In practice, a multitude of factors are involved, and a perfect model is impossible to formulate. Simplifications need to be made, with a focus on key geometric and physical parameters.

In the nanoscale world, a system usually has thousands or even millions or more components. These components can be included in the model either explicitly or implicitly; for the latter, a discrete distribution (e.g. of particles) is ap-

proximated by a continuous one. For example, the distribution of small particles in the magnetic self-assembly model of Chapter 7 is represented by a continuous density. In the protein model of Chapter 6, the distribution of microions in the solvent is treated as continuous and is assumed to be governed by the Poisson-Boltzmann equation. Also, proper boundary conditions can greatly facilitate the simulation. Examples include radiation and PML boundary conditions in the model of a "nanolens" (Chapter 8), as well as periodic boundary conditions common in molecular dynamics.

There are many numerical techniques for solving physical problems. No one is perfect and all-powerful, and each has its own advantages and disadvantages. It is impossible to cover all the techniques in one dissertation or book. In this thesis, the focus is on FLAME and FEM, with their applications to nanoscale systems.

FLAME is a recently developed generalized finite difference (FD) method. Standard FD relies on Taylor expansions around grid nodes to derive a difference scheme. One of the unwelcome implications of this approach is the notorious "staircase" effect at slanted and curved interfaces between different materials. By replacing the Taylor expansions with more accurate approximating functions, FLAME reduces or eliminates the staircase effect. The approximating functions are local-defined only over a small subdomain covering a grid stencil. These functions can be obtained either analytically or numerically, as described in Chapter 3. In this thesis, FLAME is applied primarily to problems in bounded domains, but it can also be used to derive absorbing boundary conditions for unbounded problems [81].

In Chapter 4, FLAME is applied to electrostatic multiparticle problems that are important, for example, in the analysis of colloidal or macromolecular systems. The large number of objects (e.g. colloidal particles) makes traditional methods such as FEM and FD difficult to apply. FLAME is an interesting alternative, as it operates on regular grids and yet takes advanyage of high-quality local approximations. FLAME is demonstrated to have very good accuracy in multiparticle simulations even on fairly coarse grids.

Accurate local approximations satisfying the governing equation are key in the "Trefft" version of FLAME. These approximations can often be obtained analytically or semi-analytically. For example, for multiparticle problems where particles are separated by distances greater than the mesh size, FLAME bases can be constructed using cykindrical (in 2D) or spherical (in 3D) harmonics. In cases where particles are in close proximity to one another, or when particles have complex shapes, the analytical computation is not available. Two methods (semi-analytical bases and adaptive FLAME) are proposed and implemented in the thesis to overcome this difficulty.

Adaptive strategies are already well established in FEM but involve a separate new development for FLAME (Chapter 4). Adaptive schemes take advantage of the fact that FLAME is not restricted to regular meshes. Adaptive FLAME refines the grid locally in regions where the numerical errors are estimated (a posteriori) to be higher. The discrepancy between the patchwise numerical solutions in the areas where two adjacent patches (subdomains) overlap serves as the error indicator.

Both semi-analytical bases and adaptive FLAME are applied to multiparticle problems in Chapter 4. The numerical results for particles in close proximity to one another show that these two strategies yield high accuracy on fairly coarse grids. The results show that these strategies can be a useful part of the overall simulation.

FLAME, including analytical/numerical bases and adaptive mesh strategies, is also applied to wave scattering problems in Chapter 5. The study of wave scattering is important in a variety of areas including radar systems, astronomy, optics, photonics and solid state physics. Our test problems and applications of FLAME involve electromagnetic wave scattering from dielectric or metal particles and are currently limited to 2D problems. (However, applications of FEM to three-dimensional scattering are considered in Chapter 5.) Similar to the static case, FLAME bases are constructed for problems where particles may or may not be well separated (relative to the grid size). FLAME again proves to have much higher accuracy than standard FD schemes.

In Chapter 6, FLAME is applied to electrostatic interactions in macromolecules (e.g. protein molecules). Proteins contain amino acids with charged groups. The electrostatic fields produced by the charges influence the spatial distribution of the microions in the solvent. Electrostatic interactions are critical for the formation and stability of the protein structure and for its function. Under reasonable physical assumptions, this distribution can be described by the Poisson-Boltzmann equation.

A conventional protein model contains two regions: the macromolecular core and the solvent. In the core layer, the protein nuclei are viewed as point

charges. Recently a more accurate model that accurately takes into account both short- and long-range dielectric response of water, was developed by A. Rubinstein and his co-workers [46]. In one practical version of this new model, an intermediate layer with a low dielectric permittivity is introduced. FLAME is applied to this problem in Chapter 6.

The numerical treatment is encumbered by the inhomogeneities of the media and the presence of singularities (point charges). FLAME overcomes these difficulties using potential splitting and accurate analytical bases (see Chapter 6 for details). FLAME again exhibits much higher accuracy than conventional FD.

While FLAME is demonstrated to be a useful tool in selected applications, the finite element method (FEM) still remains the most powerful and versatile numerical technique for problems with complex geometries and inhomogeneous media. The generality of the method makes it possible to develop general purpose computer programs for solving a wide range of problems. In this thesis, FEM is applied to two electromagnetic problems: magnetostatic in the case of self assembly of ferrofluid structures (Chapter 7) and electrodynamic in the case of plasmonic nanolenses (Chapter 8).

Fabrication and assembly of nanoscale systems are quite involved. Self-assembly is the most promising general way for getting highly ordered structures or materials. Magnetic self assembly pioneered by G. Friedman and B. Yellen [1,59,60] is one of such technologies. In this technology, particles are magnetized by an applied magnetic field, and their motion may be controlled by fixed magnetized traps

pre-patterned on the substrate (Chapter 7). FEM is used to simulate the distribution of the ferrofluid density for different applied magnetic fields. The scalar, rather than vector, potential formulation reduces the computational complexity greatly.

Nanolenses, formed by a cascade of plasmonic particles, are of great interest due to enormous electromagnetic field enhancement, with potential applications in ultrahigh-resolution optical microscopy and sensing technology. The computational challenge is that the high enhancement of the field is highly localized and, being produced at a resonance, is very sensitive to all physical and geometric parameters. In Chapter 8, FEM with adaptive mesh refinement is used to simulate the field distribution around the nanolenses. It is found, somewhat counterintuitively, that the quasi-static limit does not produce the highest enhancement, despite the absence of retardation and dephasing in that limit. Furthermore, again somewhat counterintuitively, the highest enhancement does not necessarily occur in direction of polarization of the incident field. These findings emphasize the importance of detailed electrodynamic simulations of nanolenses, and highlight the limitations of existing electrostatic analyses of plasmonic field enhancement.

Overall, the contributions of this thesis can be summarized as follows.

- Systematically implement and apply the new generalized finite difference calculus of FLAME to electrostatic and wave scattering problems. All the results demonstrate high accuracy and flexibility of FLAME.

- Extend the application of FLAME by developing two strategies: semi-analytical bases and adaptive mesh refinement.
- These strategies are applied to in electrostatic multiparticle problem. The simulation results show substantial accuracy improvement even on fairly coarse grids. (Chapter 4)
- FLAME (including adaptive mesh refinement) is applied to wave scattering from cylindrical particles; the feasibility of FLAME is thus demonstrated for wave scattering problems.
- Implemented FLAME for a new protein model with an intermediate dielectric layer. The new model accurately takes into account both short- and long-distance dielectric response. The analytical and semi-analytical approximations in FLAME accurately represent the behavior of the potential due to the singularities and inhomogeneities of the media. As a result, FLAME outperforms the conventional FD methods. (Chapter 6)
- Implemented FEM simulations of ferrofluids. The ferrofluid particle concentration is treated as a continuum density. The model is further simplified by formulating the problem in terms of the of scalar magnetic potential instead of the vector one. (Chapter 7)
- Simulated the field distribution of plasmonic nanolenses using adaptive FEM. Results indicate that the quasi-static limit does not produce the highest enhancement and the highest enhancement does not necessarily occur in direc-

tion of polarization of the incident field, which both are counterintuitive. The simulation of electrodynamic effects lead to appreciable corrections for the research of nanoplasmonics.(Chapter 8)

9.2 Future Outlook

FLAME has proved to have useful applications in multiparticle problems, cylindrical wave scattering problems, and macromolecular simulation. For cases in which particles are in close proximity to each other, analytical/numerical bases and adaptive mesh strategies are proposed and proved to be effective. However, future research needs to be conducted to enhance FLAME further. In this thesis, electromagnetic force is calculated only for "well-separated" particles; this needs to be extended to the 2D "poorly-separated" particles and to 3D as well. Adaptive algorithms need to be extended to 3D models. Also, this thesis does not cover time domain problems which are worthy of future research.

A prototype test model for macromolecular simulation was explored in the thesis. It would be very interesting to apply FLAME to large-scale macromolecular simulations, including for example problems of protein folding, docking, drug design and discovery; this will, however, require a very substantial effort of multiple research groups.

Overall, the thesis has demonstrated that traiditional methods such as FEM and the new finite-difference calculus of FLAME can be successfully applied to challenging problems involving multi-object nanoscale systems.

BIBLIOGRAPHY

[1] B. B. Yellen, Z. G. Forbes, K. A. Barbee, G. Gallo and G. Friedman, "A Method for Printing Heterogeneous Patterns of Cells and Biological Molecules by Magnetically Directed Assembly," *Bioengineering Conference*, June 25-29, Florida, 2003.

[2] B. B. Yellen, "Magnetically Programmable Transport and Assembly of Colloidal Particles," *Ph.D Dissertation, Drexel University*, 2004.

[3] K. K. Jain, "The Role of Nanobiotechnology in Drug Discovery," *Drug Discovery Today*, Vol. 10, Issue: 21, pp. 1435-1442, 2005.

[4] K. Watlington, "Emerging Nanotechnologies for Site Remediation and Wastewater Treatment," *National Technical Information Service*, pp. 55, 2005.

[5] B. Yu and M. Meyyappan, "Nanotechnology: Role in Emerging Nanoelectronics," *Solid State Electronics*, Vol. 50, Issue: 4, pp. 536-544, 2006.

[6] K. Goser, P. Glosekotter and J. Dienstuhl, "Nanoelectronics and Nanosystems: From Transistors to Molecular and Quantum Devices," *Springer*, 2004.

[7] F. T. Ulaby, "Fundamentals of Applied Electromagnetics," *Prentice Hall*, New Jersey, 1999.

[8] M. N. O. Sadiku, "Numerical Techniques in Electromagnetics," 2nd ed., *CRC Press*, 2001.

[9] W. Yu and R. Mittra, "A Conformal Finite Difference Time Domain Technique for Modeling Curved Dielectric Surfaces," *IEEE Microw. Wireless Comp. Lett.*, Vol. 11, No. 1, pp. 2527, 2001.

[10] A. Wiegmann and K. P. Bube, "The Explicit-Jump Immersed Interface Method: Finite Difference Methods for PDEs with Piecewise Smooth Solutions," *SIAM J. Numer. Anal.*, Vol. 37, No. 3, pp. 827862, 2000.

[11] S. Foteinopoulou, J. P. Vigneron and C. Vandenbem, "Optical Near-Field Excitations on Plasmonic Nanoparticle-Based Structures," *Opt. Express* 15, pp. 4253-4267, 2007.

[12] K. Y. Jung and F. L. Teixeira, "Multispecies ADI-FDTD Algorithm for Nanoscale Three-Dimensional Photonic Metallic Structures," *IEEE Photon. Technol. Lett.* 19, pp. 586-588, 2007.

[13] A. Sayyed-Ahmad, K. Tuncay and P. J. Ortoleva, "Efficient Solution Technique for Solving the Poisson-Boltzmann Equation," *Journal of Computational Chemistry*, Vol. 25, No. 8, pp. 1068-1074, 2004.

[14] H. Cheng, L. Greengard and V. Rokhlin, "A Fast Adaptive Multipole Algorithm in Three Dimensions," *J. Comput. Phys.*, Vol. 155, No. 2, pp. 468–498, 1999.

[15] I. Tsukerman, "Electromagnetic Applications of a New Finite-Difference calculus," *IEEE Trans. Magnetic*, Vol. 41, No. 7, pp. 2206–2225, 2005.

[16] I. Tsukerman, "A Class of Difference Schemes with Flexible Local Approximation," *The Journal of Computational Physics*, Vol. 211, No. 2, pp. 659–699, 2006.

[17] V. Thomee, "From Finite Differences to Finite Elements: a Short History of Numerical Analysis of Partial Differential Equations," *J. Comput. Appl. Math.*, Vol. 128, pp. 1-54, 2001.

[18] S. G. Mikhlin, "Approximation on a Rectangular Grid With Application to Finite Element Methods and Other Problems (Translation from the Russian)," *Sijthoff & Noordhoff, Alphen aan den Rijn*, pp. 236, 1979.

[19] J. Jin, "The Finite Element Method in Electromagnetics," *J. Wiley Sons, New York*, pp. 753, 2002.

[20] N. Ida, "Engineering Electromagnetics," 2nd ed., *New York: Springer*, 2004.

[21] I. Tsukerman, "Computational Methods for Nanoscale Applications: Particles, Plasmons and Waves," *Springer*, 2007.

[22] I. Tsukerman, "Flexible Local Approximation Method for Electro- and Magnetostatics," *IEEE Trans. Magn.*, Vol. 40, No. 2, pp. 941944, 2004.

[23] J. Dai, I. Tsukerman, A. Rubinstein and S. Sherman, "New Computational Models for Electrostatics of Macromolecules in Solvents," *IEEE Trans. Magn.*, Vol. 43, No. 4, pp. 1217-1220, 2007.

[24] H. Pinheiro, J. P. Webb and I. Tsukerman, "Flexible Local Approximation Models for Wave Scattering in Photonic Crystal Devices," *IEEE Trans. Magn.*, Vol. 43, No. 4, pp. 1321-1324, 2007.

[25] J. D. Jackson, "Classical Electrodynamics," *New York: Wiley*, 1962.

[26] L. F. A. Asghar and S. Chandran, "Multiparticulate Formulation Approach to Colon Specific Drug Delivery: Current Perspectives," *J Pharm Pharmaceut Sci.*, 9(3), pp. 327-338, 2006.

[27] M. Paulsson and S. K. Singh , "Colloidal and Thermal Characteristics of Concentrated Dispersions of Polymethacrylate-Based Latices for Aqueous Enteric Coating," *Journal of Pharmaceutical Sciences*, pp. 406-411, 2000.

[28] R. L. Graham, D. E. Knuth and O. Patashnik, "Concrete Mathmatics: A Foundation for Computer Science, 2nd ed. Reading," *MA: Addison-Wesley*, pp. 162, 1994.

[29] H. Choi, I. Park and S. Lee, "Electromagnetic Body Force Calculation Based on Virtual Air Gap," *Journal of Applied Physics*, pp.99-102, 2006.

[30] B. Z. Lu, X. L. Cheng, J. F. Huang, and J. A. McCammon, "Order N Algorithm for Computation of Electrostatic Interactions in Biomolecular Systems," *Proceedings of the National Academy of Sciences of the United States of America* pp. 19314-19319, 2006.

[31] I. Babuska, J. Chandra and J.E. Flaherty, "Adaptive Computational Methods for Partial Diferential Equations," *Philadelphia SIAM.*, 1983.

[32] J. Dai, I. Tsukerman, "Flexible Approximation Schemes with Adaptive Grid Refinement," *IEEE Trans. Magn.*, Vol. 44, No. 6, pp. 1206 - 1209, 2008.

[33] M. Koshiba, Y. Tsuji and M. Hikari, "Time-Domain Beam Propagation Method and Its Application to Photonic Crystal Circuits," *J. Lightwave Technol.*, Vol.18, No.1, pp. 102-110, 2000.

[34] J.Yamauchi, M. Mita, S. Aolii and H. Nakano, "Analysis of Antireflection Coatings Using the FDTD Method with the PML Absorbing Boundary Condition," *IEEE Photon. Techno/. Lett.*, Vol. 8, pp. 239-241, 1996.

[35] R. Kappeler, D. Erni, C. Xudong and L. Novotny, "Field Computations of Optical Antennas," *J. Comput. Theor. Nanosci.*, Vol. 4, No. 3, pp. 686-691, 2007.

[36] W. C. Chew, "Waves and Fields in Inhomogeneous Media," *Van Nostrand Reinhold*, pp. 591-596, 1990.

[37] M. F. Perutz, "Electrostatic Effects in Proteins," *Science*, 201, pp. 1187-1191, 1978.

[38] T. Simonson, "Electrostatics and Dynamics of Proteins," *Rep. Prog. Phys.*, Vol. 66, Vo. 5, pp. 737-787, 2003.

[39] A. A. Kornyshev and S. Leikin, "Electrostatic Interaction Between Helical Macromolecules in Dense Aggregates: An Impetus for DNA Poly- and Meso-Morphism," *Proc. Natl. Acad. Sci.*, 95, pp. 1357913584, 1998

[40] K. Sharp, "Electrostatic Interactions in Proteins," *International Tables for Crystallography, International Union of Crystallography*, Chester, UK, 1999.

[41] S. Kumar, H. J. Wolfson and R. Nussinov, "Protein Flexibility and Electrostatic Interactions," *IBM Journal of Research and Development*, Vol. 45, pp. 499-512, 2001.

[42] W. Rocchia, S. Sridharan, A. Nicholls, E. Alexov, A. Chiabrera and B. Honig, "Rapid Grid-Based Construction of the Molecular-Surface and the Use of Induced Surface Charge to Calculate Reaction Field Energies: Applications to the Molecular Systems and Geometric Objects," *J. Comput. Chem.*, Vol. 23, pp. 128-137, 2002.

[43] M. Gilson, A. Rashin, R. Fine and B. Honig, "On the Calculation of Electrostatic Interactions in Proteins," *J. Mol. Biol.*, Vol. 183, pp. 503-516, 1985.

[44] M. Gilson, K. Sharp and B. Honig, "Calculating the Electrostatic Potential of Molecules in Solution: Method and Error Assessment," *J. Comp. Chem.*, Vol. 9, pp. 327-335, 1988.

[45] A. Papazyan and A. Warshel, "Continuum and Dipole-Lattice Models of Solvation", *J. Phys. Chem. B*, 101, pp. 11254-11264, 1997.

[46] A. Rubinstein and S. Sherman, "Influence of the Solvent Structure on the Electrostatic Interactions in Proteins," *Biophysical Journal*, Vol. 87, pp. 1544-1557, 2004.

[47] S. K. Pal and A. H. Zewail, "Dynamics of Water in Biological Recognition," *Chem. Rev.*, 104, pp. 2099-2123, 2004.

[48] J. J. Havranek and P .B. Harbury, "Tanford-Kirkwood Electrostatics for Protein Modeling," *Proc. Natl. Acad. Sci.*, 96, pp. 11145-11150, 1999.

[49] P. M. Chaikin and T. C. Lubensky, "Principles of Condensed Matter Physics," *Cambridge University Press*, 1995.

[50] F. Fogolari, P. Zuccato, G. Esposito and P .Viglino, "Biomolecular Electrostatics with the Linearized Poisson-Boltzmann Equation," *J. Biophys* Vol. 76, pp. 1-16, 1999.

[51] C. O. Hwang, M. Mascagni and N. A. Simonov, "Monte Carlo Methods for the Linearized Poisson-Boltzmann Equation," *Advances in Numerical Analysis*, Nova Science, Hauppauge, NY, 2004.

[52] Z. Zhou, P. Payne, M. Vasquez, N. Kuhn and M. Levitt, "Finite-Difference Solution of the Poisson-Boltzmann Equation: Complete Elimination of Self-Energy," *J. Comput. Chem.*, Vol. 17, pp. 1344-1351, 1996.

[53] I. Klapper, R. Hagstrom, R. Fine, K. Sharp and B. Honig, "Focusing of Electric Fields in the Active Site of Cu-Zn Superoxide Dismutase," *Proteins*, Vol. 1, pp. 47-59, 1986.

[54] M. Boncheva, S. A. Andreev, L. Mahadevan, et al. "Magnetic Self-Assembly of Three-Dimensional Surfaces from Planar Sheets," *PNAS* 102, 3924-3929, 2005).

[55] A. Ciferri, "Assembling Nano and Macrostructures and the Supramolecular Liquid Crystal," *Progress in Polymer Science*, Vol. 20, Issue: 6, pp. 1081-1120, 1995.

[56] A. Kumar, H. A. Biebuyck and G. M. Whitesides, "Patterning Self-Assembled Monolayers: Applications in Materials Science," *Langmuir*, Vol. 10, pp. 1498-1511, 1994.

[57] H. O. Jacobs, A. R. Tao, A. Schwartz, D. H. Gracias and G. M. Whitesides, "Fabrication of a Cylindrical Display by Patterned Assembly," *Science*, Vol. 5566, pp. 323-325, 2002.

[58] O. D. Velev and E. W. Kaler, "In Situ Assembly of Colloidal Particles into Miniaturized Biosensors," *Langmuir*, Vol. 15, pp. 3693-3698, 1999.

[59] B. Yellen, G. Friedman, A. Feinerman, "Printing Superparamagnetic Colloidal Particle Arrays on Patterned Ferromagnetic Film," *Journal of Applied Physics*, Vol. 93, pp. 7331-7333, 2003.

[60] B. Yellen, G. Friedman, "Programmable Assembly of Colloidal Particles Using Magnetic Micro-well Templates," *Langmuir* Vol. 20, pp. 2553-2559, 2004.

[61] J. Andrus, W. L. Bond, "Photoengraving in Transistor Fabrication," *Transistor Technology*, Vol III, Princeton, N. J., pp. 151-162, 1958.

[62] A. Hierlemann, O. Brand, C. Hagleitner, H. Baltes, "Microfabrication Techniques for Chemical/Biosensors," *Proceedings of the IEEE*, Vol. 91, pp. 839-863, 2003.

[63] Rouillard, A. and Lockwood, M. "Oscillations in the Open Solar Magnetic Flux with a Period of 1.68 Years: Imprint on Galactic Cosmic Rays and Implications for Heliospheric Shielding," *Annales Geophysicae*, Vol. 22, pp. 4381-4395, 2004.

[64] Skjeltorp, A. T. "Colloidal Crystals in Magnetic Fluid," *Journal of Applied Physics*, Vol. 55, pp. 2587-2598, 1984.

[65] Einstein, A. "On the Motion of Small Particles Suspended in Liquids at Rest Required by the Molecular-Kinetic Theory of Heat," *Annalen Der Physik*, Vol. 17, pp. 549-560, 1905.

[66] A. H. Morrish, "The Physical Principles of Magnetism," *IEEE Press*, New York, 2001.

[67] U. Huebner, W. Morgenroth, R. Boucher, M. Meyer, W. Mirande, E. Buhr, G. Ehret, G. Dai, T. Dziomba, R. Hild and T. Fries, "A nanoscale Linewidth/Pitch Standard for High-Resolution Optical Microscopy and Other Microscopic Techniques," *Meas. Sci. Technol.*, 18, pp. 422-429, 2007.

[68] H. Rigneault, J. M. Lourtioz, C. Delalande and A. Levenson, "Nanophotonics," *ISTE Ltd*, 324p, 2005.

[69] S. A. Maier, M. L. Brongersma, P. G. Kik, S. Meltzer, A. A. G. Requicha and H. A. Atwater, "Plasmonics - A Route to Nanoscale Optical Devices," *Adv. Mater.*, Vol. 13, pp. 1501-1505, 2001.

[70] L. Novotny, "The History of Near-Field Optics: Progress in Optics," *E. Wolf (ed.)*, 2007.

[71] S. Lal, S. Link and N. J. Halas, "Nano-Optics from Sensing to Waveguiding," *Nature Photonics*, Vol. 1, pp. 641-648, 2007.

[72] U. Kreibig and M. Vollmer, "Optical Properties of Metal Clusters," *Springer,* 1995.

[73] K. R. Li, M. I. Stockman and D. J. Bergman, "Self-Similar Chain of Metal Nanospheres as an Efficient Nanolens," *Phys. Rev. Lett.*, Vol. 91, pp. 227402:1-4, 2003.

[74] K. Kneipp, H. Kneipp, M. S. Dresselhaus and S. Lefrant, "Surface-Enhanced Raman Scattering on Single Wall Carbon Nanotubes," *Philos. Trans. R. Soc. Lond. Ser. A-Math. Phys. Eng. Sci.*, Vol. 362, pp. 2361-2373, 2004.

[75] D. M. Sullivan, "A Simplified PML for Use with the FDTD Method," *IEEE Microwave Guided Wave Lett.*, Vol. 6, pp. 97-99, 1996.

[76] H. Zheng, C. Zhang and D. Ge"Extending Anisotropic Perfectly Matched Layer Absorbing Boundary Condition to Biaxial Media," *INT J INFRARED MILLI*, Vol. 22, pp. 101-111, 2001.

[77] Ansoft Corporation, "High Frequency Structure Simulator (HFSS)," http://www.ansoft.com/products/hf/hfss/, 2006.

[78] P. B. Johnson and R. W.Christy, "Optical constants of the noble metals," *Phys. Rev. B*, Vol. 6, pp. 4370-4379, 1972.

[79] J. Dai, F. Cajko, I. Tsukerman, and M. I. Stockman, "Electrodynamic effects in plasmonic nanolenses," *Phys. Rev. B*, 77, 115419, 2008.

[80] R. F. Harrington, "Time-Harmonic Electromagnetics Fields," *McGraw-Hill, New York*, 1961.

[81] D. Halverson, G. Friedman and I. Tsukerman, "Local Approximation Matching for Open Boundary Problems," *IEEE Trans. Magn.*, pp. 2152-2154, 2004.